Experimental investigation of a zeotropic working fluid and working fluid filling factor on system performance in a small-scale ORC.

(Master Thesis)

A thesis submitted in partial fulfilment of the requirements for the Degree of Master of Engineering in Mechanical Engineering

University of Canterbury

2017

Richard Wijninckx

Acknowledgements

I am very grateful to Professor Dr. Susan Krumdieck, of the University of Canterbury, who made this work possible. I thank her for the continuous support, deep insights, and an overall fantastic learning experience.

A special thanks goes to Dr. Sid Becker without whose patience, encouragement, and direction this work would not have been possible.

I would like to thank the members of the technical staff, especially G. Kirk, E. Cox, and G. Cotton for their valuable insights and help on several occasions. I also would like to thank the University of Canterbury Mechanical Department for their financial assistance and making this study possible.

Finally, I want to thank my fellow students and family who contributed indirectly to the thinking and experimentation in this thesis journey. Especially to my partner M. Curry, without whose support this study may never have been completed.

Abstract

Organic Rankine Cycle (ORC) systems are capable of utilising low-enthalpy heat sources to generate power. For the performance engineering of ORC systems, it is important to understand process parameters and component behaviour. To maximise performance, modelling of the plant thermodynamics must be coupled with data analysis to develop diagnostic procedures, find optimal operating points, and diagnose problems to schedule the most cost effective maintenance. An existing ORC system at the University of Canterbury has been upgraded from a previous iteration to assist in furthering our knowledge of ORC system design and construction.

This paper presents experimental results from running a 1 kW ORC system using HFC-M1 refrigerant, a zeotropic mixture of R245fa and R365mfc, as the working fluid under a wide range of operating conditions. Hot exhaust combustion products from a 30kW Capstone^{TM} Gas Turbine are used as the heat source, and heat is transferred via a thermal oil loop to the working fluid through a plate heat exchanger. A scroll expander magnetically coupled to an AC generator is used for work extraction and energy conversion.

Trials focused on testing the full range of performance, and investigated the effect of a zeotropic working fluid, and the influence of varying the working fluid liquid level on system performance.

Trials were prematurely ended by bearing failure in the ORC scroll expander. However, analysis of the results from additional tests suggest the working fluid charge in the system influences operation, corroborating findings in literature. While inconclusive, these initial results support the need for further testing the effect of the DVR in a fully functioning system.

A comparative study was performed between the system actual performance and the theoretical performance to evaluate the degree of impact of the operational issues on the system performance. The unit was disassembled to evaluate the component compatibility and assess functionality over the operation. It transpired the system mass was not conserved during the operation due to leakage, contributing to the overall deterioration in system performance over time. It is concluded the zeotropic mixture was chemically incompatible with system components leading to system failure.

Critiques of components and working fluid, derived from experiences in operating the system, coupled with general trends produced by the results, provide recommendations for the design and testing of future small-scale ORC systems.

Table of Contents

Table of Figures

Table of Tables

Nomenclature

Abbreviations

See Appendix A, Glossary

Symbols

η	efficiency (%)
ρ	density (kg/L)
σ	motor slip factor
ϕ	Filling factor (ratio)
c_p	heat capacity, const. pressure (J/kg)
DVR	Dimensionless Volume Ratio
f	frequency (Hz)
h	specific enthalpy (kJ/kg) or heat transfer coefficient (W/m)
$\dot{m}$	mass flow (kg/s)
N_{rot}	Rotational speed (RPM)
P	pressure (Pa)
$\dot{Q}$	heat absorbed or released (W)
T	Temperature (°C or K)
v	kinematic viscosity (cSt)
V	Volume (m^3)
$\dot{W}$	Work (W)

Subscripts

1..8	process stages
abs	absorption
Capstone	Capstone microturbine
carnot	Carnot
cond	condenser
cycle	ORC cycle
e	electrical
exp	expander
evap	evaporator
exhaust	Capstone exhaust
gen	generator
gross	gross
global	entire ORC, including heat transfer loop
II	second law
ideal	ideal / theoretical
mot	motor
net	net
pump	pump
r	rate
real	measured / experimental
rot	rotation
s	isentropic
sub	subcooling
sup	superheating
sys	system / circuit
tf	transfer fluid
water	heat sink water
wf	working fluid

Chapter 1 Introduction

1.1 Motivation

The Organic Rankine Cycle (ORC) provides a method to generate electricity from heat sources that cannot be captured by a conventional steam-powered Rankine cycle. Heat recovery from sources such as industrial exhaust streams presents an opportunity for the reduction of fossil fuel consumption.

While commercial proprietary ORC plants are already successfully operating in megawatt power range, research over the past decade has been conducted to understand the technical and economic feasibility of extending ORC operation to the kilowatt range.

For the design, component selection and operation of ORC systems, it is important to understand process parameters and component behaviour. Since 2012, the University of Canterbury has been developing and testing a 1 kW small-scale ORC. This system allows investigation of the impact of design parameters on performance, for future scale-up and product development considerations.

Until now the performance of this ORC system has not been investigated systematically. The current study used the 1 kW test rig, with majority of the system componentry and working fluid inherited in various states of functionality. During this iteration of the project, the next key component for understanding is of the influence of system working fluid charge on performance, and the impact of controllable inputs.

A clear understanding of the impact of the working fluid liquid level and system behaviour is required to progress small ORC development. When designing a small-scale ORC, there appears to be no published references to inform the working fluid volume charge, and its possible effect on system performance. The current study aims to provide an investigation of the possible effect of fluid level on performance. The analysis in this study provides insight into system input parameter relationships through testing, and where opportunities lie for further improvement.

1.2 Objective

The objective of this study is to investigate the potential of the working fluid to have an effect on ORC performance. The rationale is informed by the following considerations:

1. That the working fluid volume charged into the system influences heat exchanger performance in either the evaporator or condenser.
2. This heat exchanger performance affects the net rate of heat transfer to the working fluid.
3. That this in turn influences cycle performance (efficiency and net power output), and the flexibility of the system to accommodate a wider range of operating conditions.

1.3 Approach

In its previous iterations, the system had never been fully tested. Therefore, the first step in the experimental study was to systematically investigate the system over its operational range. The aim of these trials was threefold:

1. Establish the upper and lower boundaries of system steady state operation.
2. Establish the degree of impact the controllable inputs had on performance.
3. Collect a detailed data set for the highest working fluid level to be tested, for analysis of system performance metrics.

The results from this experiment would inform a selection of operating inputs to progressively test the effect of decreasing the working fluid level in the system. The inputs would balance a good resolution of the performance metrics under consideration, within a reasonable total testing time.

In order to validate the design, a basic theoretical thermodynamic simulation using informed operating points is conducted. This is adapted to investigate theoretical performance using experimental operating conditions as inputs.

The study adopts commonly used performance metrics to enable comparison with other published works. These include, amongst others, expander isentropic efficiency, gross power, net power, and cycle thermal efficiency.

Analysis of the experiential results, experiences during testing, and findings in published literature will allow assessment of the current design. From this, informed suggestions for improvement and the next design iteration will be derived.

1.4 Thesis outline

Chapter 1 presents a brief introduction of the working principles, main components, and applications of ORCs, providing a background to the research of the current study. In Chapter 2, a literature review covers pertinent system aspects and similar studies of experimental sub-10 kW ORC systems. This is used to inform the testing methodology, and as a comparison for system performance. Chapter 3 details a theoretical thermodynamic simulation of the ORC, used as a benchmark for the system performance, and subsequent analysis of experimental results. Chapter 4 outlines the experimental equipment, methodology, and rationale for the testing. Chapter 5 presents the results and analysis of the experimental trials, and covers the disassembly of the setup to investigate the cause of various system abnormalities. Finally, Chapter 6 identifies system shortcomings informed by experimental experiences and comparable published systems in literature, and suggests improvements for future testing.

Chapter 2 Literature Review

This literature review chapter presents studies concerning small ORC development, technological considerations of similar scroll ORCs, the potential influence of the system working fluid volume on performance, and common best practises for assessment.

Section 2.1 provides a generic overview of ORC systems. Sections 2.2 and 2.3 outline the previous work performed on the ORC used in the current study, and reported literature of ORC systems as bottoming cycles for internal combustion engines. Sections 2.4 to 2.6 detail considerations of the working fluid, operating principles of the scroll expander, and modelling of experimental ORC systems. Section 2.7 presents the findings of studies utilizing the same scroll expander as the current study, and a summary of similar experimental small ORC systems for performance comparisons.

Section 0 presents the influence of the working fluid charge on ORC performance. The current study identifies this as an area of importance with little reported literature, and which merits further investigation. Finally, section 2.9 outlines the studies whose testing methodologies influence that used in the current study.

2.1 Background of ORC Systems

2.1.1 Overview of ORC system components

The following sub sections provide an overview of essential components that comprise the ORC system.

2.1.1.1 Cycle Configuration

The organic Rankine cycle (ORC) is a closed thermodynamic cycle that extracts a work output using a heat source. The basic organic Rankine cycle is achieved by circulating an organic working fluid through the following four processes, illustrated in Figure 2.1:

1. Compression – The addition of work to the working fluid, commonly achieved commonly by a pump to raise the pressure for the evaporator.
2. Evaporation – Heat energy is added to the working fluid to raise the state from liquid to vapour via one or more heat exchangers.
3. Expansion – Work energy is extracted from the pressurised fluid to create power through the use of an expansion machine such as a turbine or scroll expander.
4. Condensation – Heat energy is removed from the working fluid, returning it to a liquid state suitable for compression, using a heat exchanger and a medium (such as air or water) to reject the heat.

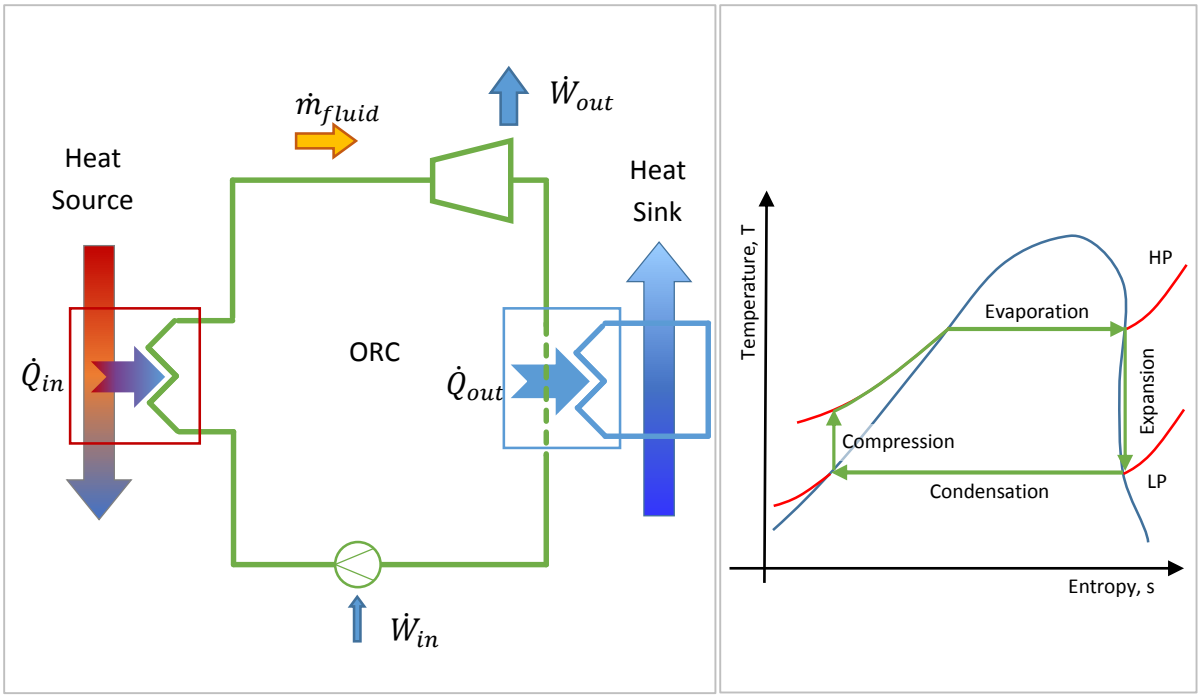

Figure 2.1 – Schematic and T-s diagram representation of a simple Organic Rankine Cycle (ORC). High and low pressure isobars denoted as HP and LP respectively.

2.1.1.2 Expanders

One of the key defining components of the ORC is the expander. Table 1 briefly outlines the common types of expander and their operating capacities.

Table 1 – Comparison of the different ORC expander types. Adapted from Table 8 in (Bao and Zhao, 2013).

Type	Capacity range (kW)	Rotational speed (RPM)	Relative cost	Advantages	Disadvantages
Radial-inflow turbine (Velocity)	50 - 500	8,000-80,000	High	Light weight, mature manufacturability and high efficiency at design conditions	High cost, low efficiency in off-design conditions, cannot tolerate two-phase conditions
Scroll expander (Volumetric)	1 – 10	< 6000	Low	High efficiency, simple manufacture, light weight, low rotational speed, tolerates two-phase conditions	Low capacity, often requires lubrication

Type	Capacity range (kW)	Rotational speed (RPM)	Relative cost	Advantages	Disadvantages
Screw expander (Volumetric)	15 – 200	< 6000	Medium	Low rotational speed, high efficiency over broad range, tolerates two-phase conditions	Requires lubrication, complex to manufacture and seal
Reciprocating piston expander (Volumetric)	20 – 100	-	Medium	High expansion ratio, mature manufacturability, tolerates two-phase conditions	Many moving parts, valve and torque impulse.
Rotary vane expander (Volumetric)	1 – 10	< 6000	Low	Simple construction, low cost, tolerates two-phase conditions	Requires lubrication, low capacity, low efficiency

For sub-10 kW systems, such as that used by the current study, expander choice is almost exclusively limited to volumetric type, as shown in Table 1. Understanding the operating principles of the expander is important for characterizing its behaviour, therefore scroll expanders are further detailed in section 2.5.

2.1.1.3 Heat exchangers

The role of the heat exchanger is to transfer heat from the hot and cold fluid streams to the ORC loop. The two main types of heat exchangers used in ORC units are shell and tube, and plate type. Plate heat exchangers are usually more compact than shell and tube due to a larger contact surface area, but incur a higher pressure drop and are more difficult to maintain. This makes them most suited to smaller applications, where the economic advantage of a cheaper heat exchanger outweighs the cost of a slightly lower power output (Budisulistyo et al., 2014).

2.1.1.4 Pumps

The function of the pump in the ORC is to circulate the working fluid, and raise the pressure. For small-scale systems, pump selection is limited due to the low mass flow rates across a high pressure differential, thereby excluding centrifugal pumps (Muhammad et al., 2015). The remaining options are positive displacement pumps, examples of which include diaphragm, reciprocating piston, and gear type pumps. All these types of pumps inherently produce a varying degree of pressure spikes as part of their operation, which is undesirable for measuring the working fluid flow rate.

2.1.1.5 Working fluid

The organic working fluid is the medium that is used to generate work output from the heat source. The thermo-physical properties of the working fluid dictate its performance. Since the optimal working conditions are closely linked to the selected working fluid, selection is critical to design and the system's ability to utilize the available heat source (Quoilin et al., 2012). The properties and considerations for working fluid are elaborated on in section 2.4.

2.1.2 Overview of ORC commercial units and applications

This section outlines commercially available ORCs and their applications, to provide context for the opportunity of small-scale ORC systems.

2.1.2.1 Commercially available

Table 2 briefly outlines the current commercially available ORCs. This illustrates the opportunity for developing small-scale ORCs in the sub-50 kW capacity range.

Table 2 - (Peris et al., 2015c)

Manufacturer	Power (kW)	T (°C)	Working fluid	Expander type
Adoratec/Maxxtec (Germany)	315–1600	300	Octamethyltrisiloxane (OMTS)	Turbine
Barber Nichols (USA)	700–2700	>115	–	Turbine
Electratherm, (USA)	30–50	>88	R245fa	Volumetric (Screw)
Eneftech (Switzerland)	may-30	120–200	R245fa	Volumetric (Scroll)
Freepower (England)	120	>110	Hexane	Turbine
GE Clean Cycle/Calnetix (USA)	125	>120	R245fa	Turbine (radial)
GMK (Germany)	50–5000	120–350	GL-160, WL-220	Turbine (multistage, axial)
Infinity turbine (USA)	10–250	90-120	R134a, R245fa	Turbine
Lti REEnergy (Germany)	30	>160	-	-
TransPacific (USA)	100–5000	<480	-	Turbine
Tri-o-gen (Netherlands)	60–160	>350	Toluene	Turbine
Turboden (Italy)	200–2,000	100–300	OMTS, Solkatherm	Turbine (two-stage axial)
Pratt & Whitney Systems (USA)	280	90–150	R245fa	Turbine (radial)
Ormat (USA)	200–70,000	150–300	n-pentane, other	Turbine (two-stage axial)
Enertime (France)	300–5,000	200	HFC	Turbine
Phoenix (Australia)	10–5000	80–900	R245fa, Novec649, Cyclohexane	Not specified (Scroll expander, turbine)
Rank (Spain)	2–100	80, >140	R245fa, other	Volumetric
Zuccato Energy (Italy)	50,150	94, >160	–	Turbine (radial)
Bosch KWK (Germany)	65–325	120–150	R245fa	Turbine
Cryostar (France)	500–15,000	100–400	R245fa, R134a	Turbine (radial)
Opcon (Sweden)	350–800	<120	Ammonia	Volumetric (Lysholm)

2.1.2.2 Applications

Typical applications of ORCs using low-medium temperature heat sources include waste heat from industrial processes, internal combustion engines, gas turbine power systems, geothermal hot water sources, solar heat, and biomass energy (Zhai et al., 2016). The characteristics for these heat sources are summarised in Table 3.

Table 3 – ORC applications and heat source characteristics. Adapted from Table 2 in (Zhai et al., 2016).

Heat source	Source temperature	Capacity	System Cost
Industry	80–500 °C, Mostly 200–300 °C	125 kW–3 MW 10 MW for big industry	System total cost 1500–4500 €/kW,
Waste heat Internal CE	80 – 100 °C cooling system; 400 – 900 °C exhaust gas	95 kW–6.5 MW	No data
Power waste heat GT	250 – 550 °C	50 kW-6.5 MW	Micro GT + ORC, 2500–3000 €/kW
Geothermal	80 – 180 °C	0.6–27 MW	1000–4000 €/kWe
Solar collector	< 300 °C	< 30 MW	MW system 5000–6000 €/kWe
Solar pond	80 – 90 °C	6 kW–5 MW	MW system 5000–6000 €/kWe
Biomass	Around 300 °C	100–1500 kW	1600 €/kWe for medium scale 10,000 €/kWe for small-scale

2.2 University of Canterbury ORC development

The University of Canterbury has been investigating small-scale Organic Rankine Cycles since 2012, designing a 1 kW test system for demonstration of the design process and testing of different potential expanders. Furthermore, the system allows investigation of the impact of design parameters on performance, for future scale-up considerations. The following studies describe the work performed to date on the ORC system used in the current study.

In (Meyer et al., 2013) the authors present the design process, component selection, and fabrication of a 1 kW ORC test bed known as ORC-B. At the conclusion of the study, the system is ready to be charged with working fluid for testing. The current study utilizes the majority of the componentry assembled in Meyer et al.'s study.

Concurrently to Meyer et al., the author in (Engel, 2013) details the design and fabrication of the heat transfer loop from the Capstone micro gas turbine exhaust to the ORC-B. This consists of design and fabrication of a finned-tube heat exchanger, thermal oil and pump selection, and expanding diaphragm specification. Their thesis presents relevant system parameters and equations used by the current study.

In (Southon, 2014) and (Jung et al., 2015), the authors perform initial experimental tests on the ORC system. Both authors conclude with the future work requirement of adding a working fluid flow meter and improved sensory equipment for further testing to be viable.

In (Southon, 2014), the author presents the initial commissioning and testing of ORC-B. Notably the system lacks a working fluid flow meter, instead calculating this quantity indirectly from measured frequency and known displacement of the volumetric pump. A total of six steady state points were achieved, with maximum cycle efficiency of 2 %.

The study by (Jung et al., 2015) presents further testing, with one experimental data point. The maximum cycle efficiency was 3.9 %, and a maximum expander isentropic efficiency of 28.4 % was achieved. However, a disagreement in the energy balance in the evaporator and condenser implied inaccuracy in the indirect measurement method of the fluid flow rate. As such, results are subject to a high degree of uncertainty. This highlights the effect of losses, and the limitations of comparing data from a real system to thermal cycle models that assume adiabatic components and internally reversible processes.

2.3 Bottoming cycles for Internal Combustion Engines

The ORC in the current study utilizes the waste heat from the exhaust stream of a diesel powered Capstone C30 micro turbine. It is therefore pertinent to consider published studies using similar heat sources for common best practise methods for analysis.

In (Shu et al., 2016) the authors present an experimental ORC system designed for waste heat recovery from exhaust gases of a 240 kW diesel engine. The system features no expander, and instead uses an expansion valve to estimate potential power output, using R123 as a working fluid. A thermal oil loop is used to transfer heat from the exhaust stream. A heat balance test of the diesel engine is performed without the ORC to investigate the varying properties of the exhaust gas. This builds a performance map of recoverable heat as a function of engine load and shaft speed.

The authors denote the recoverable heat from the exhaust gas as Q_{ideal}, defined as the heat released when cooled to an acid dew point of 120 ^{o}C. This is done to protect the heat exchanger from corrosion, as CO_2 and sulphur dissolve in condensed water vapours, producing acid attack of metal below this temperature. The calculation rationale and method is adopted in the current study.

Shu makes the observation that exhaust gas temperatures exceed decomposition temperatures of most organic working fluids, necessitating a transfer loop to reduce temperatures. The thermal oil additionally acts as a thermal damper, smoothing out fluctuations in heat input caused by changing engine operation.

The authors propose the metric of heat absorption efficiency, defined in equation (1) as the ratio of the measured heat transfer from the exhaust stream ($\dot{Q}_{real}$) to the recoverable waste heat ($\dot{Q}_{ideal}$).

$$\eta_{abs} = \frac{\dot{Q}_{real}}{\dot{Q}_{ideal}} \tag{1}$$

This is adopted by the current study, however, it is modified to better reflect the ability of the entire ORC system to capture useful heat by considering the heat transferred to the working fluid ($\dot{Q}_{evap}$) as opposed to ($\dot{Q}_{real}$) (see equation (21), page 69). The results of (Shu et al., 2016) provide a point of

reference for the magnitude of heat recovery, ranging from 100% (cooled to acid dew point) at low engine loading to 47% at full load, where proportionally more heat is lost from the system.

In (Yu et al., 2013), the authors present the results of a simulation of an ORC utilizing diesel exhaust as a heat source. To evaluate exhaust gas properties, perfect combustion of diesel fuel is assumed. The resulting composition on mass basis is calculated to be: CO_2 = 15.1%, H_2O = 5.5%, N_2 = 71.6%, O_2 = 7.8%. This approach is adopted by the current study, creating a gas profile in REFPROP 9.0 fluid property software.

In (Yang et al., 2013) the authors experimentally test the exhaust energy of a diesel engine as a heat source for an ORC. Similarly to (Shu et al., 2016), the authors define the available exhaust energy as the heat rejected to a set temperature, but instead specify this as 30 ^{o}C. However, this neglects the possibility of corrosion caused by acid condensation in the heat exchanger. Additional to the normal performance metrics of net power output and thermal efficiency, the authors propose WHRE (waste heat recovery efficiency) as a performance index. WHRE is defined as the ratio of net power output to the available exhaust gas energy of the engine. This allows objective evaluation of the running performance of an ORC.

In (Lemmens et al., 2006) the authors report on a finned tube heat exchanger of similar design and dimensions to that used by the current study, also extracting waste heat from a C30 Capstone micro turbine. The system captured 60 kWth at full turbine load, at an overall efficiency of 84%. As such, this provides a reference point for comparison of the current study.

(Galindo et al., 2015) presents the experimental analysis of an ORC operating on the waste heat of a 2 litre turbocharged gasoline engine. The system incorporates a prototype swash-plate expander, and uses ethanol as the working fluid, both of which appear unique in small-scale ORC units. The study aims to determine the influence of the controllable input parameters. The authors achieve this by changing one parameter at a time while holding the remainder constant. The resulting 28 steady state points provide a high-quality set of data, with clearly visible trends. The study presents similar trends to (Declaye et al., 2013). In particular, isentropic efficiency exhibits a maximum at an expansion ratio which is specific to the heat input, while power monotonically increases with the expansion ratio.

The exhaust heat transfer ranged from 5 to 30 kW, of similar magnitude to the current study. The maximum cycle efficiency was 6%, while the swash-plate expander reached a maximum isentropic efficiency of 38%. This is substantially lower than scroll expanders reported in the reviewed literature, which range from 50 - 60%, with a maximum around 75%.

2.4 Working fluid

Working fluids in ORCs is an area of abundant published research. As the current study uses a zeotropic mixture working fluid determined by lack of access to any alternatives, the scope of the literature review is limited to research regarding the general influence of the working fluid on the ORC, general working fluid behaviour and characteristics, and zeotropic fluid mixtures.

2.4.1 Working fluid characteristics

The selection of working fluid influences nearly every aspect of the ORC. It determines the efficiency of the system, the size and cost of system components such as heat exchangers and expansion machine, system stability, safety, and environmental concerns (Bao and Zhao, 2013). As such, working fluid has a large influence on the ORC performance and economic feasibility. This is especially prevalent in low temperature ORC (as used in the current study), where heat transfer inefficiencies have a proportionally larger effect on cycle efficiency (Quoilin, 2007). These inefficiencies are dependent on the thermodynamic characteristics of the working fluid and system operating conditions.

2.4.1.1 Isentropic saturation vapour curve

Fluids can be classified into three categories based on the shape of their saturation temperature-entropy (T-s) diagram vapour curves: dry fluids, wet fluid and isentropic fluids (Hung et al., 2010). This shape dictates expansion characteristics of the fluid, which underpins allowable operating conditions and heat source utilization (Quoilin et al., 2012).

Figure 2.2 presents examples of the three fluid shapes: a dry fluid with a positive slope (R245fa), an isentropic fluid with a vertical slope (R11), and wet fluid with a negative slope (R22). A theoretical cycle with superheating and subcooling of 5K and an isentropic expansion of 65% is shown in blue, representing a realistic cycle. Isentropic expansion from saturated vapour is shown by a black dashed line, presenting the ideal cycle.

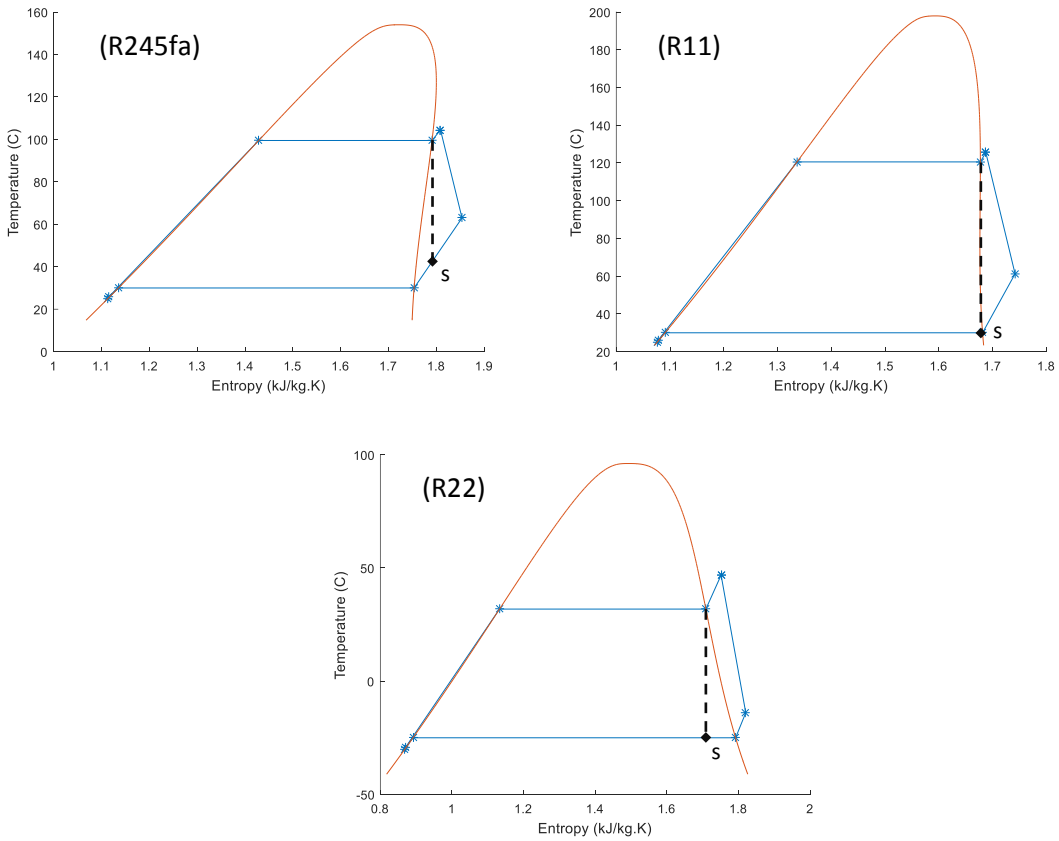

Figure 2.2 – T-s diagrams of a dry fluid with a positive slope (R245fa), an isentropic fluid with a vertical slope (R11), and wet fluid with a negative slope (R22). Realistic theoretical cycle shown in

blue, while dashed black lines depict ideal cycle isentropic expansion from saturated vapour with end point denoted by 's'.

(Quoilin, 2007) states that isentropic fluids (such as R11) are preferred for low temperature Rankine cycles, as the expander work extraction is parallel to the line of isentropic expansion and pose a good fit when considering an ideal cycle. As the vapour expands along a vertical line on the T-s diagram, vapour saturated at the expander inlet will remain saturated throughout the expansion process without condensation.

For dry fluids with a positive slope saturation curve (such as R245fa), the fluid transitions to a superheated state after isentropic expansion from saturated vapour, which is advantageous as it avoids condensation and damage to the expander. However, depending on the vapour profile, this can also result in substantial superheat at the expander outlet, which causes inefficiency and requires additional cooling before entering a two-phase state. This imposes a larger cooling requirement on the condenser, or the integration of a regenerator between the expander exhaust and the working fluid pump, resulting in increased capital cost.

Wet fluids with a negative slope saturation curve (such as R22) become two-phase before the end of isentropic expansion, resulting in condensate which can damage the expander and reduces its isentropic efficiency. To compensate for this, a degree of superheating is required, which decreases cycle efficiency. Furthermore, due to the reduction in the heat transfer coefficient in the vapour phase, the heat transfer area requirement (and therefore the cost) of the evaporator increases significantly (Bao and Zhao, 2013).

The characteristic of maintaining saturated vapour throughout the isentropic expansion process, and the fact that there is no need for installing a regenerator (as would be recommended for certain dry fluids) makes isentropic fluids ideal working fluids for ORCs (Bao and Zhao, 2013). However, in a study modelling a realistic cycle, (Hung et al., 2010) indicate that wet fluids with very steep saturated vapor curves in T-s diagram have a better overall performance in energy conversion efficiencies than that of dry and isentropic fluids. The authors note these fluids are not always suitable for ORC systems when other thermo-physical properties are taken into consideration.

In their review of working fluids and expanders, (Bao and Zhao, 2013) report the cycle thermal efficiency is a weak function of the turbine inlet temperature. From the literature, they concluded it is not necessary for organic fluids to be superheated, and consequently optimum efficiency of ORC working with a dry fluid could be achieved without any superheating. However, in experimental studies such as (Declaye et al., 2013), a superheat degree of around 7 – 17 K is nevertheless imposed to ensure no condensing occurs, taking into account the potential for cold surfaces and ambient heat losses in the expander.

2.4.1.2 Thermo-physical properties

This section briefly outlines working fluid considerations and their influence on ORC design and operation, as summarised succinctly in (Quoilin et al., 2012). Of particular relevance to the current study are:

- Chemical stability:
  In contrast to water, organic fluids usually undergo chemical deterioration and decomposition at high temperatures. The maximum heat source temperature is therefore limited by the chemical stability of the working fluid.

- Safety considerations:
  The two main safety considerations are flammability and toxicity. The ASHRAE Standard 34 classifies refrigerants in safety groups and allows evaluation of a fluid's safety. Class A refrigerants are of a lower degree of toxicity, while Class B refrigerants are those of higher degree of toxicity. In experimental systems it is preferable to utilize a safer working fluid.
- Environmental considerations:
  Ozone Depletion Potential (ODP) is the relative amount of degradation to the ozone layer a fluid can cause, relative to R-11 which has a reference ODP of 1.0. Due to the restrictions imposed by the Montreal Protocol, non-zero ODP fluids such as R-11 and R-22 are progressively being phased out.
  Greenhouse Warming Potential (GWP) is a relative measure of how much heat a greenhouse gas traps in the atmosphere, compared carbon dioxide (whose GWP is standardized to 1). High GWP refrigerants such as R134a (GWP of 1400) are being phased out in favour of lower GWP fluids.
- Availability and cost:
  Depending on local legislation and supply considerations, working fluid availability and cost may be a constraining factor. For example, in New Zealand pure R245fa was not obtainable for experimental trials at the University of Canterbury despite being a popular and high performing refrigerant.

Additionally, the following working fluid properties are important to understand as they can influence system design and cost:

- Thermodynamic properties:
  The critical point, specific heat, and density of a fluid govern the thermodynamic performance, which determines cycle efficiency and output power for given heat source and heat sink temperatures.
- Vapour density:
  High vapour density is preferred, leading to lower volume flow rates and lower pressure drops in heat exchangers.
- Viscosity:
  Low viscosity in both liquid and vapour phase is preferred to maintain high heat transfer coefficients and minimise friction losses in heat exchangers.
- Thermal conductivity:
  High thermal conductivity is preferred, which results in high heat transfer coefficients and affects the size and cost of heat exchangers. The heat exchanger design has a large impact on the economic feasibility of an ORC, as described by (Budisulistyo et al., 2014).
- Evaporating and condensing pressures:
  The evaporating pressure impacts system design, as high pressures generally lead to higher equipment investment costs and increased system complexity. The condensing pressure should be higher than the atmospheric pressure to avoid air infiltration in the cycle.

2.4.1.3 Refrigerant R245fa

Refrigerant R245fa, which constitutes 50.3% of the working fluid used in the current study, is often employed in the literature reviewed in this chapter. It has relatively low environmental impact and

toxicity, is a dry working fluid theoretically requiring no superheating, and has favourable performance at low temperatures.

(Mago et al., 2007) conducted a second-law analysis for the use of organic Rankine cycle (ORC) to convert waste energy to power from low-grade heat sources. The authors simulated R245ca, R245fa, R134a, R113, R123, isobutane and propane as working fluids. Results indicate that R245ca and R245fa have superior thermal efficiency when the temperature of the heat source is between 380 K and 430 K (107 – 157 ^{o}C), which is approximately the expected temperature range for the current study.

Not all studies agree with this conclusion. (Lakew and Bolland, 2010) studied the performance of different working fluids utilizing a low-temperature heat source, considering a simple subcritical Rankine cycle. The working fluids considered are R134a, R123, R227ea, R245fa, R290, and n-pentane. The authors find R227ea gives the highest power for a heat source temperature range of 80 – 160 ^{o}C, while R245fa produces the highest in the range of 160 – 200 ^{o}C.

An alternative to using a pure working fluid is to combine fluids with favourable characteristics in a zeotropic mixture.

2.4.2 Zeotropic mixtures

The working fluid used in the current study is refrigerant HFC-M1, a zeotropic mixture of the two refrigerants R245fa and R365mfc (50.3/49.7 % on a weight percent basis respectively, Appendix C). This was selected in previous work by the research group, due to availability in New Zealand and favourable thermodynamic modelling, further detailed in section 4.1.3.

2.4.2.1 Zeotropic fluid fundamentals

A zeotropic mixture is a fluid mixture whose components have different boiling points. This gives the mixture a property called temperature glide, as the phase change occurs in a temperature range of about four to seven degrees Celsius, rather than at a constant temperature (Mohanraj et al., 2011). On the temperature-composition graph in Figure 2.3, the temperature glide can be seen as the temperature difference between the bubble point (saturated liquid temperature) and dew point (saturated vapour temperature). Upon boiling or condensing of a zeotropic mixture, the composition of the liquid and the vapour phase is dictated by the mixture's temperature-composition diagram.

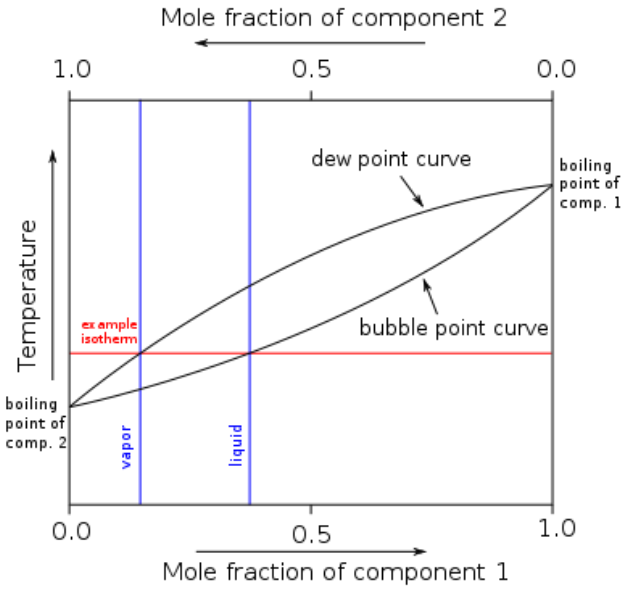

Figure 2.3 – Temperature-Composition diagram of a zeotropic mixture, demonstrating generic mixture definitions. Author (Padleckas, 2009), Licensed under Creative Commons Attribution CC BY-SA 2.5.

Research suggests zeotropic fluids may have a performance advantage over pure working fluids due to their temperature glide demonstrated in Figure 2.4. Tailoring of the constituent working fluids and their ratios allows customisation of the temperature glide, such that it better follows heat source and sink temperature profiles in the evaporator and condenser, reducing irreversibility and increasing efficiency (Bamorovat Abadi et al., 2015), (Liu et al., 2014).

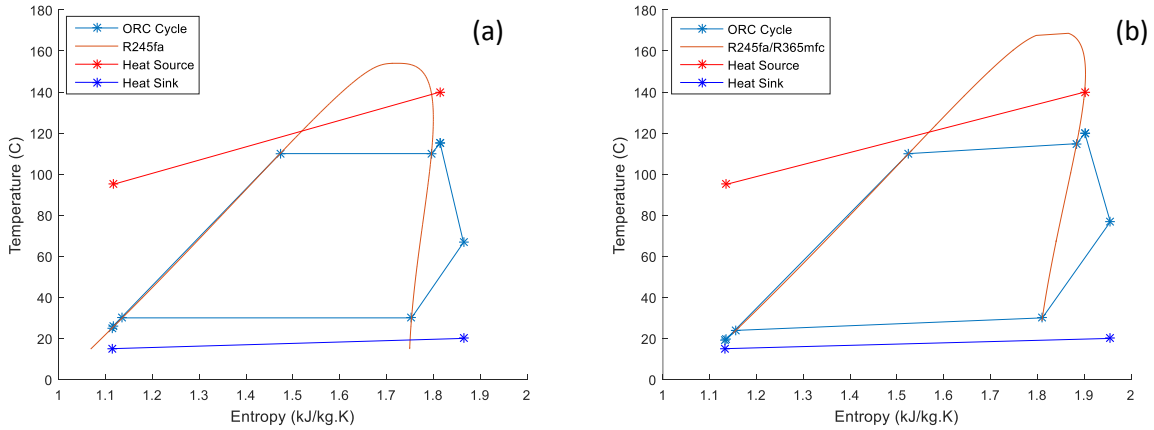

Figure 2.4 – Comparison of ORC demonstrating temperature glide of zeotropic mixtures, with (a) pure R245fa and (b) zeotropic mixture of R245fa/R365mfc in 50.3/49.7 ratio. Theoretical thermodynamic model values.

2.4.2.2 Zeotropic fluid performance in simulations

Numerous studies have been conducted into the effect of zeotropic fluids on cycle performance. Of these the majority involve the modelling of an ORC and simulating working fluid behaviour. The following studies outline the theoretical effects of zeotropic mixtures on cycle performance.

(Liu et al., 2014) studied the impact of zeotropic mixtures on cycle performance, specifically considering the effect of condensation temperature glide. They concluded ORC systems have better thermodynamic performance when the condensation temperature glide is nearly equal to the cooling water temperature increase.

In (Chys et al., 2012), the authors examine the effect of using zeotropic mixtures as working fluids in ORCs, simulating a realistic cycle. A mixture of R245fa/R365mfc in a 0.3/0.7 ratio was included amongst the working fluids. The authors concluded that for a heat source of 150 ^{o}C, using a zeotropic mixture improves the cycle thermal efficiency by 16% over the best pure fluid. However, this effect diminishes at higher temperatures, as for a heat source of 250 ^{o}C, only a 6% increase was modelled. This suggests zeotropic fluids may be more applicable for low temperature heat sources.

In (Yang et al., 2013) the authors conduct a simulation of zeotropic mixtures for an ORC using waste heat from the exhaust of a diesel engine. The selection of zeotropic mixture improved cycle efficiency by approximately 5%, from a cycle efficiency of 10.08% to 10.65%. The evaporating pressure exhibited a larger influence on thermal efficiency, with peak efficiencies occurring around 2.0 MPa.

In (Weith et al., 2014) report on studies previously carried out by their group (Heberle, 2013) which reports an efficiency increase of almost 16% for a geothermal application using mixtures of R245fa and R365mfc. However, the required heat transfer area of the evaporator and preheater for the most efficient mixture composition is 83% larger than that of the most efficient pure fluid. This is due to the highly reduced heat transfer coefficients of the R245fa/R365mfc mixture compared to its constituent fluids. In experimental trials, compared to the pure fluids, a reduction in the heat transfer coefficient of up to 50% is observed (Heberle and Brüggemann, 2013).

The authors in (Dong et al., 2017) investigate the performance of R245fa, R365mfc, R123, and R113 and their zeotropic mixtures as working fluids low temperature ORC. Additionally to cycle efficiency, the authors consider a measure of cost-effective performance as a comparison criteria. An increase in cycle efficiency of up to 18% over pure fluids is found. However, results indicate the zeotropic fluids persistently present lower cost-effective performance than pure fluids. This highlights the impact of zeotropic fluid's reduced heat transfer coefficients leading to larger heat exchangers and increased system cost.

2.4.2.3 Zeotropic fluid performance in experimental applications

During this literature review, it was noted very few groups experimentally test zeotropic fluids in small-scale ORCs. The following studies present the findings of those groups that conducted experimental tests.

In (Wang and Zhao, 2009) the authors present a theoretical analysis of low temperature ORCs using zeotropic mixtures, and find that further research may yield improved thermal efficiency and reduce capital cost. Subsequently in (Wang et al., 2010), the authors perform an experimental study using a solar collector heat source and a throttling valve in place of an expander. The cycle performance of pure R245fa, and zeotropic mixtures of R245fa/R152a in 0.9/0.1 and 0.7/0.3 ratios were compared. In the results the collector and cycle thermal efficiency of zeotropic mixtures were comparatively higher than pure fluid R245fa, which indicated that zeotropic mixtures had potential improvement for overall efficiency.

In (Li et al., 2015), the authors experimentally compare the effect on ORC performance of pure R245fa and a zeotropic mixture of R245fa/R601a in a 0.72/0.28 ratio. The system uses a 500 W scroll expander. The authors conclude the zeotropic mixture exhibits higher performance, with the highest thermal efficiency for R245fa and R245fa/R601a being 4.38% and 4.45% respectively. However, this 1.6% increase is well within their stated experimental error margin of 4.9%.

The authors in (Bamorovat Abadi et al., 2015) test a zeotropic mixture of R245fa/R134a in 60/40 molar ratio, comparing performance to pure R245fa, using the same expander as the current study. The results indicate the zeotropic mixture increased power output over the pure fluid at lower pressure ratios and heat sources between 80 – 100 ^{o}C. However, the pure fluid achieved higher maximum performance, detailed in section 2.7.1.

The authors compare experimental results to a model of composition shift, due to the differential liquid hold-up in the two-phase flow. The analysis suggests the circulating mixture had a different concentration compared to the charged composition. The degree of composition shift was dependent on the operating conditions. The authors believe the composition shift of the zeotropic mixture to be one of the main reasons why the predicted values were overestimating the performance of the ORC system.

Through the results of their study, Bamorovat et al have identified an important potential drawback of zeotropic fluids to be the unknown effects of composition shift of the mixture components. This can cause unpredictable behaviour and uncertainty in modelling of fluid properties for calculations. Furthermore, zeotropic mixtures can result in increased complexity for system material compatibility considerations.

2.5 Scroll Expander

The expander used by the current study is a commercially available 1 kW, oil free, scroll expander designed by AirSquared (model E15H22N4.25, part # E15H022A-A03).

Scroll expanders have been gaining popularity as the expanders in small-scale ORCs, due to their mechanical simplicity, relatively low cost compared to alternative expander options, and lack of possible turbine expander options. Analyses of the working principles and the characteristics of various expanders led the authors in (Qiu et al., 2011) to the conclusion that scroll expanders are a good choice for 1 – 10 kW ORC-based systems. While there are a number of commercially available scroll expanders, they are relatively more expensive than commonly available scroll compressors used in refrigeration and air conditioning. As such, several authors of experimental studies used scroll compressors modified to work in reverse as expanders, detailed further in section 2.7.

In comparison to other positive displacement expansion devices, the scroll expander has the most complicated geometry to manufacture (Bao and Zhao, 2013). Furthermore, the scroll's fixed volumetric expansion ratio limits the allowable expansion ratio in operation and therefore its application (Ma et al., 2016). However, the following qualities make it a good candidate for small-scale ORC systems:

- Low volumetric flow rate, high pressure ratios (Lemort et al., 2012).
- High isentropic efficiency, typically in the range of 65 – 75% ((Bamorovat Abadi et al., 2015), (Declaye et al., 2013)).

- Mechanical simplicity, with no inlet/outlet valves or gears. This leads to fewer moving parts than reciprocating positive displacement designs, and consequently high reliability and robustness (Ma et al., 2016).
- Low rotational speed (2000 – 3600 RPM) and pure rotational motion resulting in low noise and vibration, and removing the need for a gearbox for electrical generation (Bao and Zhao, 2013).
- Unlike turbine expanders, these machines can theoretically tolerate two-phase conditions, which may be present at the end of expansion in some operating conditions during experiments (Lemort et al., 2009).
- Turbine expanders for refrigerants are simply not available, and the specific speed in the 1 kW range would be extremely high.
- Coupling of the expander to a generator or other load has already been accomplished by the AirSquared unit, which is sealed. Sealing a turbine shaft is a large problem.

2.5.1 Operating principle

Common to positive displacement devices, the scroll expander is characterized by a built-in volumetric expansion ratio, and fixed displaced volume per rotation (Bao and Zhao, 2013).

The scroll expander is composed two scrolls, one fixed and one which orbits eccentrically without rotating. The operation of the scroll expander includes three processes: suction, expansion and discharge. The high pressure fluid flows into the suction chamber through the intake port, expands by rotating the orbiting scroll, and flows out from the exhaust port after expansion (Guangbin et al., 2010), shown in Figure 2.5.

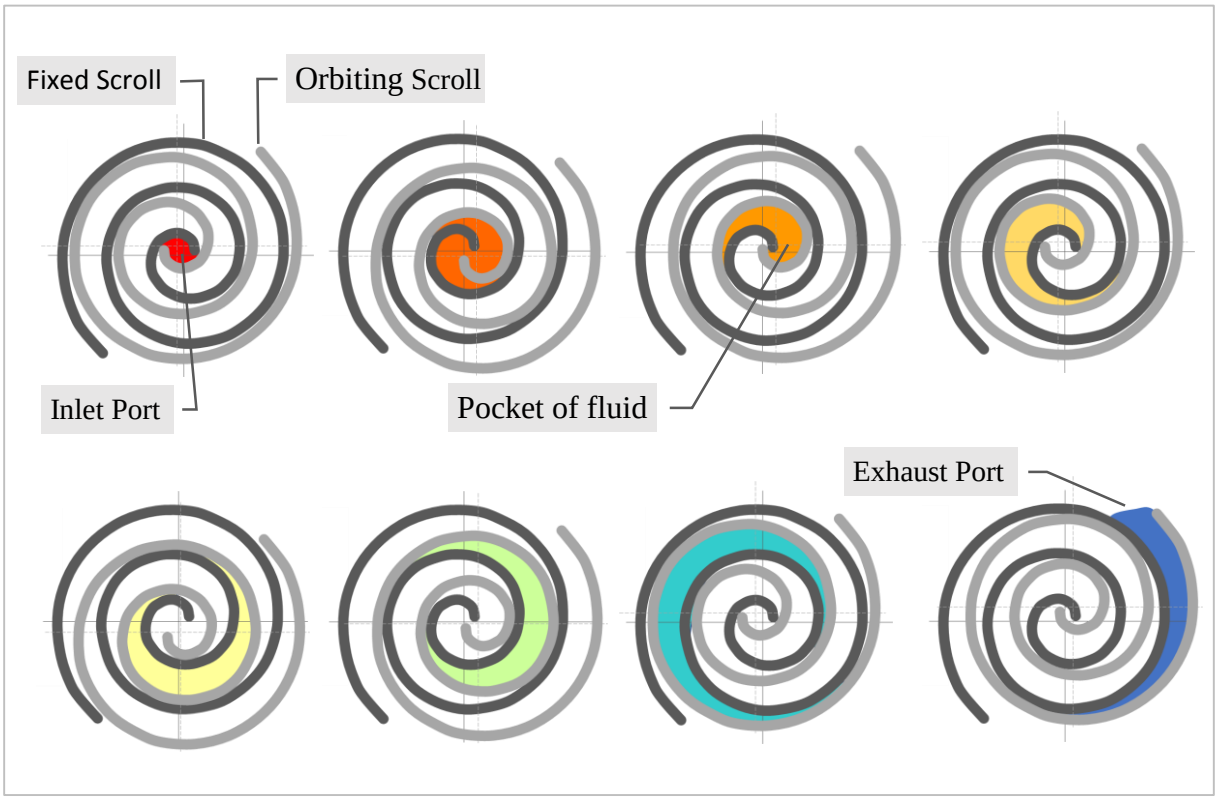

Figure 2.5 – Scroll expander operating process.

2.5.1.1 Scroll lubrication

Scroll expanders fall into two categories: compliant and kinematically constrained. Compliant scrolls require lubrication to operate efficiently without causing significant wear, while constrained scrolls in contrast can operate without lubrication (Bao and Zhao, 2013). Lubricated scrolls have reduced friction between the two scrolls and a reduced leakage area (Quoilin, 2007). However, oil-free expanders have several advantages over lubricated expanders. Lubrication raises several issues such as the necessity to avoid undesired oil traps, the reduction of the heat transfer coefficients in the heat exchangers, oil return issues at start up, and oil degradation at high temperatures (Declaye et al., 2013).

2.5.2 Performance losses

The following sections outline some of the various loss pathways of the scroll expander, which impact the expander's performance.

2.5.2.1 Built in volumetric expansion ratio losses

The built-in volumetric ratio can generate two types of losses if the system specific volume ratio is not equal to the expander nominal volume ratio: under expansion and over expansion (Bao and Zhao, 2013). These losses can considerably reduce the efficiency of the expansion process, with under expansion having the larger impact (Li et al., 2015).

The optimal isentropic efficiency of the scroll expander is in part determined by the machine's volumetric expansion ratio. However, despite this ratio being fixed, (Declaye et al., 2013) experimentally determine the pressure ratio that maximizes isentropic efficiency is not constant for all rotational speeds. Instead, this ranges from 3.42 at 2000 rpm to 4.33 at 3500 rpm for a scroll expander that had a built in expansion ratio of 3.95. This corroborates earlier numerical results in (Lemort et al., 2012), which indicate this shift of the optimum pressure ratio is due to additional influences such as mechanical losses, internal leakage losses, ambient heat exchange, and supply pressure drop in the inlet port.

2.5.2.2 Mechanical losses

Mechanical losses primarily arise from two sources: the main bearing and auxiliary crank mechanisms that support the revolving motion of the orbiting scroll, and friction between the orbiting and the fixed scrolls. (Lemort et al., 2009) observed that the mechanical loss torque is neither a function of the suction pressure nor of the rotational speed. However, the authors in (Ma et al., 2016) developed and experimentally validated a scroll expander model and noted that their proposed overall frictional loss coefficient increased with pressure difference.

2.5.2.3 Internal leakage losses

The two types of leakage losses in a scroll expander are flank leakage (δ_f), and radial leakage (δ_r) which are a result of necessary clearances between the orbiting and fixed scrolls, shown in Figure 2.6. The leakage reduces the output power of the scroll expander, with the fluid flowing directly from the high pressure region to the low pressure region without producing any useful work (Quoilin, 2007). Leakage losses are often larger in magnitude than mechanical losses, and leakage

losses become increasingly significant as the expander rotational speed decreases (Lemort et al., 2009), (Ma et al., 2016).

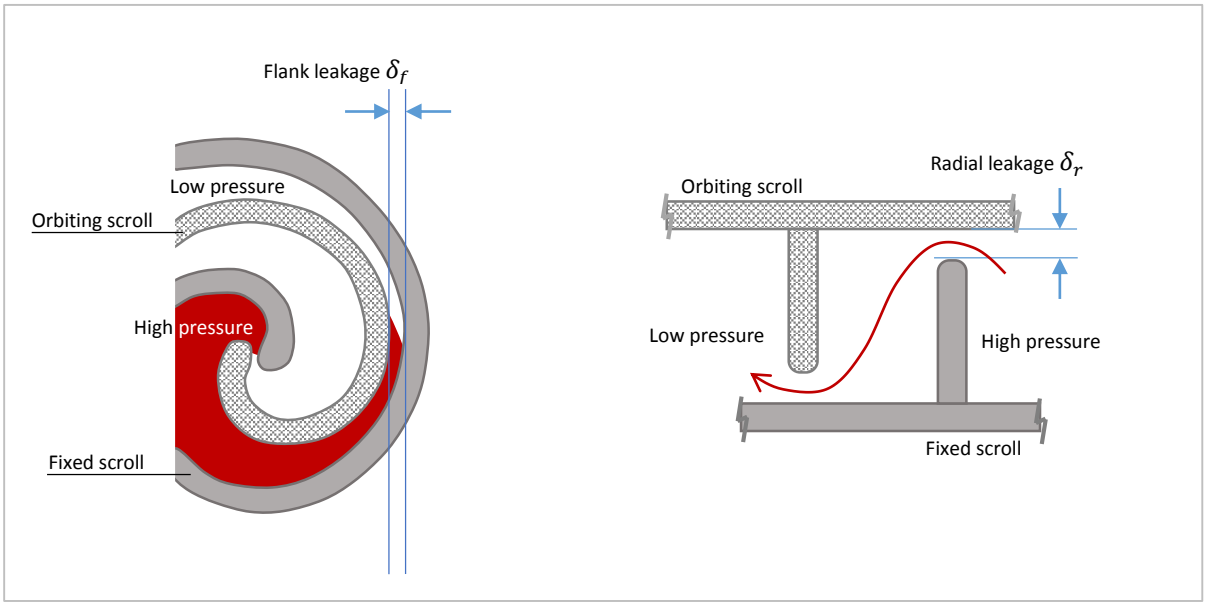

Figure 2.6 – Simplified schematic of leakage pathways in a scroll expander.

2.5.2.4 Other losses

Other significant losses include ambient heat transfer losses and supply pressure drop losses. As the working fluid moves through the scroll, useful heat is lost to the surroundings as heat transfer occurs between the fluid and the scrolls (Guangbin et al., 2010). Supply pressure drop losses occur as the high pressure fluid enters the inlet port to the suction chamber. (Lemort et al., 2009) state the pressure drop is an inherent characteristic of the scroll expander, which may be able to be reduced through modelling and modifying the expander geometry.

2.6 Modelling

The following sub-sections outline some applications of detailed ORC models and simple thermodynamic simulations in reviewed literature. It highlights that while undoubtedly useful, in depth models are difficult to develop and experimentally validate, and that for initial design and testing of small ORC systems a thermodynamic cycle simulation is often sufficient.

2.6.1 Detailed component modelling

In depth modelling of the ORC and its components is the focus of several in depth studies and working groups. Such theoretical models allow investigation of control and optimisation strategies, and identification of inefficiencies during operation. Of the detailed models, the following are of particular interest to the current study, albeit unfeasible to implement at this stage. Nevertheless, they highlight the benefit of such models in potential future work.

Utilized in several studies is the lumped parameter scroll model developed by the authors in (Lemort et al., 2009), which is further refined and implemented in their subsequent works. The semi-empirical model of the expander is based on experimental results and derived from one proposed by (Winandy et al., 2002).

The scroll model identifies eight parameters, and predicts the mass flow rate, shaft power and working fluid exit temperature with good accuracy. The maximum deviation between model predictions and experimental measurements is 2% for the mass flow rate, 5% for the shaft power and 3 K for the discharge temperature. The model of the expander is used to quantify the different losses, and identifies internal leakage as responsible for the major part of the performance losses. It indicates how modifying the expander geometry might achieve better performances. The model could also be used as a pre-design tool for estimating the main characteristics of an expander.

Another detailed and generic scroll model is presented in (Ma et al., 2016), which can be tailored to the geometry of a specific scroll expander. The model was experimentally validated using the same 1 kW scroll expander used in the current study, and produced a good agreement between experimental and simulated results.

In (Quoilin et al., 2011) and (Desideri et al., 2016), the authors present the applications of dynamic models in the ThermoCycle Modelica library for modelling of low capacity ORC systems. The ThermoCycle Modelica library aims at providing a robust, efficient and fully open-source simulation environment targeting the modelling of thermal plants. Evaluation of fluid properties is handled by CoolProp. Quoilin et al. develop a dynamic model of a small-scale Organic Rankine Cycle, and demonstrate the importance of a proper control strategy to prevent rapid declines in cycle performance. Desideri et al. validate their own proposed ORC model with experimental data, and showed a good overlap between experimental and simulated results for all but extremely off-design conditions.

2.6.2 Thermodynamic simulation

While the above studies show the benefit of detailed component models, these are time consuming and arduous to develop and experimentally calibrate. The reviewed literature of experimental systems similar to the current study, indicates that when designing and testing a small-scale ORC, simple thermodynamic cycle simulations are sufficient. These simulations allow investigation of component and working fluid selection, cycle performance estimation, and as a comparison for experimental performance.

In studies where a standard thermodynamic analysis is carried out, equations of mass and energy balances across components are coupled with assumptions that simplify the simulations. These assumptions often include (Galloni et al., 2015):

- All thermodynamic processes are in steady state.
- No pressure drops considered both in the evaporator and in the condenser.
- Constant isentropic efficiencies for expanders and pumps.
- Perfectly insulated system, no heat transfer to surroundings.

In (Galloni et al., 2015), the authors use such a thermodynamic simulation to predict performance of a 1 kW Rankine cycle operating with R245fa. Thermodynamic data of the working fluid is calculated by means of the CoolProp libraries, a cross-platform, open-source, alternative to NIST Reference Fluid Thermodynamic and Transport Properties Database (REFPROP).

In (Baral et al., 2015) the authors simulate a 1 kW ORC using the Engineering Equation Solver (EES). EES uses a built in fluid property library, and is well suited to thermodynamic equation solving. (Bamorovat Abadi et al., 2015) also implement thermodynamic equations in EES to model the performance a 1 kW ORC, using experimental conditions as input variables. They find the model predicts performance well for the ORC using pure R245fa as a working fluid. However, the simulation over-estimates system performance compared to experimental values when considering a zeotropic mixture of R245fa and R134a.

The authors in (Muhammad et al., 2015) perform a cycle simulation using Cycle-Tempo software (ASIMPTOTE, 2016), a commercially available software package which allows analysis of thermodynamic cycles. Muhammad et al. experimentally validate the design of their 1 kW system, and observe the results of different operating conditions, with reasonable agreement between simulation and experimental results.

The current study adopts a similar strategy to the above studies, simulating a simple thermodynamic cycle. This is achieved using REFPROP v 9.0 (Lemmon, 2013) as working fluid property library, in conjunction with MATLAB 2016b, detailed in section 3.1.

2.7 Small scale ORC in Literature

There has been a notable increase in interest in small-scale ORCs since 2006, with higher volumes of papers published on the subject each year. Figure 1 in (Yang et al., 2017) reports an increase in published works on the topic from 15 in 2006 to over 450 in 2014. Several groups of authors in the field are developing experimental small ORCs and corresponding theoretical models.

2.7.1 Systems utilizing 1 kW scroll expander from Air squared

The literature survey yielded five publications utilizing the same 1 kW scroll expander as the current study: (Muhammad et al., 2015) ,(Bamorovat Abadi et al., 2015), (Baral et al., 2015), (Eicke and Smolen, 2015), and (Galloni et al., 2015).

In the study by (Muhammad et al., 2015), the authors present a very similar experimental setup to that used by the current study (which was originally built and published in 2014). Using R245fa as a working fluid and 1 to 3 bar waste steam as a heat source, the authors system also used light bulbs of identical wattage as electric load dissipation. Therefore, the results of Muhammad et al. provide a useful comparison for the current study. The maximum electrical power output was 1 kW with 0.84 kW of net electrical power. The maximum cycle efficiency was 4.7 %, and the maximum expander isentropic efficiency obtained was 77.7%.

The authors in (Bamorovat Abadi et al., 2015) utilize a hot water heat source, and test a zeotropic mixture of R245fa/R134a in 60/40 molar ratio, comparing performance to pure R245fa. The results indicate the zeotropic mixture increased power output over the pure fluid at lower pressure ratios and heat sources between 80 – 100 ^{o}C. However, the pure fluid achieved higher maximum performance. With the zeotropic mixture, the maximum power produced was 1.2 kW, a maximum cycle efficiency of 6.5%, and expander isentropic efficiency of 65%. Using the pure working fluid, the maximum power produced was 1.4 kW, a cycle efficiency of 7%, and expander isentropic efficiency of 70%.

In (Baral et al., 2015), the authors utilize a similar experimental configuration to the current study, and R245fa as a working fluid. The ORC is designed to be used for small-scale solar concentrated power. The results of experimentally varying different operating parameters, such as the evaporating and condensing pressures, degree of superheating, and pressure ratio are illustrated. Exergy efficiency, cycle efficiency, and expander isentropic efficiency are considered as performance metrics. From the experimental results, the maximum expander power output was 1.4 kW with the expander's rotating speed of 3600 RPM and inlet pressure of 13 bar. The thermal efficiency of the corresponding condition was 8.55% with a maximum pressure ratio of 5.9. The maximum isentropic efficiency of the expander was found to be 70%.

The authors in (Eicke and Smolen, 2015) begin to develop a ORC demonstration system utilizing an electric oil heater heat source and R245fa working fluid. Due to a lack of component availability, only compressed air tests of the scroll expander are presented. These demonstrate a voltage output anomaly in the magnetically coupled AC generator that is utilized with this scroll expander and in the current study. The authors calculate that such a small-scale system is not economically viable for electrical power production, based on German energy prices and market conditions in 2015.

In (Galloni et al., 2015), the authors build and test an experimental system, utilizing a custom hot water boiler as the heat source and R245fa as the working fluid. The mass flow rate of the working fluid is not directly measured, rather it is inferred via an energy balance on the condenser. Furthermore, neither the shaft power nor the electrical generated power of the scroll expander is directly measured, opting instead for a thermodynamic analysis of the expanded working fluid. This introduces an unknown degree of uncertainty in the obtained results. The heat source temperature was varied from 75 – 95 ^{o}C, the cold sink temperature ranged between 20 – 33^{o}C, and the evaporating pressure ranged from
6 – 10 bar. The maximum effective electrical power was 1.2 kW, and a maximum cycle efficiency of approximately 9 % was achieved.

2.7.2 Other small (< 10 kW) scroll expander systems

The following section presents small-scale experimental scroll expander ORC systems relevant to the current study. These provide useful benchmarks for similar system performance, testing methodologies, and result interpretation.

(Eyerer et al., 2016) tested the applicability of using refrigerant R1233zd-E as a drop-in replacement for R245fa in an existing 500 W scroll expander ORC system. In contrast to R245fa, R1233zd-E has almost no Ozone Depletion Potential, and significantly smaller Global Warming Potential. To compare the performance of the working fluids the paper evaluates system parameters such as cycle efficiency and power output. Furthermore, the study experimentally investigates the influence of process parameters of mass flow rate, condensation temperature and expander rotational speed. R1233zd-E was found to be a suitable substitute for R245fa, with a 6.9% higher maximum thermal efficiency (5.1 %), but 12.2% lower maximum gross power.

(Woodland et al., 2012) experimentally study a small automotive scroll compressor modified to run in reverse as an expander with R134a as a working fluid. The scroll achieves a maximum isentropic efficiency of 0.72, and the filling factor ranged from 2 to 0.83. The authors found the isentropic efficiency of the expander can be fully characterised by its filling factor and the expansion volume

ratio imposed across it. In particular, the peak isentropic efficiency occurs near a filling factor of unity and an expansion volume ratio near the built-in volume ratio of the expander.

In (Bracco et al., 2013), the authors design, test and model a 1.5 kW ORC prototype. The system uses a modified air conditioning scroll compressor as an expander, R245fa as a working fluid, and an electric boiler as a heat source. The cycle achieved a maximum net cycle efficiency of around 8%, a maximum power output of 1.5 kW, and the scroll achieved a maximum isentropic efficiency of 73%.

In (Quoilin, 2007), the author designs, fabricates, and experimentally tests a small ORC. The system utilizes a scroll expander and R123 as a working fluid, with hot air ranging from 150 ^{o}C to 200 ^{o}C as the heat source. The maximum gross electrical power was 1.8 kW, achieving a cycle efficiency of 7.4 %, and the expander reached a peak isentropic efficiency of 68 %. After experiencing refrigerant leakages and observing this led to decreased power output, the system was modified to allow control over the quantity of refrigerant in the system. The results suggest the refrigerant charge has a large influence on the performance of the system.

In (Lemort et al., 2009), the authors present the results of an experimental study of a prototype ORC using an open-drive oil-free scroll expander and refrigerant HCFC-123 as the working fluid. The maximum delivered shaft power is 1.82 kW and the maximum achieved overall isentropic effectiveness is 68%.

In (Lemort et al., 2012), the authors present the results of an experimental study on the performance of a hermetic scroll expander, modified from a heat pump compressor, and R245fa as a working fluid. Performance of the expander is evaluated in terms of isentropic effectiveness and filling factor as functions of the main operating conditions. The expander exhibited good volumetric performance, with a maximum isentropic efficiency of 71 % and filling factors from 1.04 – 1.11.

In (Declaye et al., 2013) the authors present an experimental characterization of an open-drive scroll expander integrated into an Organic Rankine cycle, using R245fa as the working fluid. The expander is a commercially available air compressor modified to operate as an expander. The maximum isentropic efficiency and shaft power are 75.7 % and 2.1 kW respectively, while a maximum cycle efficiency of 8.5% is achieved. Results show that isentropic efficiency exhibited an optimum at each expander speed and inlet pressure, while shaft power was a monotonically increasing function of the pressure ratio. The authors attribute this to the pressure ratio applied to the expander compared to the built in volumetric ratio, and the impact of the corresponding constant volume expansion.

The authors in (Yang et al., 2017) present an experimental study of a 3 kW ORC system using an open-drive scroll expander and R245fa as the working fluid. The expander is a modified hermetic refrigerant scroll compressor with a built in volume ratio of 3.24. The system utilises a 40 kW electric oil heater as a heat source. The maximum expander shaft power, electrical power, thermal efficiency and system electrical efficiency are 2.64 kW, 1.89 kW, 5.92% and 3.93%, respectively. The expander reaches a peak isentropic efficiency of 79%. This study presents an exemplary experimental setup, with direct measurement of all variables.

2.8 Working fluid volume filling fraction

The current study is motivated by the following consideration:

1. That the working fluid volume charged into the system influences heat exchanger performance in either the evaporator or condenser.
2. This heat exchanger performance affects the net rate of heat transfer to the working fluid.
3. That this in turn influences cycle performance (efficiency and net power output), and the flexibility of the system to accommodate a wider range of operating conditions.

Very little literature was found that directly tests the impact of working fluid charge on operational performance.

The author in (Quoilin, 2007) designed and built a 1 kW scroll expander ORC with R-123 as the working fluid, compared models to experimental results, and varied the refrigerant charge. They found that the refrigerant charge has a tremendous importance in the behaviour of the cycle and that its optimal value has to be found in order to maximize the performance.

In (Li et al., 2015), the authors designed and built a 500W scroll expander ORC, compared performance of r245fa with a r245fa/r601a mixture, and investigated the effect of working fluid charge on operational performance. In the study, the authors propose to characterize the working fluid charge, using the Dimensionless Volume Ratio (DVR) as a metric, shown in equation (2).

$$DVR = \frac{V_{wf}}{V_{sys}} \tag{2}$$

The DVR is defined as the ratio of the volume of the liquid working fluid in the system V_{wf} to the total internal volume of the working fluid circuit V_{sys}.

Li et al. found the expander isentropic efficiency monotonically decreased with increasing DVR for both fluids, but each had a slightly different response. Power output monotonically decreased with decreasing DVR for both fluids in approximately the same manner. However, the cycle thermal efficiency demonstrated a peak with changing DVR – the location of this peak was specific to each working fluid tested.

The results of these studies motivate the current study to investigate the effect of the working fluid charge (DVR) on system performance. Specifically it seeks to corroborate the findings of Li et al. by investigating the existence of a DVR value that results in a maximum cycle thermal efficiency, and a monotonic decline in power with decreasing DVR. Simultaneously, the effect of the DVR on the system's range of allowable operating conditions will be able to be assessed.

2.9 Testing methodologies in literature

The following section presents studies which both clearly articulate their testing methodology and produce high-quality data sets from experiments. These, along with elements of studies in section 2.7, inform the testing methodology implemented by the current study, outlined in section 4.4.

The metrics commonly used to assess system performance of scroll based ORC in the reviewed literature are listed below. Where these are used in the current study, they are defined in Chapter 5:

- Gross and net power output
- Cycle efficiency
- Second law efficiency
- Expander and pump isentropic efficiencies
- Expander filling factor

(Galindo et al., 2015) presents the experimental analysis of a 2 kW ORC operating on the waste heat of a 2 litre turbocharged gasoline engine. The study aims to determine the influence of the controllable input parameters, an initial aim of the current study. The authors achieve this by changing one parameter at a time while holding the remainder constant. The resulting 28 steady state points provide a high-quality set of data, with clearly visible trends.

Over three studies, Bernado Peris et al. document the laboratory testing of a now commercially available 20 kWe ORC system provided by Rank®, and compare this performance with results from its subsequent installation in an industrial application (Peris et al., 2015a, Peris et al., 2015b, Peris et al., 2015c). The authors demonstrate a robust and repeatable testing methodology that yielded comparable results in both settings. In (Peris et al., 2015a) the performance of the ORC is experimentally characterized by analysing thermal power input, gross and net electrical powers, electrical cycle efficiencies and expander effectiveness. The ORC was tested by varying the thermal oil inlet temperature, thereby applying thermal power inputs simulating different loading scenarios.

The authors in (Declaye et al., 2013) experimentally demonstrate that if ambient heat losses are neglected, scroll expanders can be modelled by their isentropic efficiency and filling factor. This paper stands out because of the high degree of control and sensory equipment, leading to a high-quality data set that clearly shows trends and relationships between the parameters. The operating parameters that are varied include the inlet pressure (from 9 to 12 bar), outlet pressure (from 1.5 to 4 bar) and expander rotational speed (from 2000 to 3500 rpm). The operating parameters are achieved by adjusting the expander RPM, mass flow rate of cooling water in condenser, and mass flow rate of the refrigerant. A total of 74 steady state operating points are achieved.

In (Desideri et al., 2016) the authors also show the expander efficiency to be a function of the expander inlet pressure, expander rotational speed, and the expander pressure ratio. As such, these are useful to investigate the expander efficiency in experimental results.

2.9.1.1 Throttling valve in lieu of expander

During experiments in the current study, the expander experienced premature failure. In order to continue testing, a needle valve in the bypass line was used in place of the expander. This approach is also demonstrated in literature. In (Shu et al., 2016), the authors employ an expansion valve in the

place of the expander which was under design. This allows adjustment of the evaporating pressure and allows simulation of the expander. The authors in (Wang et al., 2010) use an expansion valve instead of an expander. They perform a thermodynamic analysis to simulate the power production of an expander in the cycle, using measured inlet and outlet expansion pressures and assuming an 85% efficient expansion process.

2.9.1.2 Methods for testing DVR

In (Li et al., 2015) the authors experimentally test the effect of changing DVR on performance. The DVR varies from 0.51 – 0.32 and presents a demonstrable influence on cycle efficiency, cycle net power and isentropic efficiency. The implications of a certain DVR on the fluid liquid level in the heat exchangers in a specific system is dependent on the physical layout of components. However, this range presents a reasonable starting range for testing and is implemented in the current study, detailed in section 4.4.4. The authors repeat a set of 10 tests at each DVR, varying the heat source temperature, which yields a sufficient resolution of data to allow clear observation of trends.

2.9.2 Steady state specification and identification

The following section outlines criteria and methods for identifying steady state operation in small-scale ORCs.

In (Woodland et al., 2012) data for the experimental steady state ORC tests is presented according to a proposed steady state standard. In this standard, data collected in a 30 second buffer is averaged and compared to another 30 second buffer taken approximately 10 minutes earlier. The absolute difference or percent change between the two averages is computed for each measurement, and compared to the following set of criteria in Table 2.4.

Table 2.4 – Comparison criteria for each measurement satisfying steady state conditions (Woodland et al., 2012)

Measurement	**Steady state criteria**
Temperature	Difference < 0.5K
Pressure	Change < 2%
Working fluid mass flow	Change < 2%
Rotating equipment speed	Change < 2%

In (Peris et al., 2015a), steady state operation was satisfied when all measured variables, sampled at 1 Hz, were within a fluctuation range lower than 1% for 15 minutes. The data of the final 10 minutes of steady state was then averaged to generate an operating point. 10 steady state operating points were achieved.

In (Donald L. Simon, 2010), the authors present a data filter for identifying steady-state operating points in engine flight data. The algorithm automatically identifies and extracts steady-state engine operating points from engine flight data.

The generic-approach state transition logic is implemented in MATLAB. It incorporates low pass filters, standard deviation calculations, and implementation strategies. Operating regime conditional statements are specified for relevant data, consisting of standard deviation tolerances and absolute values.

The state transition logic has three states it can transition between when processing incoming data: buffer initial window of data, sliding buffer window of non-steady-state data, and expanding buffer window of steady state data. A similar approach is used by the current study, in conjunction with other experimental ORC works which inform selection of conditional statements, detailed in section 4.5.2.

2.9.3 Experimental uncertainty

The majority of experimental systems in the reviewed literature present a table of measurement uncertainties for each considered system parameter. In (Bracco et al., 2013), the authors demonstrate the calculations for error analysis in the experimental measurements of their small-scale ORC, notably the handling of enthalpy error estimation when using REFPROP as a reference fluid library. The authors derive an expression that incorporates the relative error introduced with the Lemmon-Span equations (Lemmon and Span, 2006). These calculations form the basis for the error analysis performed in the current study, which uses REFPROP 9.0 for the experimental data analysis.

Chapter 3 ORC Modelling

Chapter three presents the application of thermodynamic first principles to the ORC system. Design inputs are used to provide a benchmark for system operation, allowing evaluation of experimental results in later sections.

3.1 Cycle thermodynamic simulation

One of the initial goals of this research was to investigate the suitability of component selection, through assessing the system performance and comparing to theoretical design points. This required developing a cycle model to ascertain the system parameters of cycle efficiency, power output and heat transfer, given an informed set of input operating conditions.

Developing in depth component models was beyond the scope of this research, so the simplest component and thermal system model of the ORC system was developed using fundamental laws of mass and energy conservation. The equations presented were solved in MATLAB 2016b, using REFPROP 9.0 as fluid reference library. This system model was then adapted to receive experimental temperature and pressure data as inputs, allowing evaluation of the ORC performance compared to a theoretical case in section 5.2.3.

3.1.1 Theoretical cycle

Figure 3.1 presents the T-s diagram of the theoretical organic Rankine cycle of the system at the designed operation parameters, with the processes outlined in Table 3.1.

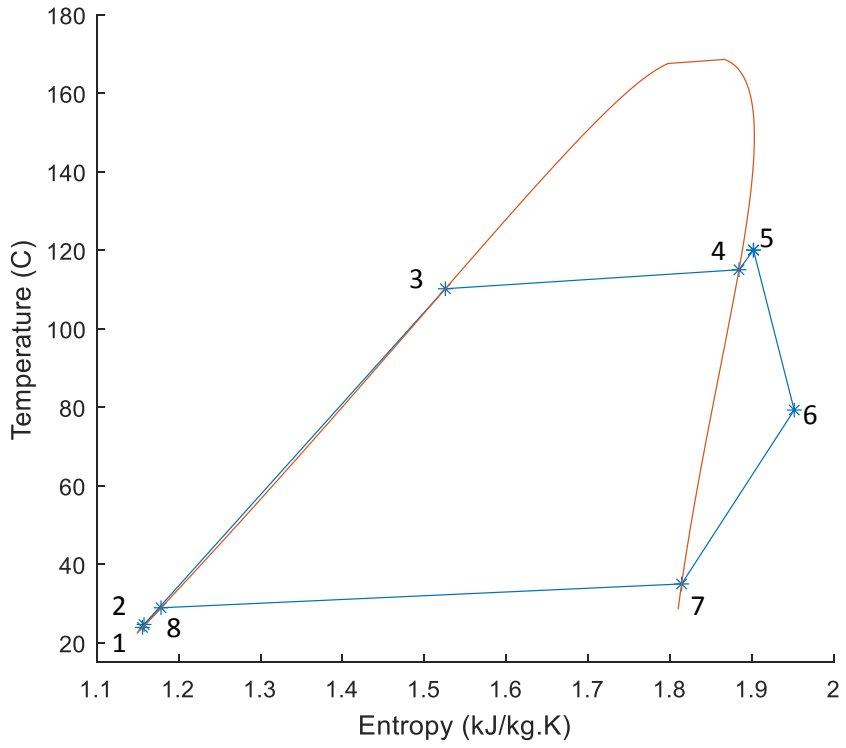

Figure 3.1 – Temperature-entropy diagram of the theoretical organic Rankine cycle with HFC-M1 refrigerant mixture

Table 3.1 – ORC processes as presented in Figure 3.1

Component	Symbol	Stage	Process
Pump	$\dot{W}_{pump,wf}$	1 – 2	Work input by working fluid pump
Evaporator	$\dot{Q}_{evap}$	2 – 3	Preheating of working fluid in the evaporator
		3 – 4	Phase change of the working fluid
		4 – 5	Superheating of the working fluid
Expander	$\dot{W}_{exp}$	5 – 6	Work output by expansion between imposed pressures
Condenser	$\dot{Q}_{cond}$	6 – 8	Condensation of the working fluid
		8 – 1	Subcooling of the working fluid

3.1.2 Cycle equations

Mass, energy, and entropy balance equations are written for all cycle components and for the overall cycle, assuming steady state operation, shown in equations (3) and (4).

Mass balance

$$\sum \dot{m}_{in} = \sum \dot{m}_{out} \tag{3}$$

Energy balance

$$\sum \dot{m}_{in} h_{in} + \sum \dot{Q}_{in} + \sum \dot{W}_{in} = \sum \dot{m}_{out} h_{out} + \sum \dot{Q}_{out} + \sum \dot{W}_{out} \tag{4}$$

The balance equations are coupled with the definitions of isentropic efficiency for the pump ($\eta_{s,pump}$) and expander ($\eta_{s,exp}$) to model the theoretical cycle processes. These are presented in Table 3.2. The equations are based on the following assumptions:

- Changes in kinetic and potential energies are negligible.
- All components are perfectly insulated such that heat transfer only occurs between fluid streams in heat exchangers.
- Working fluid exits the evaporator as a superheated vapour.
- Working fluid exits the condenser as a subcooled liquid.
- Negligible pressure losses in fluid flow through system components such as lines and heat exchangers.

In addition to Table 3.2, cycle states 5 and 1 are achieved by specifying a degree of superheating (T_{sup}) and subcooling (T_{sub}), shown in equations (5) and (6).

- $$T_5 = T_4 + T_{sup} \tag{5}$$

- $$T_1 = T_8 - T_{sub} \tag{6}$$

Table 3.2 - Thermodynamic equations used in calculating the theoretical cycle.

Process stages	**Component**	**Assumptions**	**Inputs**	**Conservation of Energy**	**Irreversibility**	**Outputs**
1 - 2	Fluid Pump	Constant isentropic efficiency	$\dot{m}, P_1, T_1, \eta_{s,pump}, P_2$	$\dot{W}_{pump,wf} = \dot{m}(h_1 - h_2)$	$\eta_{s,pump} = \frac{h_1 - h_{2s}}{h_1 - h_2}$	$T_2, h_2, \dot{W}_{pump,wf}$
2 - 5	Evaporator	Isobaric $P_5 = P_2$	$\dot{m}, P_2, T_2, \dot{m}_{tf}$	$\dot{Q}_{evap} = \dot{m}(h_5 - h_2)$	N/A	$T_5, h_5, \dot{Q}_{evap}$
5 - 6	Expander	Constant isentropic efficiency	$\dot{m}, P_5, T_5, \eta_{s,exp}$	$\dot{W}_{exp} = \dot{m}(h_5 - h_6)$	$\eta_{s,exp} = \frac{h_5 - h_6}{h_5 - h_{6s}}$	$P_6, h_6, \dot{W}_{exp}$
6 - 1	Condenser	Isobaric $P_1 = P_6$	$\dot{m}, P_6, T_6$	$\dot{Q}_{cond} = \dot{m}(h_1 - h_6)$	N/A	$P_1, h_1, \dot{Q}_{cond}$

3.1.3 Thermodynamic analysis definitions

The experiments measure electrical power for both expander and pump. In order to compare the results of the thermodynamic simulation with values from experiments, equations (7) and (8) are used estimate the electrical expander and pump work ($\dot{W}_{exp,e}$ and $\dot{W}_{pump,wf,e}$) to account for the efficiencies of the AC generator and working fluid pump motor (η_{gen} and $\eta_{mot,pump}$ respectively).

$$\dot{W}_{exp,e} = \dot{W}_{exp} \cdot \eta_{gen} \tag{7}$$

$$\dot{W}_{pump,wf,e} = \dot{W}_{pump,wf} / \eta_{mot,pump} \tag{8}$$

The system metrics from the thermodynamic analysis are limited to cycle efficiency and second law efficiency. Cycle efficiency is defined as a ratio of the net electrical work produced to the total heat input, shown in equation (9).

$$\eta_{cycle} = \frac{\dot{W}_{net,e}}{\dot{Q}_{evap}} = \frac{\dot{W}_{exp,e} - \dot{W}_{pump,wf,e}}{\dot{Q}_{evap}} \tag{9}$$

The second law efficiency is defined as a ratio between the cycle efficiency and the Carnot efficiency in equation (10).

$$\eta_{cycle,II} = \frac{\eta_{cycle}}{\eta_{Carnot}} \tag{10}$$

Where the Carnot efficiency is calculated in equation (11), with temperatures in Kelvin.

$$\eta_{carnot} = 1 - \frac{T_1}{T_5} \tag{11}$$

3.1.4 Thermodynamic simulation

Utilizing the equations described in this chapter a thermodynamic simulation was performed at an informed operating design point, to provide a benchmark to compare with experimental results. Parameters for the simulation are presented in Table 3.3.

Table 3.3 – Parameters used for theoretical thermodynamic analysis of ORC system.

Parameter	Symbol	Value	Justification
Expander efficiency	$\eta_{s,exp}$	60 %	Typical of the scroll expander in experimental setup (Bamorovat Abadi et al., 2015)
Pump efficiency	$\eta_{s,pump}$	60 %	Conservative estimate for positive displacement pump (Muhammad et al., 2015)
Pump motor efficiency	$\eta_{mot,pump}$	82 %	Nameplate efficiency for pump motor
Generator efficiency	η_{gen}	85 %	Typical of small AC generators (U.S. Department of Energy, 2008)
Condensing temperature	T_8	25 °C	Conservative estimate of lowest achievable temperature (Christchurch, New Zealand)
Evaporator pressure	P_2	1250 kPa	Recommended expander inlet pressure from manufacturer (Air Squared Manufacturing Inc., 2015)
Superheating and subcooling	T_{sup} , T_{sub}	5 °C	Consistent with literature using similar working fluid (Declaye et al., 2013)
Working fluid mass flow rate	$\dot{m}_r$	0.055 kg/s	Maximum flow rate achieved in previous system testing (Southon, 2014)

The results of the design point simulation are presented in Table 3.4. The resulting of net electrical work of 1.34 kW and cycle efficiency of 8 % are comparable to a similar scale simulation by the authors in (Muhammad et al., 2015). This provides an estimate of the order of magnitude of expected experimental performance.

Table 3.4 – Results of the design point thermodynamic analysis.

Performance Parameter	Symbol	Value
Pump electrical work	$\dot{W}_{pump,wf,e}$	0.108 kW
Expander electrical work	$\dot{W}_{exp,e}$	1.44 kW
Net electrical work	$\dot{W}_{net,e}$	1.34 kW
Heat in	$\dot{Q}_{evap}$	16.7 kW
Heat out	$\dot{Q}_{cond}$	15.1 kW
Cycle efficiency	η_{cycle}	8.01 %
Second law efficiency	$\eta_{cycle,II}$	30.7 %

It is noted that the results of this simulation are subject to many assumptions that do not hold true for the experimental system. In an attempt to mitigate this to a degree, conservative estimates for pump and expander efficiencies are chosen, which incorporate losses such as internal leakage pathways and mechanical losses. Future work could involve a more developed cycle model, with in-depth semi-empirical component models, such as those described by the author in (Quoilin, 2007). However, for the purpose of this study, a theoretical estimate is sufficient.

Chapter 4 Experimental Materials and Method

This chapter describes the experimental study performed on the one kilowatt ORC test system. The test rig was the third iteration of the research project, with majority of the system componentry and working fluid inherited in various states of functionality.

Sections 4.1 and 4.2 outline the system componentry and measurement instrumentation respectively. Section 4.3 presents the measurement uncertainty analysis, while section 4.4 covers the specifics of the experimental trials. Section 4.5 details the data collection and post processing methods.

4.1 System Specification

This section presents the specific cycle configuration, summary of the operating parameters, and the specifics of selected components.

4.1.1 Cycle Configuration

Figure 4.1 to Figure 4.3 present the thermodynamic system schematic, experimental system schematic, and the physical lab experimental setup respectively. Components are summarised in Table 4.1, with the components being covered in more detail in the subsequent sections 4.1.x.

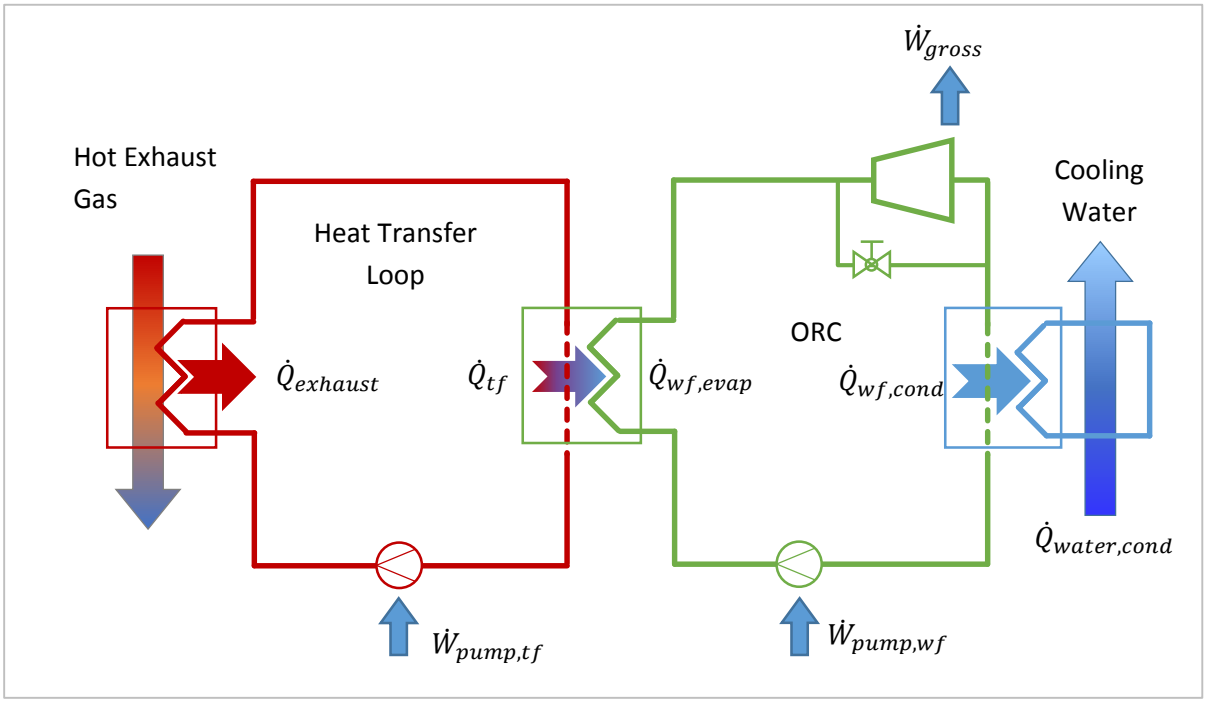

Figure 4.1 – Cycle thermodynamic schematic of the experimental ORC system used by the current study.

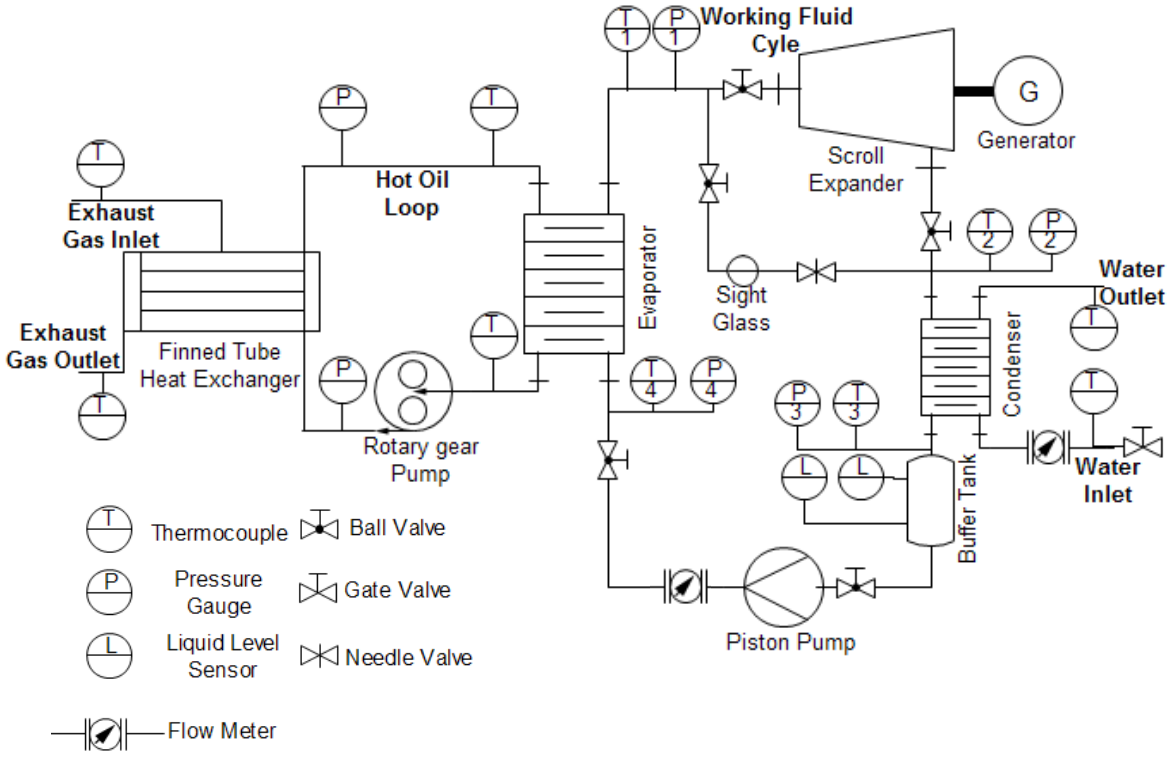

Figure 4.2 – ORC Cycle configuration schematic. Image produced by Leighton Taylor of the University of Canterbury ORC group.

Figure 4.3 – Experimental ORC setup, prior to insulation of all hot components for clarity.

Table 4.1 - Cycle component summary

Component	Type
Evaporator	Brazed 316 SS 60 plate. 26 kW heat capacity. 6.374 m^2 total surface area
Condenser	Brazed 316 SS 40 plate. 30 kW heat capacity 1.805 m^2 total surface area
Thermal oil pump	Gear type pump. 11 cc/rev
Thermal oil pump motor	1.5 HP (1.1 kW). 1 winding
Working fluid pump	3 cylinder piston pump. 4.81 cc/rev
Working fluid pump motor	0.5 HP (373 W). 4 poles
Expander	Scroll type 12 cc/rev. Fixed volume ratio = 3.5
Generator	AC asynchronous with voltage regulation. 2.4 kW, 240V operation at 50 Hz
Working fluid	M1 refrigerant. 50.3 wt% R245fa, 49.7 wt% R365mfc
Heat transfer fluid	High temperature, low viscosity HTF oil
Data Acquisition (DAQ) Unit	National Instruments CompactDAQ

4.1.2 Heat Source

The ORC system acts as a bottoming cycle for a 30 kW Capstone micro turbine, capturing the exhaust waste heat. This exhaust heat ranges in temperature from 200 - 280°C, corresponding to roughly 20 - 80 kWth, based on manufacturer data (Figure 4.4) (Capstone, 2006),(Engel, 2013).

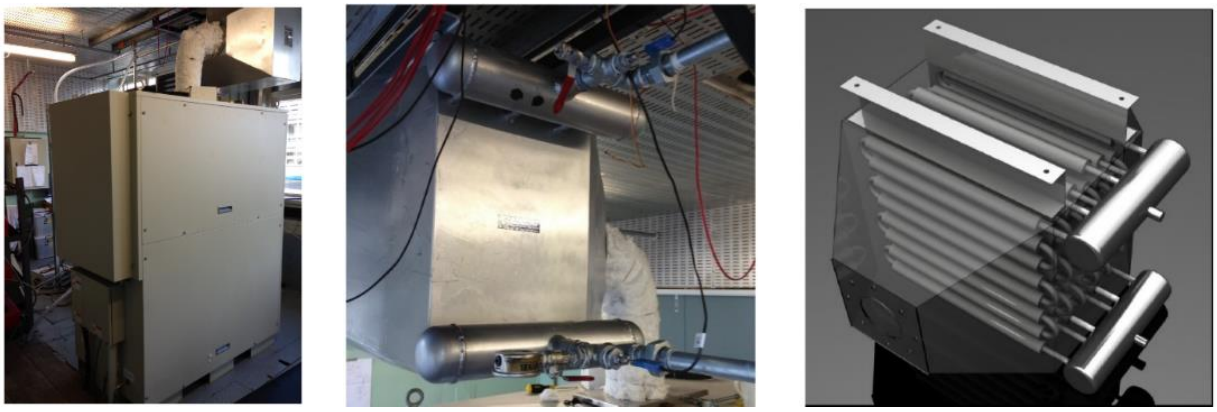

Figure 4.4 - (Left to right) Capstone 30kW micro turbine heat source. Custom finned tube heat exchanger as installed, and CAD model (Engel, 2013).

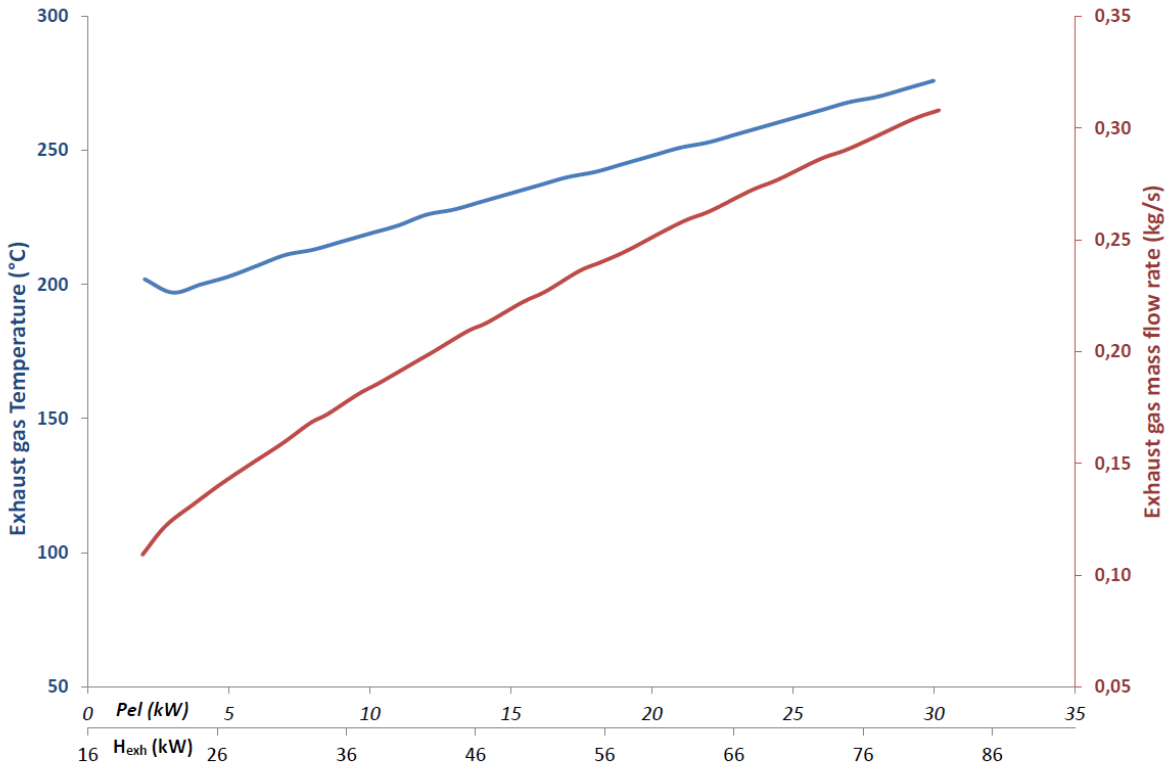

Figure 4.5 - Exhaust heat flow characterization based on manufacturer data (Engel, 2013)

An oil transfer loop is used as an intermediary to bring heat to the ORC system, as direct exposure to these temperatures would cause thermal degradation of the intended working fluid. This system was designed in previous iterations of the project (Engel, 2013),(Meyer et al., 2013). It features a custom manufactured highly finned tube heat exchanger for the gas flow, pressure sensors, an expansion bladder to accommodate for thermal expansion, and a safety valve set to 5 bar. The heat exchanger fins are aluminium making them susceptible to corrosion by sulphuric acid if it is allowed to form.

The thermal oil used is PURITY™ FG Heat Transfer Fluid from Petro-Canada. Manufacturer data on the density (ρ_{tf}), heat capacity ($c_{p,tf}$) and kinematic viscocity (v_{tf}) (see Appendix B) were used for heat rate calculations (equations (12), (13) and (14)). The heat capacity is assumed to be only dependent on oil temperature, T_{tf} , measured in °C.

$$\rho_{tf} = -0.0006 \cdot T_{tf} + 0.8775 \; (kg/L) \tag{12}$$

$$c_{p,tf} = 3.46 \cdot T_{tf} + 1807.86 \; (J/kg) \tag{13}$$

$$v_{tf} = 43342 \cdot T_{tf}^{-1.931} \; (cSt) \tag{14}$$

The oil is circulated by gear pump (Bosch-Rexroth Model F) with a displacement of 11 cc/rev, powered by a 1.1 kW motor, allowing oil flow rate to be estimated as a function of rotational speed (section 4.2.5). The speed of the motor is controlled by a variable frequency drive. The working seals in the pump impose a maximum operating temperature of 100°C on oil leaving the evaporator.

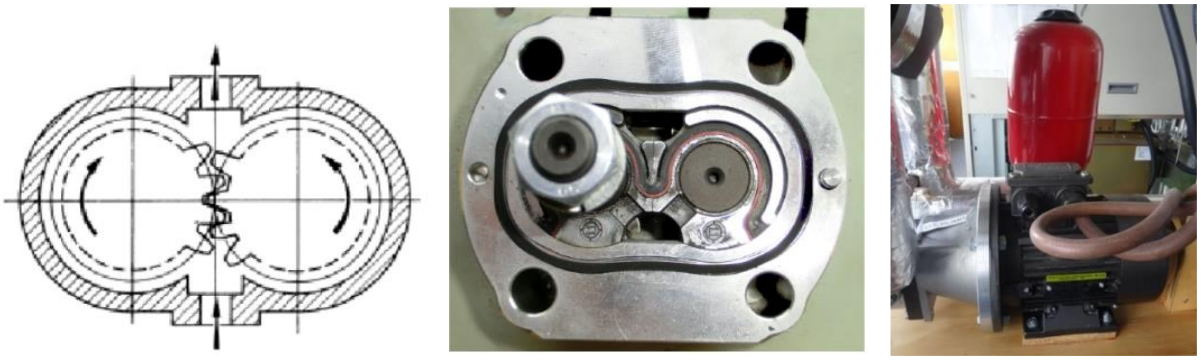

Figure 4.6 – (Left to right) Gear pump working principle (Feldhusen, 2007). Gear pump used in system. Installed pump with oil expansion bladder in background (Engel, 2013)

4.1.3 Working Fluid

The working fluid in the ORC is refrigerant HFC-M1. This is a zeotropic mixture of the two refrigerants R245fa and R365mfc (50.3/49.7 % on a weight percent basis respectively, Appendix C), and is used commercially as a blowing agent for foam insulation. HFC-M1 is a dry working fluid, with thermal decomposition beginning at 200°C.

The properties of the constituent refrigerants are presented in Table 4.2, this data is taken from manufacturer specifications (Honeywell, 2012) and (Solvay, 2010).

Table 4.2 – Properties of pure R245fa and R365mfc

	R245fa	**R365mfc**
Molecular Weight	134.05	148.08
Boiling Point (°C)	15.3	40.2
Global Warming Potential	950	890
Ozone Depletion Potential	0	0
Flammability limits [% by volume]	None	3.5 – 13.3
Thermal stability, continuous operation	200 °C	190 °C

In (Jung et al., 2015), Engineering Equation Solver and REFPROP 9.0 were used to describe the mixture temperature behaviour, displayed in Figure 4.7. Figure 4.7 (a) illustrates the bubble and dew point lines of the mixture over the entire composition range. At 1405 kPa the chosen composition

has a temperature glide (section 2.4.2.1) of 4.5 °C out of a possible maximum of 4.9 °C. Figure 4.7 (b) shows the T-S curves for the constituent refrigerants and resulting mixture.

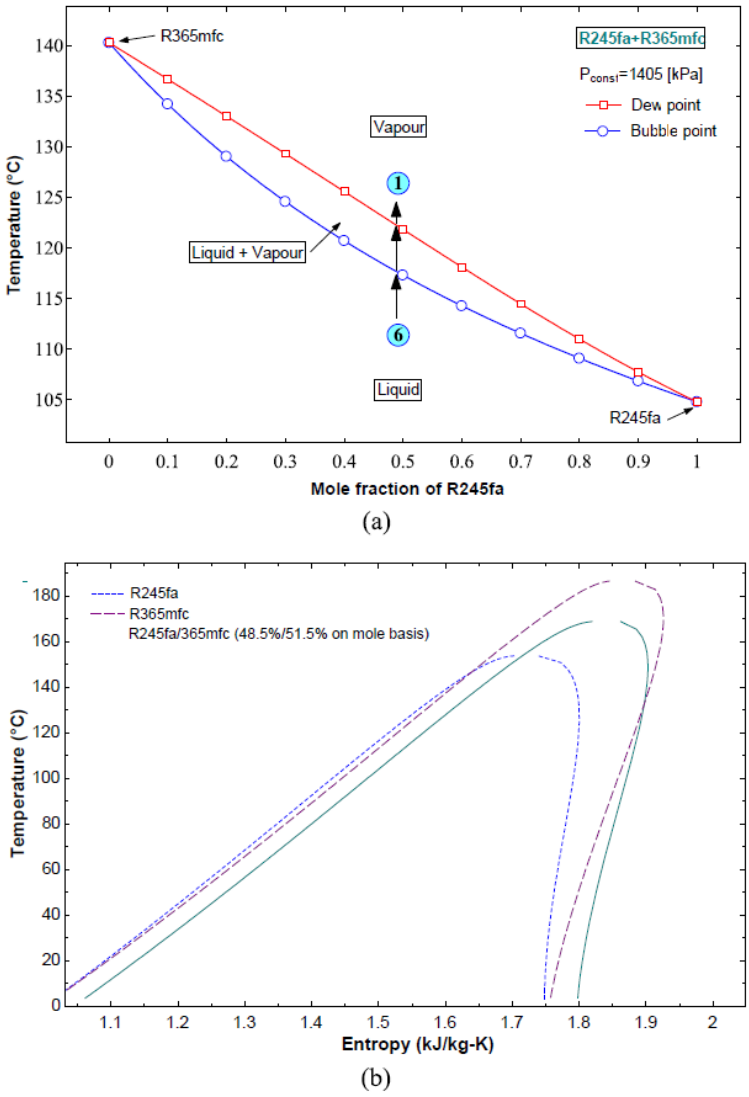

Figure 4.7 – (a) Bubble and dew point lines of the M1 working fluid illustrating the temperature glide at operating pressure. (b) Temperature-Entropy diagrams of the pure fluids and mixture. Generated in previous work on system by (Jung et al., 2015)

The material compatibility of M1 is not documented directly. Of primary concern is the interaction with seals in the fluid pump, ball valves and scroll expander. Both R245fa and R356mfc quote slight weight increases for nitrile rubber (4.2% and 2.5% respectively). R245fa has negligible interaction with Polytetrafluoroethylene (PTFE) at atmospheric temperatures and pressures (Honeywell, 2012), however, no data is presented for R365mfc (Solvay, 2010) . The possible effects of unknown material compatibility are explored in section 5.4.

4.1.4 Working Fluid Pump

The working fluid pump is a piston-type positive displacement pump from CAT pumps (model 2SF22ELS), with a volumetric displacement of 4.81 cc/rev. The pump is powered by a 373 W 4 pole motor, controlled via a variable frequency drive (Figure 4.8).

This pump was chosen since the fixed displacement per rotation theoretically allows calculation of the fluid flow rate as a function of rotational speed, although this was found to be inaccaurate (section 5.2.6.2). Furthermore, this pump is able to achieve high pressures at low flow rates, and isolates working fluid stream from rotating componentry and lubrication contamination.

The original ORC pump seals were Nitrile-butyl rubber (NBR). Honeywell does not recommend using NBR in dynamic situations with R245fa as the working fluid. In a previous study a PTFE replacement seal kit was purchased and installed (Southon, 2014). During subsequent operation these seals were destroyed, which was attributed to possible chemical corrosion or operation of the pump in the absence of the working fluid. At the beginning of the current study the seals were replaced with an original NBR kit, with the understanding they may swell and impair performance but be less likely to disintegrate entirely.

Figure 4.8 – Feed pump (left) and controller (right)

4.1.5 Expander

The expander is a commercially available 1 kW, oil free, scroll expander designed by AirSquared (model E15H22N4.25, part # E15H022A-A03), shown the left in Figure 4.9. It features a semi-hermetic design, with no dynamic seals and uses a magnetic coupling to power a generator (Voltmaster AB30) incorporated into the unit. The intended working fluid is R245fa, it features oil-free operation, and at the maximum inlet pressure of 13.8 bar is quoted to achieve 70% isentropic efficiency at 3000 – 3500 RPM (Table 4.3).

Table 4.3 - Scroll expander manufacturer specifications (Air Squared Manufacturing Inc., 2015)

Specification	**Symbol**	**Value**
Nominal output		1 kW
Maximum inlet pressure		13.8 bar
Swept volume	V_{swept}	12 cc/rev

Specification	Symbol	Value
Volume ratio		3.5
Maximum Speed		3,600 RPM
Maximum Isentropic efficiency		70% at 13.8 bar inlet, 5.5 bar exhaust, 3000 – 3500 RPM

Load is imposed on the generator and dissipated via a bank of light bulbs, acting as resistors, which can be switched manually in a binary fashion, shown on the right in Figure 4.9. The bulbs used were 100W, 200W, and two 500W units.

Figure 4.9 - Left: Scroll expander and coupled generator. Right: Light bulb resistor bank.

4.1.6 Evaporator, Condenser

The evaporator and condenser are single pass, counter current flow, 316 SS brazed plate heat exchangers manufactured by Kaori. The evaporator (model K205) has 60 plates (6.734 m^2 total) and a heat capacity of 26 kW. The condenser (model K095) is a 40 plate (1.805 m^2) unit with a heat capacity of 30 kW. The municipal water supply is passed through the condenser as the heat sink, with the flow rate controlled by a globe valve.

4.1.7 Buffer tank

A custom manufactured 1.8 L buffer tank is located before the pump to allow the system to behave dynamically during start-up, and testing different operating conditions. The tank also ensures that there is always liquid being provided to the pump as operating in vapour would damage the seals.

4.1.8 Valve layout

4.1.8.1 Expander isolation

Two high pressure, low restriction ball valves (SS-AFSS8 from Swagelok) on the inlet and outlet of the expander allow the expander to be completely isolated from the working fluid loop.

4.1.8.2 Bypass line

A ball valve allows diversion of fluid flow through the bypass loop. A needle valve placed in this loop is used to restrict flow and incur a pressure drop during the system start up, simulating an expander.

In conjunction with isolating the expander, the bypass line is used during start-up and shut down of the system, when the working fluid is not at a superheated state which would cause damage to the expander.

4.1.8.3 Pressure Relief Valve

The pressure relief valve is located between the pump and the evaporator as a safety measure, preventing catastrophic failure. The valve is set to 20 bar - six bar above the maximum operating pressure of the system (14 bar), and below the burst pressure of the system components.

4.1.9 Estimated system volume

For DVR calculations, the internal system volume of the working fluid loop is estimated to be 0.01124 m^3. The estimated volumes for the various components obtained from manufacturer specifications are summarised in Table 4.4.

Table 4.4 – Estimated internal system volume

Component	Volume (m^3)
Evaporator	0.00679
Condenser	0.00200
Expander	0.000012
Fluid pump	0.0000048
Buffer tank	0.00165
Piping	0.00079
Total	**0.01124**

4.2 Measurement/instrumentation

This section outlines the specifics of the measurement instrumentation and principles used in data collection for the ORC system.

4.2.1 Thermocouples

K-type sheathed thermocouples from Intec Instruments LTD are used for the majority of temperature measurements, as they are inexpensive yet accurate over a wide range of temperatures (Table 4.5). The thermocouples are not individually calibrated, and this study uses the manufacturer response curve in the data acquisition program.

Table 4.5 – Thermocouple Specifications for Intech MTC-I3.0K310-300-MP

Parameter	Value
Temperature Range	-100 to 1150°C
Accuracy	±0.40% of reading above 0°C
Response time	1 s
Output	1 – 10 V

4.2.2 Pressure Transducers

Pressure measurements are taken by piezoelectric transducers from the PX309 model range by Omega. All are fitted with pressure snubbers to protect the sensors from large pressure spikes and to dampen small amplitude oscillations in pressure for a more accurate reading. All output between 0-5 V over their measurement range, and quote a 0.25% accuracy for the full range.

Sensors are appropriately sized to the pressures experienced at their location, resulting in a total of five different models. At the outset of the current study, inspection revealed incorrect sensor calibration. This required a total overhaul of the sensor integration and calibration in the data acquisition program before trials could begin.

Additionally, the oil loop initially featured a bourdon gauge for pressure measurement located near the rear heat exchanger which was out of sight for the operator. After an oil spill occurred when the pressure limit of the safety valve was exceeded in preliminary trials, a piezoelectric sensor was installed and integrated to allow oil pressure monitoring and warning from the main console.

4.2.3 Optical Level Sensors

Two LVE 115/116 series electro-optic sensors from Omega indicate fluid level in the buffer tank. These provide the only digital feedback observing the fluid flow in the system. A high and low-level signal are associated with the sensors, providing a warning against flooding the condenser and running the fluid pump dry.

4.2.4 Working Fluid Volume Flow

Figure 4.10 – H250 M40 variable area flow meter

The working fluid flow is measured by an analogue H250 M40 variable area flow meter from KROHNE, shown in Figure 4.10, installed between the working fluid pump and the evaporator. At this location, the liquid fluid properties are relatively consistent and informed from previous tests. Manufacturer data states the accuracy to be ± 1.6% of the measured value at over 50% of the measurement scale, with accuracy decreasing below this to ± 8% of the measured value at the bottom 10% of the measurement scale.

The sensor was specified and installed during the second iteration of the system, but only used once. The current study found the sensor to be poorly suited to the intended flow range. This is discussed in section 6.1.7.

It is noted this flow meter was not experimentally calibrated prior to installation and use, since the manufacturer claims calibration at the time of fabrication.

4.2.5 Thermal Oil Volume Flow

The thermal oil volumetric flow rate ($\dot{V}_{tf}$) was calculated using an empirical relationship established by (Engel, 2013) from data in Figure 4.11, correlating flow rate with the motor pump controller speed, (equation (15)).

$$\dot{V}_{tf} = (0.0103 \cdot \mathrm{n} + 0.20) \pm (0.0008 \cdot \mathrm{n} - 0.20)\ \frac{\mathrm{L}}{\mathrm{min}} \tag{15}$$

Here n is the pump motor controller speed in RPM. Engel found the pump flow rates were consistently between the theoretical maximum at that speed and the pump specified flow at the operating conditions – therefore these are considered as the boundaries of the uncertainty range. Based on the provided data, this equates to a ± 2.5 % relative uncertainty.

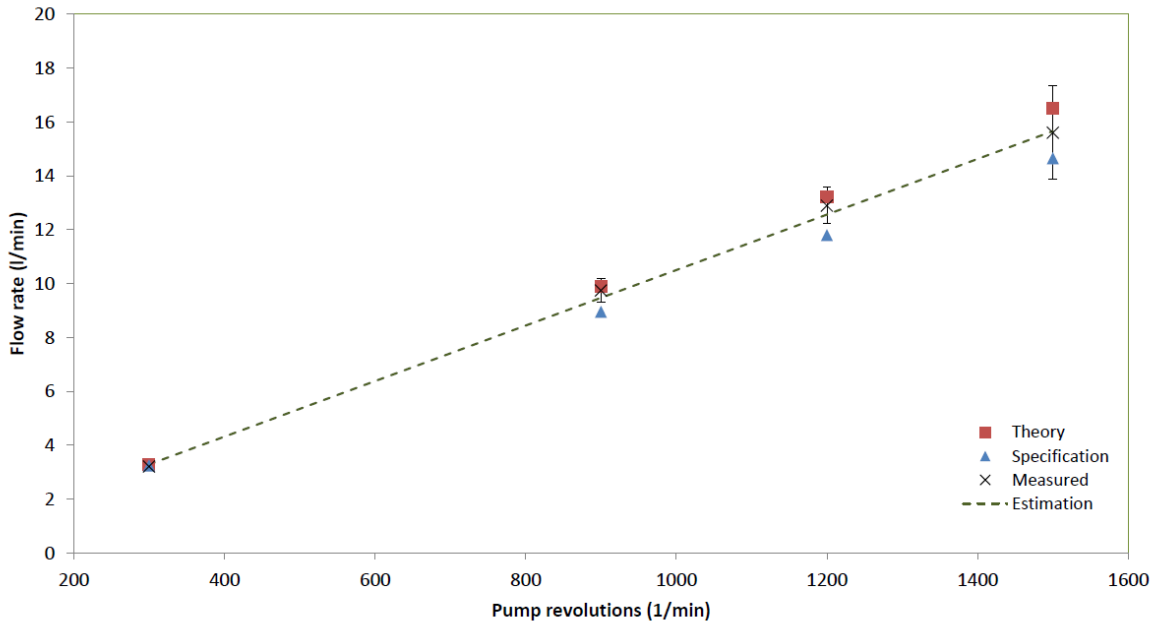

Figure 4.11 – Experimental data from which the pump flow relationship was derived (Engel, 2013)

4.2.6 Capstone Exhaust Mass Flow

The Capstone exhaust mass flow rate ($\dot{m}_{exhaust}$) is estimated from manufacturer data for the operational range of power settings of 5 – 30 kW, shown in Figure 4.12. The resulting linear fit adequately describes the data with an R^2 value of 0.998, and is shown in equation (16):

$$\dot{m}_{exhaust} = 0.0066\, P_{Capstone} + 0.1139\ (\frac{kg}{s}) \tag{16}$$

Where $P_{Capstone}$ is the set electrical power in kW.

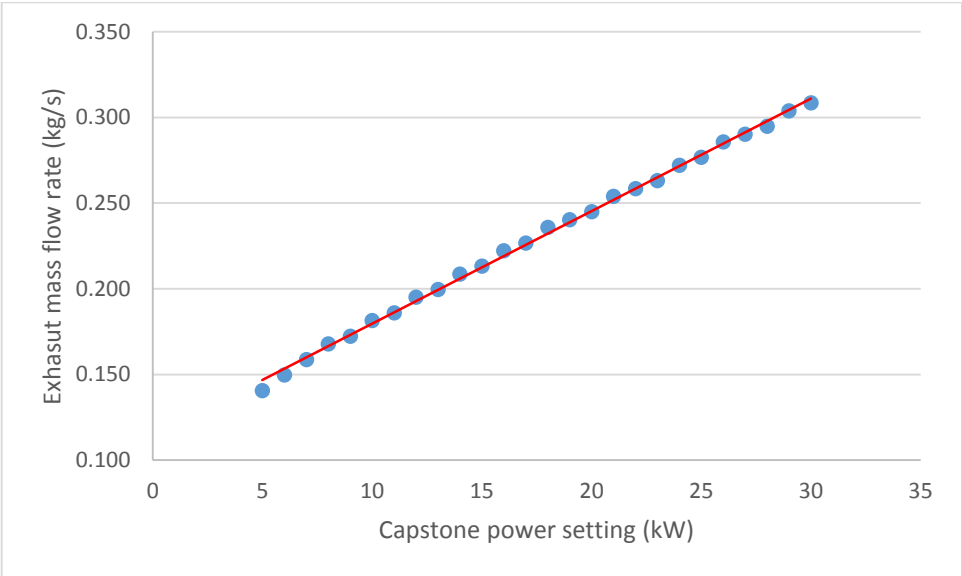

Figure 4.12 – Capstone exhaust mass flow rate as a function of the power setting from manufacturer data (Capstone, 2006).

4.2.7 Condenser Fluid Volume Flow

The water passing through the condenser is measured by a Sensus 120C rotary piston flow meter which generates a pulse for every litre of throughput, integrated into the data acquisition program. Manufacturer accuracy is quoted at ± 2% at the operational flow rates.

4.2.8 Shaft Power

The expander shaft power is not measured directly, rather it is inferred by measuring the generated electrical power. This is measured with a Fluke 2050 clamp meter, with a stated uncertainty of ± 2.5 % for power measurement. An optical tachometer on the generator shaft monitors rotational speed, accurate to ± 60 RPM. For ease of uncertainty calculations, this is generalised to a conservative relative error of ± 3.5 %, based on the minimum rotational speed of 1700 RPM.

It is noted this method neglects to account for electrical and mechanical losses, which have to be estimated for shaft work and torque to be calculated. The limitations of this method are discussed in section 5.1.7.

4.2.9 Pump Power Consumptions

4.2.9.1 Working fluid pump

The working fluid pump does not have a dedicated sensor for power measurement. In similar published studies where this is the case (e.g. (Bamorovat Abadi et al., 2015)), power consumption is estimated by thermodynamic analysis of the pump, and assuming an electrical efficiency for the pump motor. This study attempts to implement a more direct measurement, by establishing a relationship from a selection of experimental results, detailed in section 5.1.1.

4.2.9.2 Transfer oil pump

Similarly to the working fluid pump, the oil pump does not have a dedicated sensor for power measurement. An empirical relationship is established from a selection of results in section 5.1.2.

4.3 Measurement uncertainty analysis

A rudimentary uncertainty analysis was conducted to estimate the uncertainty of the calculated quantities in the study. The uncertainty of the measured parameters, based on manufacturer specifications of the measurement equipment, is shown in Table 4.6.

Table 4.6 – Measurement uncertainty from manufacturer specifications.

Parameter	Symbol	Relative uncertainty ε (%)
Temperature	T	0.40
Pressure	P	0.25
Working fluid volumetric flow rate*	$\dot{V}_{wf}$	8
Generator electrical power	$\dot{W}_{gross}$	2.5
Shaft rotational speed	N_{rot}	3.5
Transfer fluid volumetric flow rate	$\dot{V}_{tf}$	2.5

* *The maximum relative uncertainty reported by the manufacturer is chosen as a conservative estimate.*

In order to estimate uncertainties of calculated parameters, several unknown uncertainty quantities were given a conservative assumption, shown in Table 4.7. Exhaust and transfer fluid mass flow rates were calculated from manufacturer data where no uncertainty is provided, and the two pump powers were calculated using an empirical relationship from experimental data. Where REFPROP was used to calculate a fluid property, the approach of the authors in (Bracco et al., 2013) was followed, assuming an uncertainty (ε_{RP}) from the equations in (Lemmon and Span, 2006).

Table 4.7 – Unknown uncertainties and their assumed values.

Parameter	Symbol	Assumed relative uncertainty ε (%)
Capstone exhaust mass flow rate	$\dot{m}_{exhaust}$	5
Transfer fluid mass flow rate	$\dot{m}_{tf}$	2.5
Working fluid pump power	$\dot{W}_{pump,wf}$	5
Transfer fluid pump power	$\dot{W}_{pump,tf}$	5
REFPROP equations	ε_{RP}	2

Table 4.8 shows the estimated relative uncertainties for the main parameters considered in this study, evaluated by applying error propagation formula to the equations used in calculations.

Table 4.8 – Uncertainties of calculated parameters from experimental tests.

Calculated Parameter	Symbol	Uncertainty calculation	Estimated relative uncertainty ε (%)
Fluid property (Specific enthalpy, specific volume, density, heat capacity)	ε_{fp}	$\sqrt{(\varepsilon T)^2 + (\varepsilon P)^2 + (\varepsilon_{RP})^2}$	2.1
Working fluid mass flow rate	$\dot{m}_r$	$\sqrt{\left(\varepsilon \dot{V}_{wf}\right)^2 + \left(\varepsilon_{fp}\right)^2}$	8.3
Expander isentropic efficiency	$\eta_{s,exp}$	$\sqrt{\left(\varepsilon \dot{W}_{gross}\right)^2 + (\varepsilon \dot{m}_r)^2 + \left(\varepsilon_{fp}\right)^2}$	8.9
Expander filling factor	ϕ	$\sqrt{(\varepsilon N_{rot})^2 + (\varepsilon \dot{m}_r)^2 + \left(\varepsilon_{fp}\right)^2}$	9.2
Working fluid heat transfer	$\dot{Q}$	$\sqrt{(\varepsilon m_r)^2 + (\varepsilon T)^2 + \left(\varepsilon_{fp}\right)^2}$	6.8
Net cycle power	$\dot{W}_{net}$	$\sqrt{\left(\varepsilon \dot{W}_{gross}\right)^2 + \left(\varepsilon \dot{W}_{pump,wf}\right)^2}$	5.6
Cycle efficiency	η_{cycle}	$\sqrt{\left(\varepsilon \dot{W}_{gross}\right)^2 + \left(\varepsilon \dot{W}_{pump,wf}\right)^2 + (\varepsilon \dot{m}_r)^2 + \left(\varepsilon_{fp}\right)}$	10.2

The cycle efficiency uncertainty of 10.2 % is of similar magnitude to the 13 % calculated by the authors in (Bracco et al., 2013), who used similar equipment. Overall, the current study's uncertainties are generally 5 - 6% higher than other similar works such as (Bamorovat Abadi et al., 2015) and (Wang et al., 2010), due to the large uncertainty associated with the working fluid volume flow measurement. Additionally, it is worth noting these measurement uncertainties may be overshadowed by the time dependent operational errors encountered during testing. These include loss of working fluid through leakage, fouling of the working fluid, and degradation of the bearings in the expander, as described in section 5.4.

4.4 Experimental Method

The following sections outline the rationale and methodology of the experimental tests conducted in this study. Two sets of tests were completed, with a system failure separating the methods and intended results.

4.4.1 Fluid charging procedure

Prior to charging the system with working fluid, the following procedure was followed, which aims to ensure the integrity of the system and remove all non-condensable gasses.

- The system was pressurised to 10 bar with nitrogen, and a soap mix was used as a bubble agent to test joints for leaks. The system valves were closed, and the system was left at pressure for three hours to confirm the absence of leaks.
- With no leaks detected, system was evacuated with a vacuum pump, which was maintained for 24 hours.
- Prior to charging with fluid, the cycle of pressurising/evacuating was repeated.

4.4.2 Steady State Definition

For this study, all analysis was performed using steady state operating points. During operation, pressures and temperatures at the exit of the evaporator and expander were manually monitored. Therefore, for simplicity in the experiments, steady state was declared when the pressure and temperature variations were within 2 % and 2 K respectively, over a 10-minute period. A more stringent definition of steady state was applied to the data in post processing, elaborated on in section 4.5.

4.4.3 Test 1: System Performance Mapping

In its previous iterations, the system had never been fully tested. Therefore, the first step in the experimental study was to systematically investigate the system over its operational range. The aim of these trials was threefold:

1. Establish the upper and lower boundaries of system steady state operation within the limits outlined in Table 4.9.
2. Establish the degree of impact the controllable inputs had on performance. Of particular interest was the relative effect of thermal oil flow rate and Capstone power setting on available heat in the evaporator.
3. Collect a detailed data set for the highest DVR to be tested, for analysis of system performance metrics.

The results from this experiment would inform a selection of operating inputs to progressively test the effect of decreasing the DVR in the system. The inputs would balance a good resolution of the performance metrics under consideration, within a reasonable total testing time.

4.4.3.1 Test methodology

In order to limit the permutations of trials for this experiment, the following variable constraints were imposed:

- Condenser flow rate maintained at a constant value of 1.0 ± 0.1 L/s, corresponding with the valve in the fully open position.
- Ambient temperature kept as constant as possible around 18°C.
- Constant working fluid charge of 9.26 ± 0.2 kg, equating to a DVR of 0.64.

The following process was implemented to gather test results using the input variable range listed in Table 4.10:

1. Set Capstone power level.
2. Set transfer oil motor speed.
3. Test five working fluid motor speeds, from 12 Hz/as low as possible within constraints of system, up to 27.5 Hz/as high as possible within constraints.
4. At each of the working fluid motor speeds, set generator load to 500W and 1000W respectively.

Table 4.9 – System operating condition limitations

Parameter	Limitation
Thermal oil exit temperature	100 ^{O}C
Working fluid temperature	140 ^{O}C
ORC loop pressure	13.5 bar
Feed pump speed	27.5 Hz
Buffer tank	Above low-level sensor

Table 4.10 – Experimental system evaluation, summary of inputs

Component	Setting
Capstone Turbine (heat source)	5-25 kW in 5 kW steps
Thermal Oil Pump	6, 12, 18 Hz
Working fluid pump	12 – 27.5 Hz (Flow rate 0.02 to 0.06 kg/s)
Cooling water flow	Inlet valve fully open, flow rate between 0.9 and 1.1 kg/s
Generator resistance	500 W and 1000 W
Ambient Temp.	17-20 ^{o}C

The results of these tests are discussed in section 5.1, Experimental results of system performance, and section 5.2, Analysis of cycle performance.

4.4.4 Test 2: Adapted Dimensionless Volume Ratio testing

The experiments in section 4.4.3 were prematurely ended due to bearing failure in the scroll expander. With no expander, the aim of the new trials was to observe the effect of the DVR on the range of achievable steady state operating conditions, and any indicators as to its possible effect on performance. To achieve this, the maximum operating pressure ratio and mass flow rate at each DVR was inspected.

Work by (Li et al., 2015) showed their system behaviour changed when reducing DVR from 0.51 to 0.32, therefore a similar range of DVR was adopted for the current study. To check the appropriateness of this range, an estimate of 2/3s full heat exchangers and full condenser-pump and pump-evaporator lines resulted in a DVR of 0.54.

The expander was isolated by closing the ball valves, and the needle valve in the bypass loop was used to impose a pressure drop on the system, as was demonstrated in the studies by (Wang et al., 2010) and (Shu et al., 2016).

The following variable constraints were imposed:

- Oil transfer pump speed maintained at 12 Hz.
- Condenser flow rate maintained at a constant value of 1.0 ± 0.1 L/s, corresponding with the valve in the fully open position.
- Ambient temperature kept as constant as possible around 18°C.

The following procedure was implemented at Capstone settings of 5, 10 and 15 kW for each of the DVRs listed in Table 4.11:

1. Create a pressure differential using the needle valve.
2. Increase fluid pump speed incrementally until the maximum steady state was achieved while maintaining liquid level above the "low" sensor in the buffer tank to prevent damage to pump.
3. Increase the pressure ratio further with the needle valve and repeat this process until the limitations of the ORC are met (Table 4.9).

Table 4.11 – Experimental DVR achieved

DVR	Corresponding working fluid mass (kg ±0.02)
0.534	7.94
0.471	6.99
0.409	6.08
0.352	5.24
0.289	4.30

The results of these tests are discussed in section 5.3.

4.5 Data Processing and Analysis Methodology

This section outlines the data acquisition methods and post processing for result collection and analysis.

4.5.1 Data Acquisition

Sensor data is acquired through a National Instruments CompactDAQ in conjunction with a LabVIEW program (Figure 4.13). The program allows monitoring of all digital sensors including fluid and

pressure level warnings, control over the fluid pump speeds, and logging of manual data inputs. All parameters are logged every two seconds to a plain text file, for later handling in post processing.

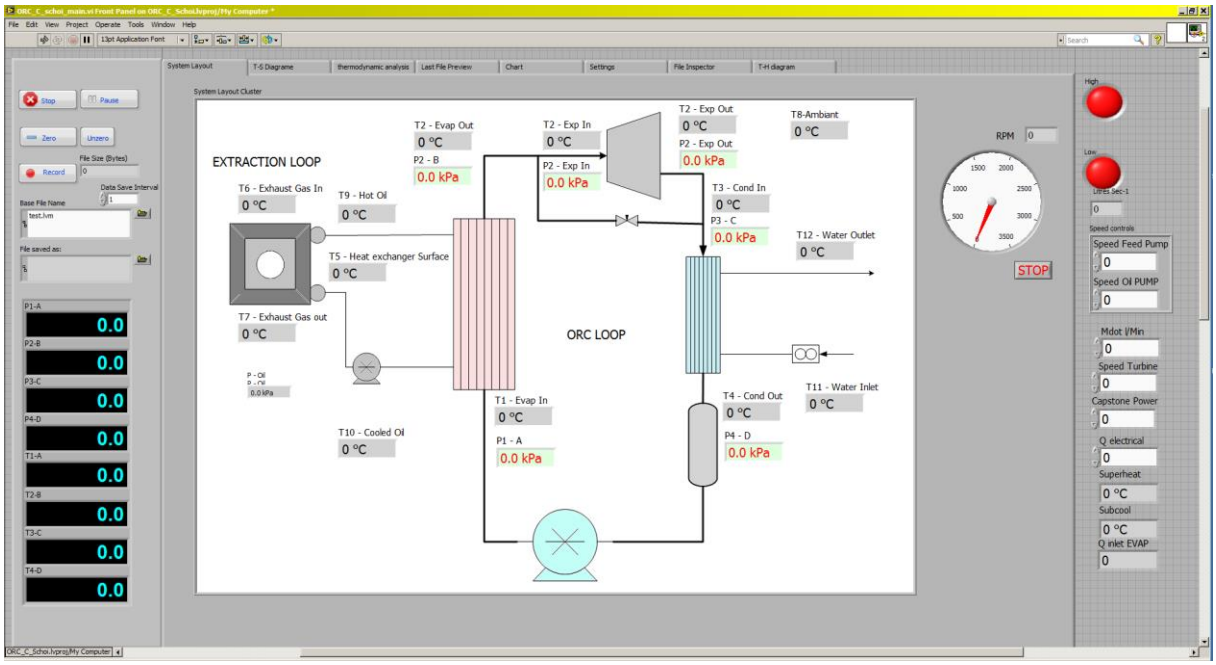

Figure 4.13 – LabVIEW control interface

Simultaneously, power output data from the clamp meter is logged by a proprietary logging program from Fluke. This is also logged every two seconds, and matched to the LabVIEW output by its initial timestamp in post processing.

4.5.2 Post Processing and Steady State Identification

Post processing of data for steady state identification and subsequent analysis was handled in MATLAB 2016b.

For steady state identification an adaptation of the methods presented by the authors in (Donald L. Simon, 2010) was used. First, custom Butterworth/low pass filters were created for sensor data where the filtering built into the LabVIEW code was deemed ineffective (as the signals retained significant noise which was addressed by MATLAB filters). Then the following procedure was implemented on the resulting data:

1. Data is parsed for changes in the controlled inputs.
2. When a change is detected, an array of points equal to 5 minutes preceding the change is created.
3. For the pressure sensors at the exit of the evaporator and expander (four total), if the coefficient of variance of the array is less than 0.5% then steady state is declared.
4. All data is averaged over the time window, and stored as a steady state operating point.

This identification process resulted in a total of 140 steady state points being identified from the experimental dataset, which are analysed in the following chapter.

Chapter 5 Results and Operational failure analysis

Over the testing period, 140 steady state points were achieved over 80 hours of operation, consuming over 700 litres of diesel and 150 m^3 of water in the process. The expander failed after 60 hours of operation.

5.1 Experimental results of system performance

This section presents results and observations from both sets of experiments. Relationships for calculating the two pump power consumptions are established, and the Capstone exhaust characteristics are inspected. The impact of the oil pump speed on heat transfer rate is analysed, along with the generator behaviour.

5.1.1 Working fluid pump power consumption

There was no dedicated power measurement for the working fluid pump power. A method of estimating working fluid pump power consumption is required for cycle analysis.

During the second set of tests as outlined in section 4.4.4, the fluid pump power was measured with the clamp meter to establish an empirical relationship for calculating the pump power. The power consumption as a function of the input motor controller frequency and pump exit pressure is shown in Figure 5.1.

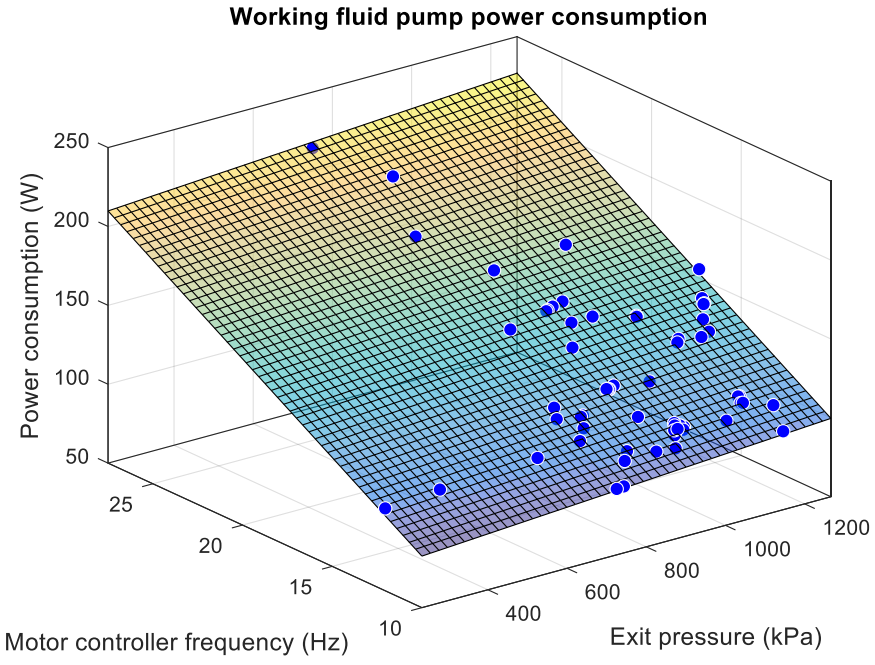

Figure 5.1 –Working fluid pump power consumption as a function of input motor controller frequency and pump exit pressure from experimental results. Linear surface fit for empirical relationship with an R^2value of 0.992.

The data shows good linear agreement with an R^2 value of 0.992, and the 95% confidence bounds of the coefficients do not cross zero. The power consumption has weak pressure dependency, and is

primarily dependent on motor input frequency. The resulting equation used for determining working fluid pump power in further analysis is shown in equation (17).

$$\dot{W}_{pump,wf} = 6.172 + 0.01646 \cdot P_{pump,wf,out} + 7.266 \cdot f_{pump,wf} \quad (17)$$

Where $P_{pump,wf,out}$ is the pressure at the outlet of the pump in kPa, and $f_{pump,wf}$ the input motor controller frequency in Hz.

5.1.2 Transfer fluid pump power consumption

As with the working fluid pump, there was no dedicated power measurement for the transfer fluid pump power consumption. A method of estimating transfer fluid pump power consumption is required for system analysis.

During second set of tests as outlined in section 4.4.4, power measurements at frequencies within the operating range were taken with a clamp meter, shown in Figure 5.2.

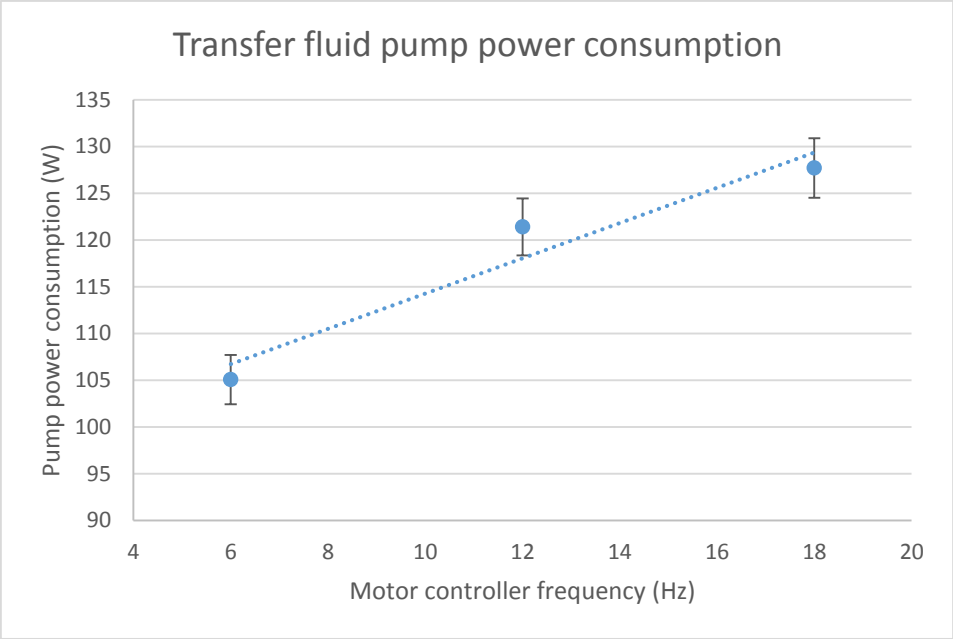

Figure 5.2 – Transfer fluid pump power consumption as a function of motor controller frequency from experimental results. Linear fit for relationship estimation.

The data shows linear agreement, with the power consumption increasing with motor input frequency. While the relationship is of low quality due to its lack of data points, it is sufficient for providing an estimate for transfer fluid pump power (equation (18)).

$$\dot{W}_{pump,tf} = 1.885 \cdot f_{pump,tf} + 95.43 \quad (18)$$

Where $f_{pump,tf}$ is the motor controller frequency in Hz. The relationship assumes pump power consumption is dominated by motor speed, that there is a negligible pressure increase during operation, and neglects the effects of changing temperature on viscosity.

5.1.2.1 Limitation

The measurements of pump power and motor controller speed were taken under conditions such that the temperature of the oil ranged from 85 -87 °C, equating to an approximately constant

kinematic viscosity. However, the resulting relationship is used to estimate power for a set of experiments in which the oil temperature, and therefore viscosity, varies outside of this range.

Consider Figure 5.3, which shows the oil temperature for the experiment in which equation (18) is developed (indicated by red diamond symbols), compared to the range of temperatures it is applied to, shown by the box plots.

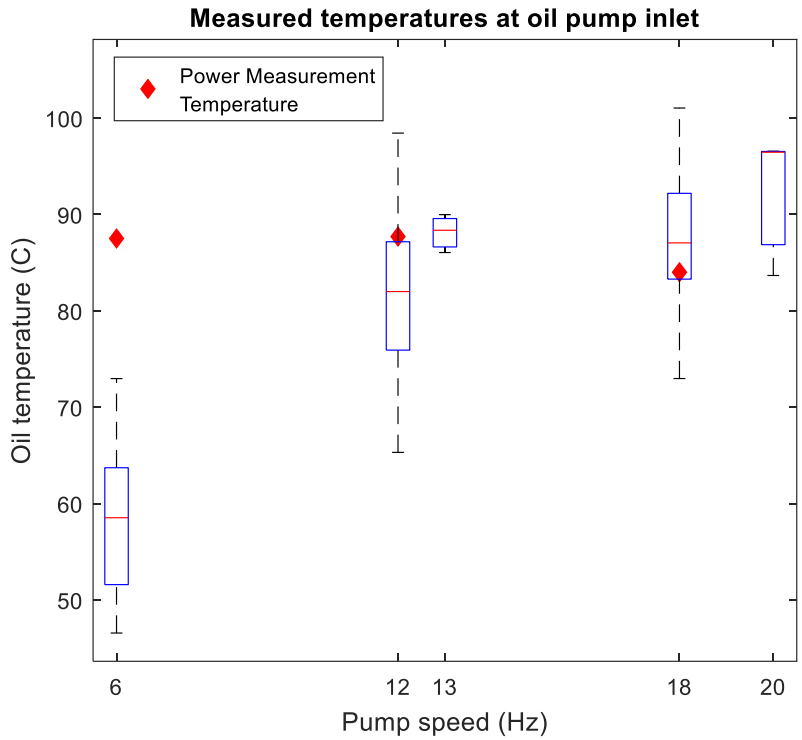

Figure 5.3 – Oil temperature at pump inlet from experimental data used to generate power relationship (red diamond), compared to all temperatures recorded during operation at each pump speed setting.

The results suggest equation (18) may be more appropriate above 12 Hz pump speed, and may be misrepresenting power consumption at 6 Hz. From manufacturer data, the kinematic viscosity at the 6 Hz measurement is approximately 2.2 times smaller than that at the median oil temperature observed at 6 Hz.

Due to these limitations, this estimation introduces a degree of uncertainty when it is used in analysis, nevertheless it yields a reasonable estimate for power consumption. As explored in Chapter 6, to improve the accuracy of power consumption the pump requires a dedicated sensor.

5.1.3 Capstone exhaust temperature

To inspect the stability of the temperature of the exhaust stream, the observed exhaust temperatures at each Capstone power setting are shown in Figure 5.4.

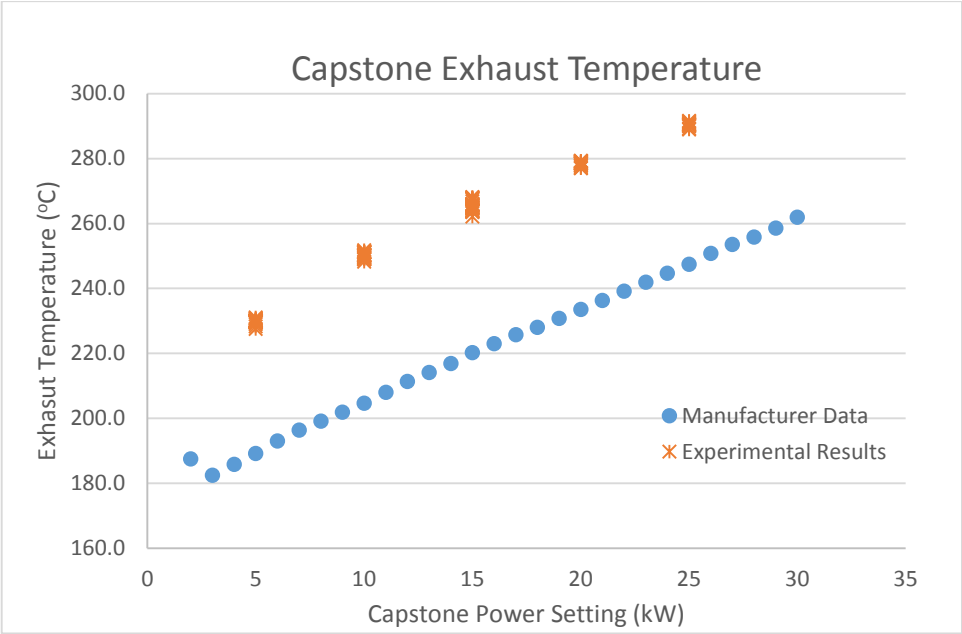

Figure 5.4 – Observed exhaust temperatures of the Capstone turbine at each tested power setting from experimental data for all 140 data points, compared to manufacturer data.

The results indicate that temperatures were relatively consistent at each power setting, varying by approximately 1.5 % at each Capstone setting. This increases confidence that setting an output power on the Capstone turbine results in a steady heat source temperature. However, it is noted the observed temperatures were consistently 44 ± 5 °C higher compared to the manufacturer data.

It is possible but unlikely this discrepancy is due to a calibration error in the thermocouple for the exhaust temperature measurement. The manufacturer temperatures may be a conservative bulk gas temperature, as opposed to the temperature given by the thermocouple, which is position dependent.

The discrepancy between manufacturer data and measured data raises the concern that using manufacturer data to calculate exhaust mass flow rate may be invalid. To eliminate this uncertainty in future testing, it is worth considering estimating exhaust mass flow rate as shown in (Yang et al., 2013), discussed further in Chapter 6. Estimation is a more cost effective approach as direct measurement would require expensive sensory equipment to overcome the obstacles of high temperatures, undeveloped flow conditions, and the lack of a reference mass flow rate for calibration (Engel, 2013).

5.1.4 Capstone exhaust waste heat energy

The available waste heat energy in the Capstone exhaust stream is characterized for each power setting. This allows inspection of the proportion of waste heat recovered by the ORC.

A simplified custom gas mixture was created in REFPROP for calculating the specific heat capacity (c_p) of the exhaust stream. The composition of the exhaust gas on mass basis assumes perfect combustion of diesel fuel, which (Yu et al., 2013) establish as: CO_2 = 15.1 %, H_2O = 5.5 %, N_2 = 71.6 %, O_2 = 7.8 %.

The available waste heat energy is denoted as $\dot{Q}_{exhaust,ideal}$ and calculated in equation (19).

$$\dot{Q}_{exhaust,ideal} = \dot{m}_{exhaust} \cdot (c_{p,exhaust,in} \cdot T_{exhaust,in} - c_{p,exhaust,ideal} \cdot T_{exhaust,ideal}) \quad (19)$$

The value of $T_{exhaust,ideal}$ is chosen such that the exhaust temperature remains above the acid dew point of the diesel fumes at the exhaust pressure, to prevent damage to the aluminium fins of the heat exchanger. This is assumed to be 120°C as used by the authors in (Shu et al., 2016).

The calculated available waste heat at each Capstone power setting for all experimental trials is shown in Figure 5.5.

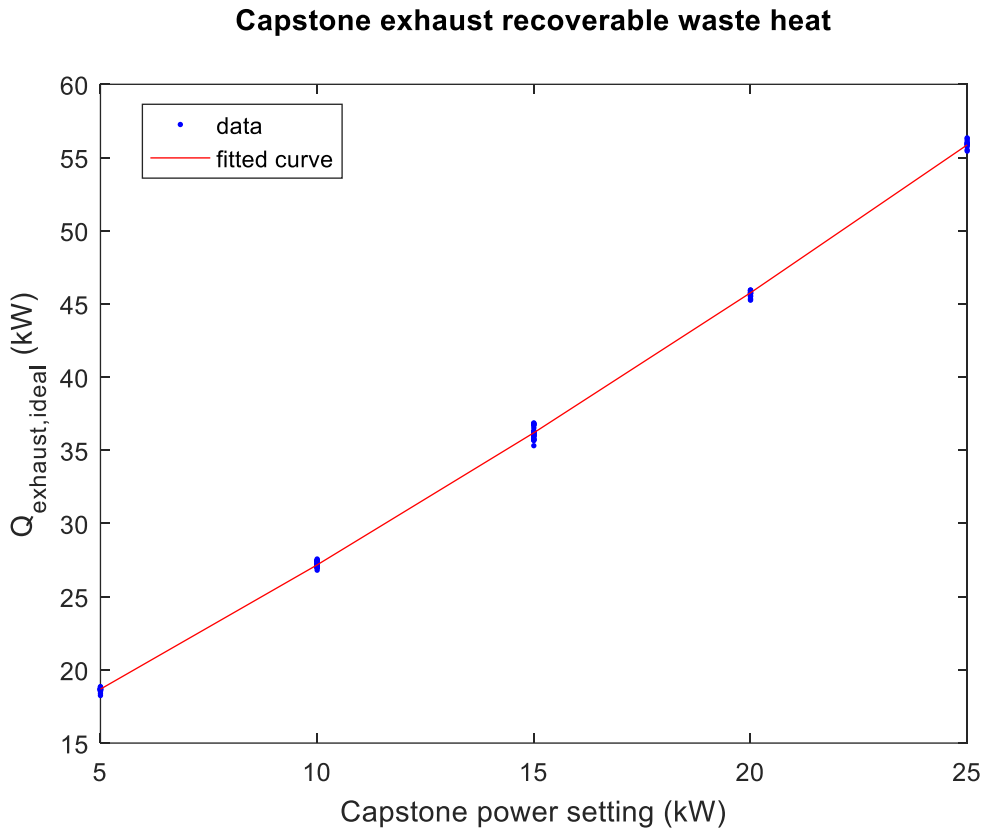

*Figure 5.5 – Available waste heat energy at each Capstone power setting from all experiments. 2nd degree polynomial fit y = 0.01077*x² + 1.536*x + 10.74 with an R² of 0.999.*

The results show that the available exhaust waste heat increases with increasing Capstone power settings. The minimum recoverable waste heat was 18.2 kW at the lowest Capstone setting of 5 kW, and the maximum waste heat was 56.3 kW at the 25 kW power setting. These results are in line with a similar heat extraction loop reported on in (Lemmens et al., 2006), which transferred a maximum of 60 kWth from a Capstone C30. This paper does not mention preventing cooling below the acid dew point, which may explain the slightly higher heat transfer.

The data provides improved insight into the recoverable waste heat over the Capstone manufacturer data, which presents the total heat in the exhaust stream. These results can be seen as indicative of what can be maximally captured from a 30 kW Capstone turbine with a diesel fuel source.

5.1.5 Heat transfer loop

The relative impact of the speed of the transfer fluid pump and the Capstone power setting on the heat transferred to the ORC system was inspected. The influence of the pump speed was unknown,

but is required to inform operating input selection for future testing. Figure 5.6 considers the heat transfer rate of the transfer fluid in the evaporator $\dot{Q}_{tf}$ (equations (28)-(30), on page 80) as a function of pump speed and Capstone power setting for all experimental data.

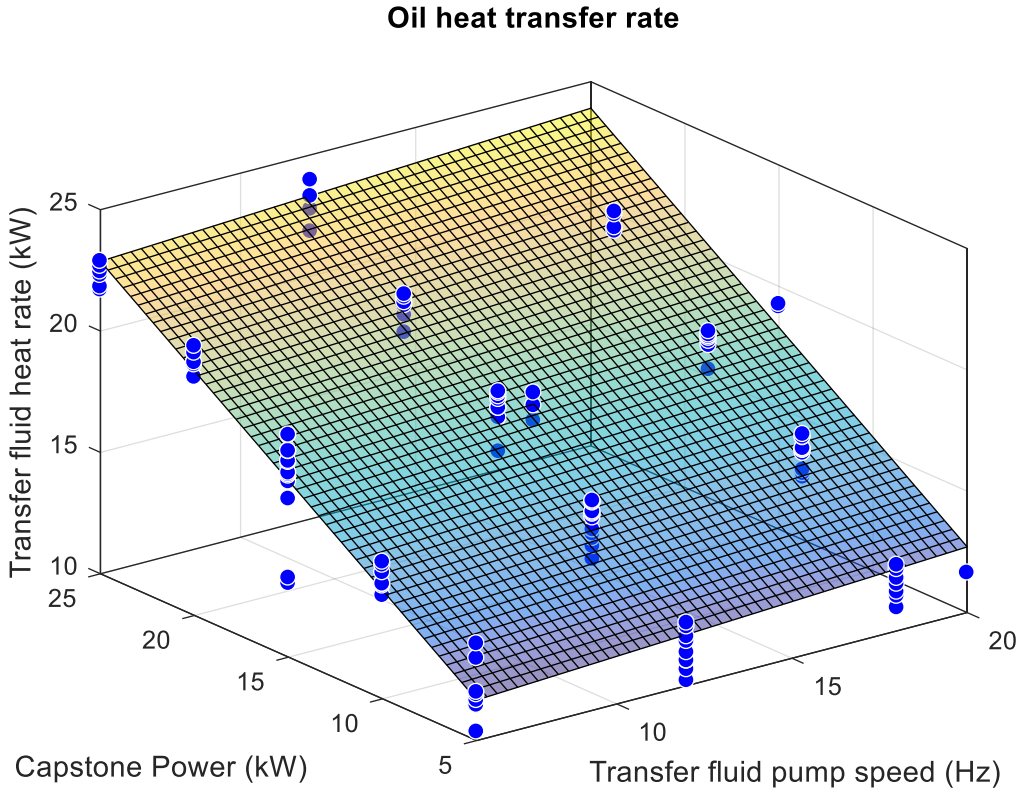

Figure 5.6 – Transfer fluid heat rate as a function of Capstone power setting and transfer fluid pump speed from all experimental data. Linear surface fit for trend visualisation with an R^2 value of 0.925. Vertical scattering is due to the variation of the other operating conditions.

The resulting linear surface fit, while simplistic, allows inspection of general relationship shown in equation (20):

$$\dot{Q}_{tf,evap} = 0.07405 f_{pump,tf} + 0.5602\, P_{Capstone} + 8.423 \quad (20)$$

Where $f_{pump,tf}$ is the frequency of the pump motor and $P_{Capstone}$ is the set electrical power in kW.

The results suggest the heat transfer rate slightly increases with increasing pump speed at each Capstone power setting. However, the heat transfer rate is approximately 7.5 times more influenced by the Capstone power setting, as this dictates the available exhaust energy. This indicates it is likely beneficial to select and maintain a single oil speed and change Capstone power to achieve different heat rates in further testing.

5.1.6 Heat absorption efficiency

The heat absorption efficiency allows inspection of controllable inputs' ability to influence the heat transferred to the ORC from the exhaust stream. Adapting the definition in (Shu et al., 2016), heat absorption efficiency (η_{abs}) is defined in equation (21) as the ratio between the measured heat absorbed by the working fluid in the evaporator $\dot{Q}_{wf,evap}$(equation (31)) and the calculated exhaust available waste heat energy (equation (19)).

$$\eta_{abs} = \frac{\dot{Q}_{evap}}{\dot{Q}_{exhaust,ideal}} \tag{21}$$

The experimental results of heat absorption efficiency at each Capstone power setting are presented in Figure 5.7. At 5 kW Capstone power the heat absorption efficiency varied from 0.3 to 0.9, decreasing to 0.3 to 0.35 at 25 kW Capstone power.

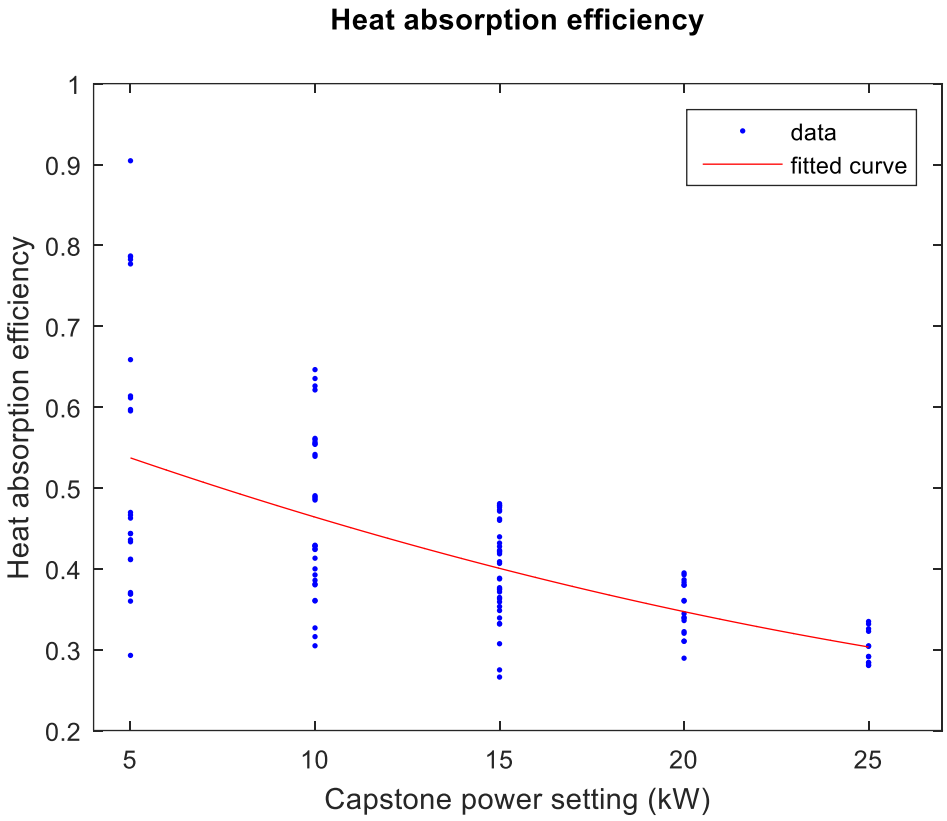

*Figure 5.7 – Heat absorption efficiency at each Capstone power setting from all experiments. 2nd degree polynomial fit y = 0.0002*x² – 0.0176*x + 0.62 with an R² of 0.37 for trend visualisation.*

The spread of data at each Capstone power setting, resulting in a low R^2 value, is due to variations in the controlled inputs. The spread of data decreases with increasing Capstone power setting, where increasing capstone settings corresponds to increased available exhaust heat energy. This suggests the controlled inputs have proportionally more of an effect on the heat absorption efficiency at lower available exhaust energy.

The decreasing trend with increasing capstone power suggests a limited ability of the system to extract heat at higher exhaust flow rates, which is primarily dictated by the finned-tube heat exchanger design for the thermal oil loop. This suggests there is scope for a revised heat exchanger design to allow better heat recovery at higher exhaust flow rates. However, the current design could be considered acceptable, as absolute values are not dissimilar to those in (Shu et al., 2016). In their study, the authors achieved a maximum of heat absorption efficiency of 100% at minimum engine load (exhaust cooled to acid dew point), decreasing to 45% at full engine load.

5.1.7 Generator behaviour

As outlined in section 4.2.8, the electrical power output from the generator was used as the measurement for ORC power in lieu of direct measurement of shaft power.

However, the supplied generator is specified to deliver grid compliant power (230 V at 50 Hz), with a self-exciting rotor winding which engages at a certain (but unspecified) RPM (WANCO, 2011). Below this frequency there is effectively no load on the scroll. During the experiments, this was observed as a drop in shaft speed at around 1600-1800 RPM as if an electric load was being engaged.

Similar concerns were raised by the authors in (Eicke and Smolen, 2015) who used an identical expander and generator. Through testing with compressed air, the voltage response of the generator as a function of generator speed was found to be non-linear. Figure 5 in (Eicke and Smolen, 2015) shows an abrupt jump in voltage from 10 V to 110 V at around 1800 RPM, and a linear response from this speed onwards to 3300 RPM.

During the experiments in this study the shaft speed fluctuated from 1500-2500 RPM. This generator behaviour means that the power measured from the generator does not necessarily directly reflect the power output of the ORC. Coupled with the fact this method cannot accurately account for losses caused by a RPM dependent generator efficiency, an alternative method for measuring the shaft power is required outlined in section 6.1.5.

5.2 Analysis of cycle performance

This section investigates the performance of the cycle and its components, using data resulting from the tests described section 4.4.3.

5.2.1 Result presentation

To observe the impact of generator load on the results, in certain analyses it is necessary to group steady state point data into cases where the load was either 500 W or 1000 W. Where this is not relevant to the inspected metric, all data points are considered. Where data has been separated into these groupings, figure captions indicate the load selection being presented.

The results in section 5.2.x are presented with test dates, to observe if the decreasing refrigerant charge and suspected increasing fouling with time had observable effects. This allows inspection if tests having similar inputs at different times of testing gave appreciably different results. There are four sets: May, June, August 11 – 21, and August 22 – 31. The August test results have been divided into two sets, the former corresponding to the lower two Capstone power settings, and the latter with the remaining higher settings, which ended with scroll expander failure.

5.2.2 Expander performance

5.2.2.1 Isentropic efficiency

The isentropic efficiency is defined as the ratio between the measured electrical power output and the isentropic expansion power (equation (22)). Note that in some of the reviewed literature, this is referred to as the electrical effectiveness.

$$\eta_{s,exp} = \frac{\dot{W}_{gross}}{\dot{m}_r(h_{exp,in} - h_{exp,out,s})} \quad (22)$$

Where $\dot{W}_{gross}$ is the measured generated electrical power, $h_{exp,in}$ is the enthalpy at the inlet and $h_{exp,out,s}$ the isentropic enthalpy at the outlet. As noted by the authors in (Declaye et al., 2013), the adiabatic definition of the isentropic efficiency cannot be used, as volumetric expanders exchange a non-negligible amount of heat with their environment.

The maximum and minimum isentropic efficiency and their operating conditions are shown in Table 5.1. Overall, isentropic efficiency was far lower than both manufacturer estimates and that found by authors using identical expanders with pure R245fa as a working fluid. Manufacturer data estimates isentropic efficiencies from 40 - 70 % at a pressure ratio of greater than 2.5 with R245fa (Air Squared Manufacturing Inc., 2015)). The authors in (Baral et al., 2015) achieved efficiencies ranging from 57.5 – 70 %, authors in (Muhammad et al., 2015) achieved 57.9 – 77.7 %, and (Bamorovat Abadi et al., 2015) achieved 60 – 70%. This illustrates the degree of impact that factors limiting performance of this system (elaborated in section 5.4) had on the efficiency of the expander.

Table 5.1 – Maximum and minimum isentropic efficiency from experimental results for 1000 W and 500 W generator load settings.

	1000 W		**500 W**	
	Maximum	Minimum	Maximum	Minimum
Isentropic efficiency (%)	49.2	5.7	31.5	11.0
Refrigerant mass flow rate (kg/s)	0.0285	0.057	0.0285	0.0668
Pressure ratio	3.49	3.52	3.94	4.76

The isentropic efficiency as a function of refrigerant mass flow rate and pressure ratio for a generator load of 1000 W is shown in Figure 5.8. It is noted that data becomes more scattered at lower mass flow rates. One reason may be the mass flow meter measurement error increases with decreasing flow rate, increasing to ± 8 % at 0.035 kg/s, additional to the ± 15 % caused by pulsation from the feed pump.

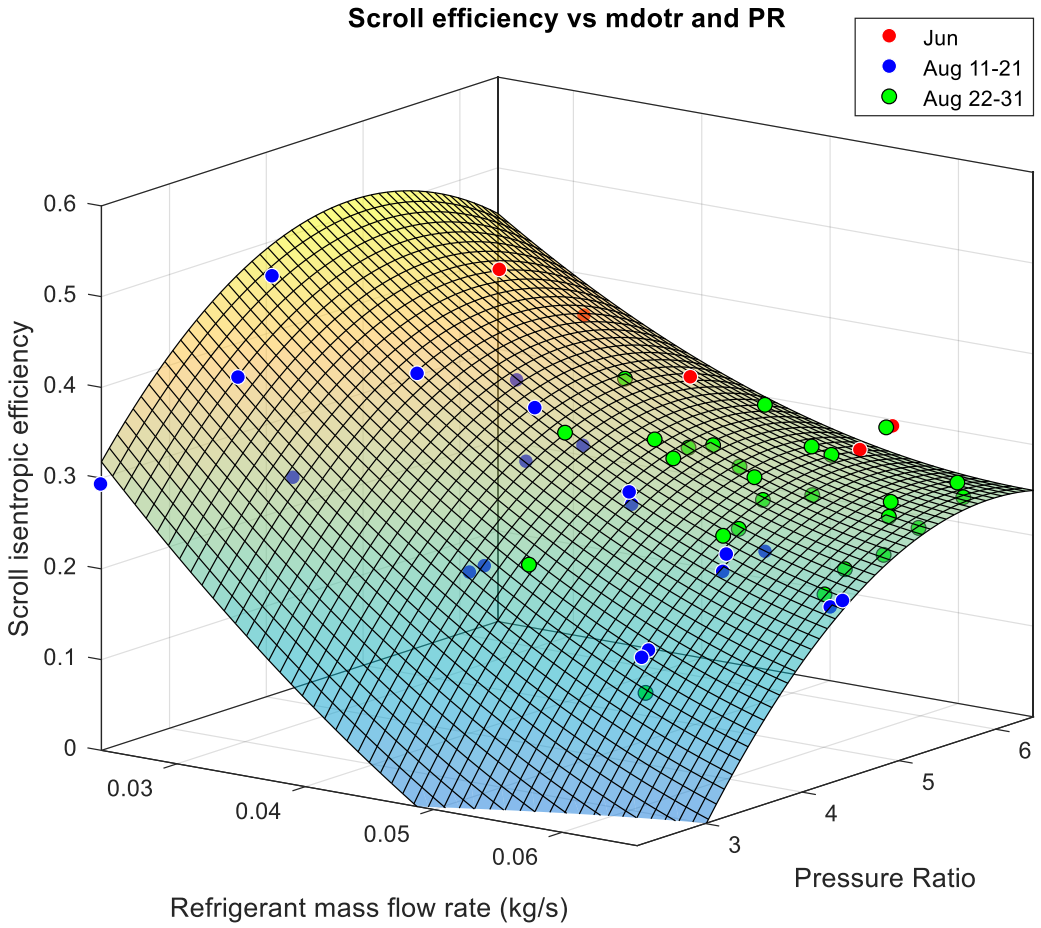

Figure 5.8 – Expander isentropic efficiency as a function of the pressure ratio and refrigerant mass flow rate at 1000 W generator load from experimental data. Second Degree polynomial surface fit for trend visualisation with an R^2 value of 0.837.

Figure 5.8 suggests that for a constant mass flow rate, the efficiency exhibits diminishing returns as pressure ratio increases. This is likely a function of increasing over-expansion losses as the pressure ratio progresses past an optimum corresponding to the built-in volume ratio of 3.5, and increasing internal leakage (Declaye et al., 2013).

For a constant pressure ratio, efficiency decreases with increasing mass flow rate. As pressure ratio is closely correlated to the rotational speed of the generator, increasing mass flow rate at a constant pressure ratio will generate proportionally less power and therefore reduce efficiency.

5.2.2.2 Expander filling factor

The filling factor is used to quantify volumetric performance, giving important insight into the expander's performance. The filling factor is defined as the ratio of the measured mass flow rate to the mass flow rate theoretically displaced by the expander (equation (23)).

$$\phi = \frac{\dot{m}_r v_{exp,in}}{N_{rot} V_{swept}} \tag{23}$$

Where $v_{exp,in}$ is the specific volume of the working fluid at the expander inlet, and V_{swept} is the swept volume of the expander per rotation specified as 12 cc/rev by the manufacturer, and N_{rot} is the rotational speed in RPM.

The maximum and minimum filling factors and their operating conditions are shown in Table 5.2. Overall, filling factors were significantly higher than those achieved by other authors testing similar sized scroll expanders. The authors in (Lemort et al., 2012) observed filling factors ranging from 1.02 to 1.1 and the authors in (Woodland et al., 2012) observed filling factors of 0.81 – 2.05. This poor volumetric performance is likely the reason for the observed poor isentropic efficiency, as volumetric expanders are most efficient when at a filling factor of unity, with decreasing efficiency above this (Woodland et al., 2012).

Table 5.2 – Maximum and minimum filling factors from experimental results for 1000 W and 500 W generator load settings.

	1000 W		**500 W**	
	Maximum	Minimum	Maximum	Minimum
Filling Factor	5.16	1.61	4.48	1.66
Refrigerant mass flow rate (kg/s)	0.0571	0.0285	0.0571	0.0351
Pressure ratio	3.59	3.49	3.39	4.77

The filling factor as a function of refrigerant mass flow rate and pressure ratio for a generator load of 1000 W is shown in Figure 5.9.

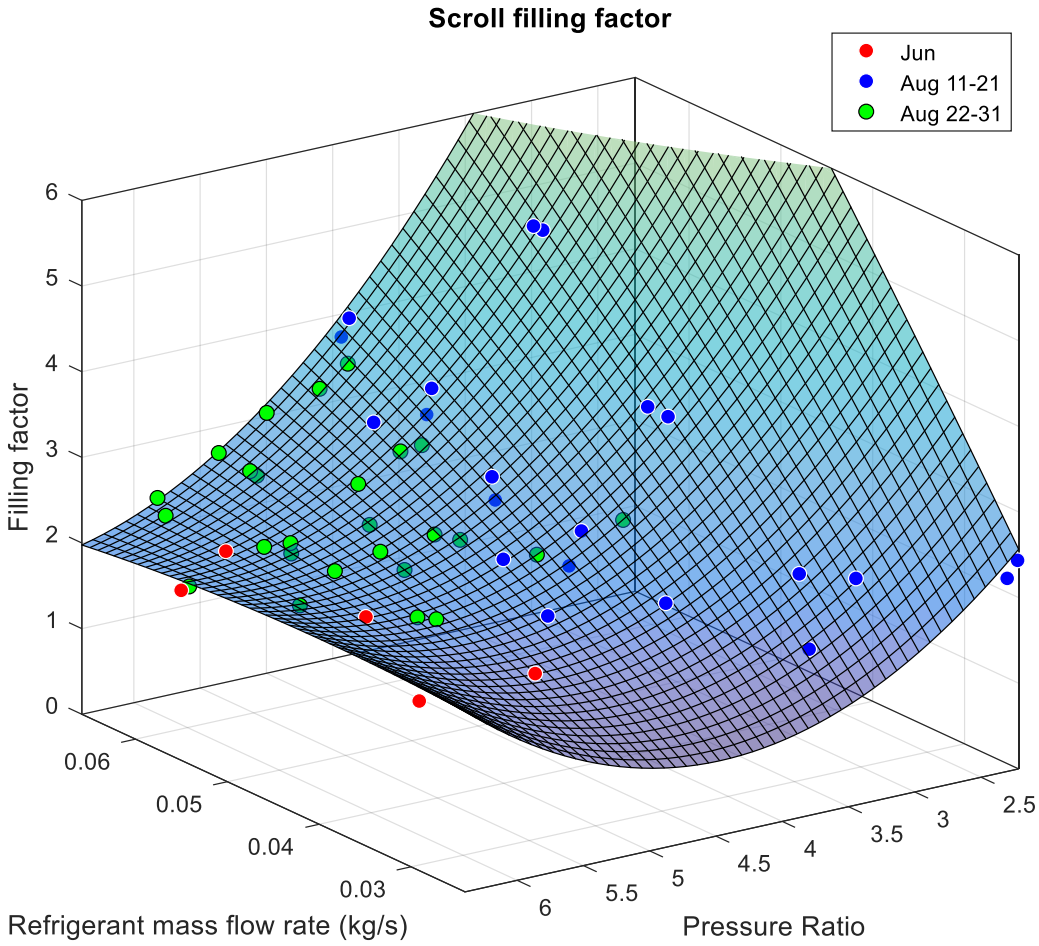

Figure 5.9 – Expander filling factor as a function of as a function of the pressure ratio and refrigerant mass flow rate at 1000 W generator load from experimental data. Second Degree polynomial surface fit for trend visualisation with an R^2 value of 0.925.

Figure 5.9 shows that at a constant mass flow rate, the filling factor is influenced by the pressure ratio, decreasing with increasing pressure ratio. This is consistent with the findings of (Woodland et al., 2012) which found the filling factor to be a function of the rotational speed of the expander, given that for these experiments increasing pressure ratio corresponds to increasing expander speed.

This trend becomes more prominent with increasing flow rate. This is possibly because at a given pressure ratio the increasing mass flow rate is being forced through leakage pathways. This leakage is then more evident at higher mass flow rates and at lower pressure ratios.

The values for filling factor in this study are unusually high with no obvious cause, calling their validity into question. The rotational speed measurement was checked with a handheld digital tachometer, and the mass flow rate measurements are approximately the same as those calculated by theoretical pump displacement (section 5.2.6.2). Therefore, the remaining possible causes for large filling factors could be a result of large internal leakage, or from inaccuracy in the REFPROP mixture model used to determine specific volume at the expander inlet.

Following the expander disassembly (section 5.4), the scroll seal did appear to have a chip near the tip folded over the scroll face, although it is possible (but unlikely) this was caused during

disassembly. Additionally, several seized bearings would also have imposed increased resistance to rotation. It is possible a combination of these factors lead to large radial leakage.

There is some uncertainty concerning REFPROP's handling of the two component refrigerant mixture M1. REFPROP indicates the refrigerant was at a superheated state at the expander inlet for all steady state pressures and temperatures in the experiments. However, when the data is re-evaluated with REFPROP using pure R245fa and R365mfc at the same pressures and temperatures, the R365mfc is sometimes in a two-phase state. Selecting only steady state points that ensure both constituent refrigerants are at a superheated state and re-evaluating the filling factor with M1, the resulting range decreases to 1.61 – 2.42. This would be consistent with a theory that the M1 mixture may have been in a two-phase state for a number of test points, causing REFPROP to underestimate the fluid density at the inlet, resulting in high filling factors.

5.2.3 Cycle performance

5.2.3.1 Cycle efficiency

The cycle efficiency is used to represent the performance of the whole system, and is defined as a ratio of the net work produced to the total heat input in equation (24).

$$\eta_{cycle} = \frac{\dot{W}_{net}}{\dot{Q}_{evap}} = \frac{\dot{W}_{gross} - \dot{W}_{pump,wf}}{\dot{m}_r(h_{evap,in} - h_{evap,out})} \quad (24)$$

Where $\dot{W}_{net}$ is the difference between the electrical power produced by the expander and the power consumed by the working fluid pump. Additionally, the global cycle efficiency is examined, where $\dot{W}_{net,global}$ incorporates the parasitic load of the oil transfer pump, shown in equation (25).

$$\dot{W}_{net,global} = \dot{W}_{gross} - \dot{W}_{pump,wf} - \dot{W}_{pump,tf} \quad (25)$$

The maximum and minimum achieved cycle efficiencies and their operating conditions are shown in Table 5.3. As with isentropic efficiency, overall values are far lower than both design estimates and those found by authors using identical expanders with pure R245fa as a working fluid.

5.2.3.2 Comparison to theoretical thermodynamic simulation

Using the experimentally measured heat source and sink temperatures, and design analysis parameters from section 3.1.4, the cycle efficiency has a theoretical maximum of 11.2% at the highest operating point. This is significantly higher than the experimental result of 3.56%.

5.2.3.3 Comparison to similar published works

The authors in (Baral et al., 2015) achieved efficiencies ranging from 2.80% - 7.6%, (Muhammad et al., 2015) achieved 4.5% - 5.75%, and (Bamorovat Abadi et al., 2015) achieved 6.0 – 6.55%. This suggests further evidence of the current system being constrained in its operation by factors such as poor expander performance.

Table 5.3 - Maximum and minimum cycle efficiencies from experimental results for 1000 W and 500 W generator load settings. (Global efficiency in brackets).

	1000 W		**500 W**	
	Maximum	Minimum	Maximum	Minimum
Cycle efficiency (incl. oil transfer)	3.56 (2.33)	-0.07 (-0.96)	1.63 (0.77)	-1.06 (-3.05)
Refrigerant mass flow rate (kg/s)	0.0329	0.0571	0.0351 (0.0439)	0.0176
Pressure ratio	5.24	3.52	4.77 (5.24)	2.07

The cycle efficiency as a function of refrigerant mass flow rate and pressure ratio for a generator load of 1000 W is shown in Figure 5.10.

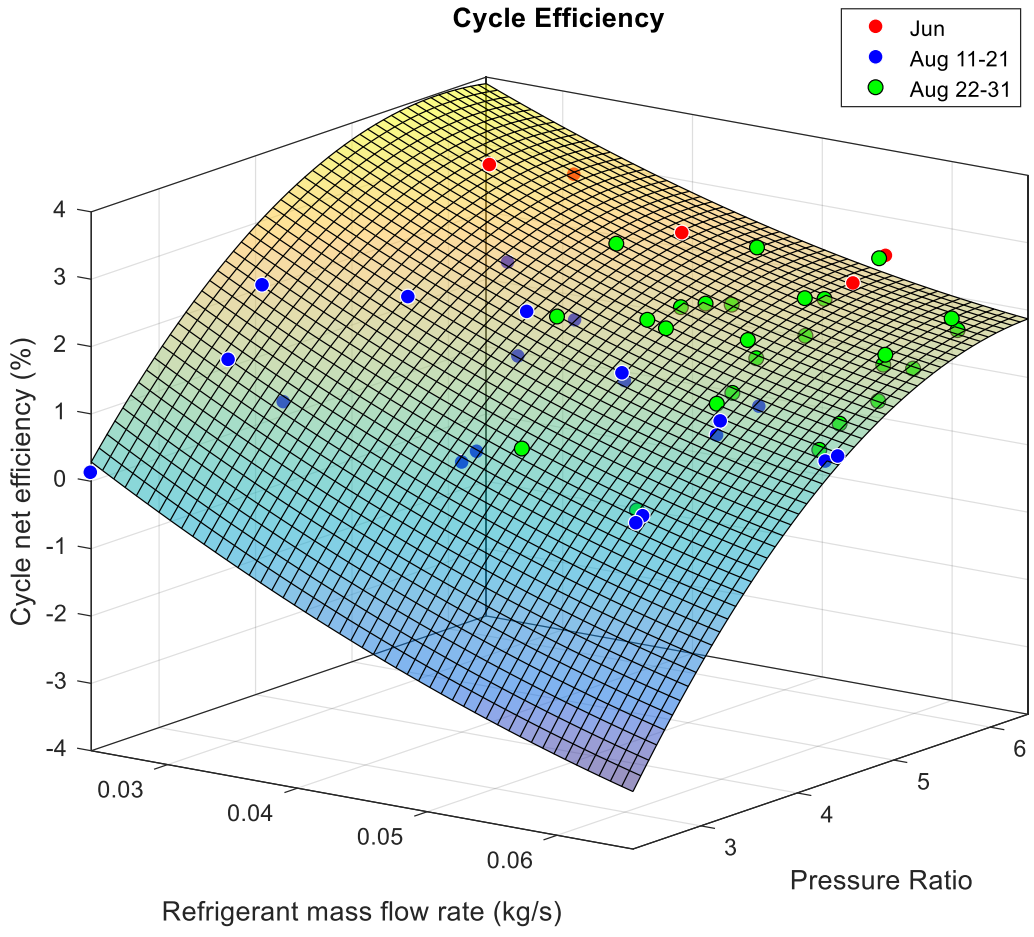

Figure 5.10 – Cycle net efficiency as a function of pressure ratio and refrigerant mass flow rate at 1000 W generator load from experimental data. Second Degree polynomial surface fit for trend visualisation with an R^2 value of 0.89.

Figure 5.10 shows a similar trend to (Baral et al., 2015) and (Declaye et al., 2013), in which cycle efficiency monotonically increases with pressure ratio, with diminishing returns at higher pressure ratios.

5.2.3.4 Second law efficiency

The absolute values for cycle efficiency are low, and in small systems at these available temperature ranges this can be dictated by the Carnot efficiency. The second law efficiency is defined as a ratio between the cycle efficiency and the Carnot efficiency in equation (26).

$$\eta_{cycle,II} = \frac{\eta_{cycle}}{\eta_{Carnot}} \tag{26}$$

Where the Carnot efficiency is calculated in equation (27), with temperatures in Kelvin.

$$\eta_{carnot} = 1 - \frac{T_{water,in}}{T_{tf,in}} \tag{27}$$

The maximum second law efficiency was 11.8 %, at a pressure ratio of 5.24 and a mass flow rate of 0.0329 kg/s. This at the low end compared to other authors with identical expanders and R245fa working fluid, with (Muhammad et al., 2015) and (Baral et al., 2015) achieving 14.6 % and 31.3 % respectively. (Bamorovat Abadi et al., 2015) achieved 22.5 % with a 0.6/0.4 R245fa/R134a mixture and identical expander. Higher values in similar sized systems are possible as shown by (Declaye et al., 2013), who achieved a maximum second law efficiency of 48%. The low second law efficiency in this study (with the majority around 5 %) is to be expected given the low expander performance.

The second law efficiency as a function of refrigerant mass flow rate and pressure ratio for a generator load of 1000 W is shown in Figure 5.11. The influence of the expander efficiency on second law efficiency can be seen, with a similar trend visible.

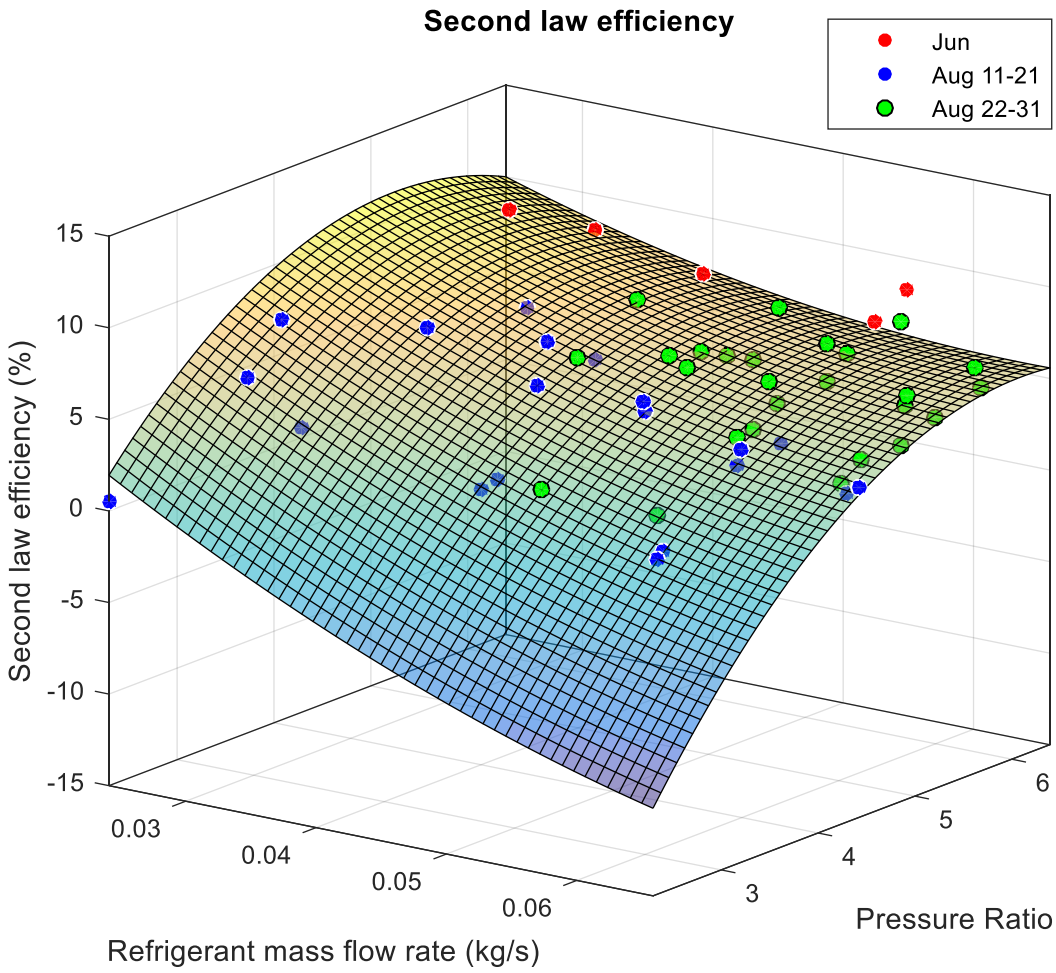

Figure 5.11 – Second law efficiency as a function of pressure ratio and refrigerant mass flow rate at 1000 W generator load from experimental data. Second Degree polynomial surface fit for trend visualisation with an R^2 value of 0.83.

5.2.4 Cycle power

The maximum and minimum achieved cycle powers calculated from equations (23) and (24) are shown in Table 5.4. It is important to note the experimental values are electrical power output, which does not take into account generator losses, as opposed to direct measurement of shaft power. Overall, the observed values reflect the poor expander performance and are far lower than those found by other authors using identical expanders with pure R245fa as a working fluid. Presenting electrical measured power, (Muhammad et al., 2015) achieved a maximum of 1001 W. Using direct shaft measurement, (Baral et al., 2015) and (Bamorovat Abadi et al., 2015) achieved 1.2 kW and 1.4 kW respectively.

Table 5.4 – Maximum and minimum cycle generated power from experimental results for 1000 W and 500 W generator load settings.

	1000 W		**500 W**	
	Maximum	Minimum	Maximum	Minimum
$\dot{W}_{gross}$ (W)	597.8	115.7	422.6	31.9
$\dot{W}_{net}$ (W)	391.4	-10.7	218.4	-56.4
$\dot{W}_{net,global}$(W)	284.7	-140	111.7	-163.2

The gross electrical generated power as a function of refrigerant mass flow rate and pressure ratio for a generator load of 1000 W is shown in Figure 5.12.

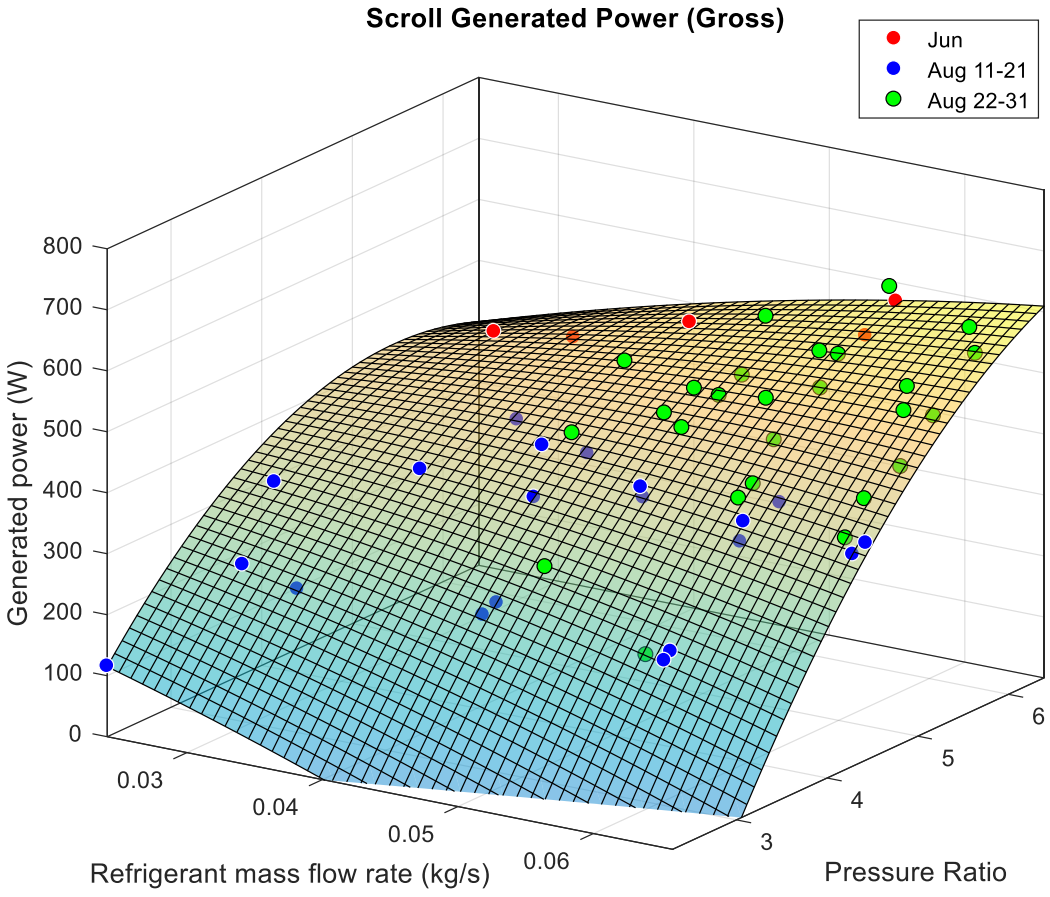

Figure 5.12 - Expander generated electrical power as a function of pressure ratio and refrigerant mass flow rate at 1000 W generator load from experimental data. Second Degree polynomial surface fit for trend visualisation with an R^2 value of 0.906.

Figure 5.12 shows a similar trend to (Declaye et al., 2013), where power appears to be a monotonically increasing function of the pressure ratio, and to a certain extent the mass flow rate. This follows the relationship between the expander rotational speed as a function of pressure ratio and mass flow rate, shown in Figure 5.13 for a generator load of 1000 W.

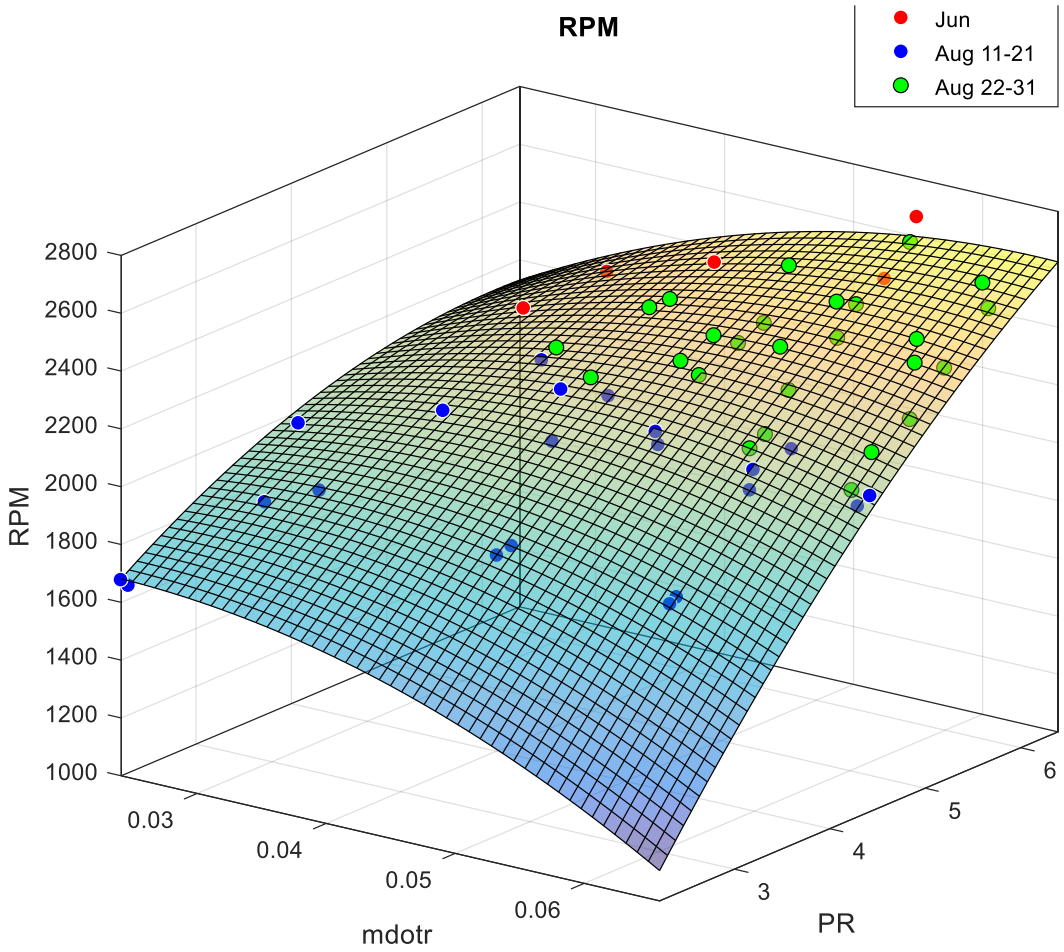

Figure 5.13 – Generator shaft speed as a function of pressure ratio and refrigerant mass flow rate at 1000 W generator load from experimental data. Second Degree polynomial surface fit for trend visualisation with an R^2 value of 0.931.

It should be noted that the maximum rotational speed of 2666 RPM is significantly below the speeds reported by authors using the same expander at comparable pressure ratios, ranging from 3000 - 3500 RPM which is the recommended operating range of the generator (Baral et al., 2015),(Muhammad et al., 2015). This may have been due to the choice of working fluid, or increased bearing losses in the expander due to residue build-up, detailed in section 5.4.

5.2.5 Heat balances

To evaluate the accuracy of the measurements, heat balances across the evaporator and condenser are compared for all steady state operating points. For the evaporator, the heat transfer rate of the transfer fluid (equation (28)-(30)) was calculated using c_p values from manufacturer data (equation (13), page 47). REFPROP was used to calculate the enthalpies for the working fluid at the given states (equation (31)). For the condenser, REPROP was used to calculate the enthalpy of the working fluid and the water, which required an assumption the water pressure was constant at 400 kPa (equation (32) and (33)).

$$\dot{Q}_{tf,in} = \dot{m}_{tf} \cdot c_{p,tf,in} \cdot T_{tf,in} \quad (28)$$

$$\dot{Q}_{tf,out} = \dot{m}_{tf} \cdot c_{p,tf,out} \cdot T_{tf,out} \quad (29)$$

$$\dot{Q}_{tf,evap} = \dot{Q}_{tf,in} - \dot{Q}_{tf,out} \quad (30)$$

$$\dot{Q}_{wf,evap} = \dot{m}_{wf} \cdot (h_{wf,evap,in} - h_{wf,evap,out}) \quad (31)$$

$$\dot{Q}_{water,cond} = \dot{m}_{water} \cdot (h_{water,out} - h_{water,in}) \quad (32)$$

$$\dot{Q}_{wf,cond} = \dot{m}_{wf} \cdot (h_{wf,cond,in} - h_{wf,cond,out}) \quad (33)$$

Comparing the calculated heat transfer rate of the two fluids in each heat exchanger gives insight into the accuracy of the calculations, and is shown in Figure 5.14. It is anticipated that comparing this data will approximately result in a 1:1 relationship (Quoilin, 2007). In Figure 5.14 (a), the evaporator transfer rates for all steady state points are plotted (equations (30 and (31). In Figure 5.14 (b), the condenser transfer rates for all steady state points are plotted (equations (32) and (33)).

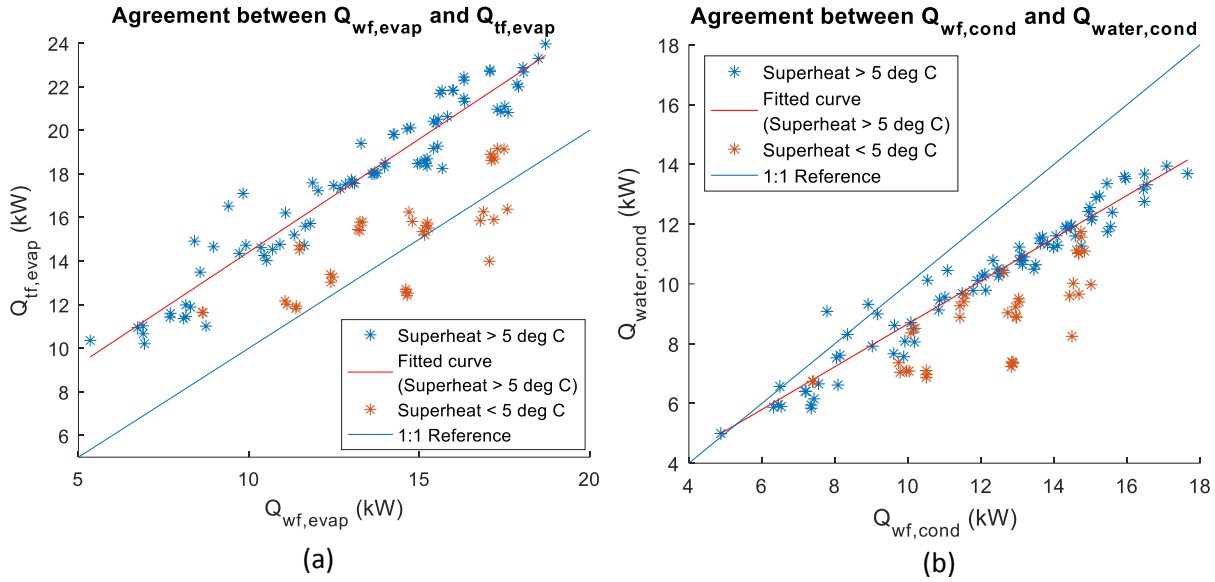

Figure 5.14 – (a) Agreement between the calculated heat transfer rates for working fluid and transfer fluid in evaporator. Linear trend line with an R^2 value of 0.926. (b) Agreement between the calculated heat transfer rates for working fluid and water in condenser. Linear trend line with an R^2 value of 0.948. Both: Data from experimental results, blue line presents 1:1 reference.

The data in Figure 5.14 shows more spread than that from other authors, whose heat agreement was close to the 1:1 reference line (Quoilin, 2007). Figure 5.14 (a) shows this spread is reduced by neglecting points where superheat at the expander inlet is less than 5 °C (shown in orange), suggesting the M1 refrigerant may have been in a two-phase state causing REFPROP to incorrectly calculate its enthalpy.

Figure 5.14 (a) shows that for the evaporator there appears to be a systematic offset above the 1:1 reference line, with the trend line having a slope of 1.04. There are several possible sources of error that could cause this. On the transfer fluid side, the c_p of the oil may be different to manufacturer data, as there was fouling in the transfer loop, with rust discovered in the oil. Additionally, the oil mass flow rate, as mentioned in section 4.2.5, was only calculated at one temperature (and therefore

viscosity) so may be incorrect. On the working fluid side, REFPROP may be inaccurately calculating the enthalpy of the two component refrigerant mixture. The transfer fluid having a greater heat transfer rate than the working fluid was somewhat expected as heat is lost to the environment. However, this difference would be expected to be small in comparison to the heat transfer values, given the insulation around the evaporator.

Figure 5.14 (b) shows that for the condenser there appears to be a gradient difference below the 1:1 reference line, with a slope of 0.72 and R^2 value of 0.948. This indicates the calculated working fluid transfer rate was greater than that of the water. As this disparity increases at higher heat rates, this may be partially due to heat loss to the surroundings, as the condenser was not insulated. Additionally, the water volume flow rate sensor had a faulty connection to the DAQ unit, which was not discovered until testing was complete. However, as the volume flow was kept constant to within approximately ± 15%, missing data was filled in with the average flow value (0.95 L/s).

5.2.6 Working fluid pump

5.2.6.1 Isentropic efficiency

The isentropic efficiency of the working fluid pump is defined as the ratio of the isentropic compression power to the measured electrical input power (equation (34).

$$\eta_{s,pump,wf} = \frac{\dot{m}_r(h_{pump,wf,out,s} - h_{pump,wf,in})}{\dot{W}_{pump,wf}} \quad (34)$$

The pump isentropic efficiency is shown as a function of refrigerant mass flow rate and pressure difference between the pump inlet and outlet for all steady state data points in Figure 5.15.

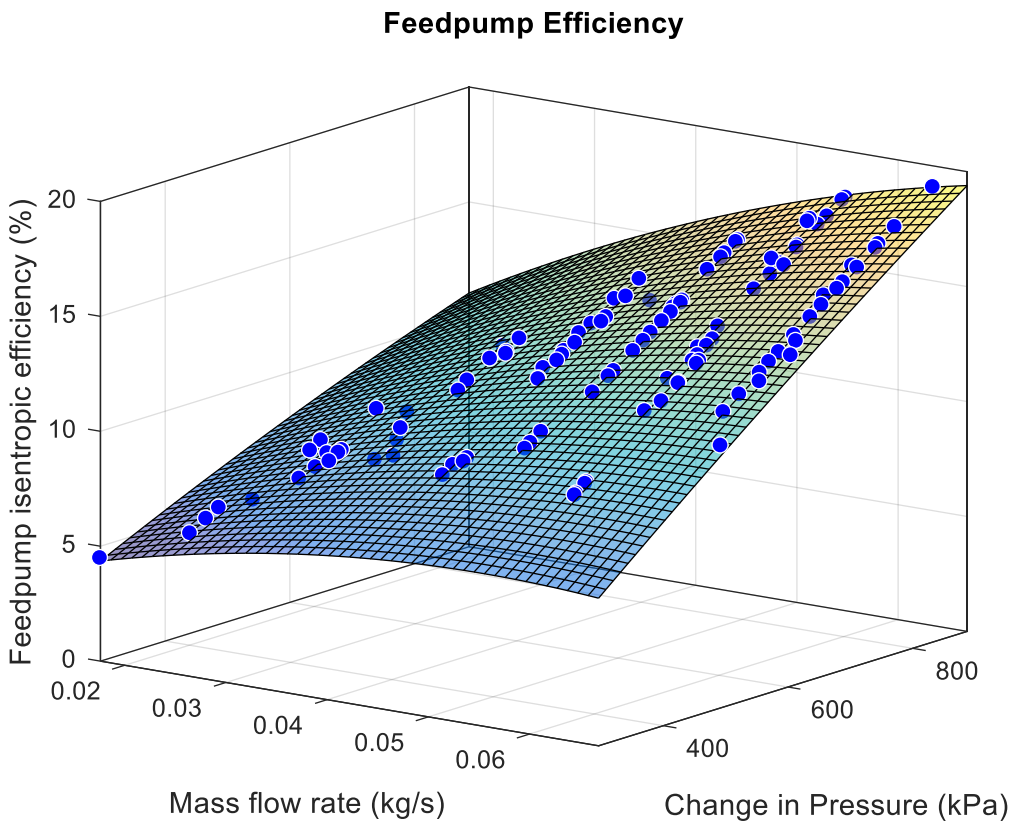

Figure 5.15 – Working fluid pump isentropic efficiency as a function of mass flow rate and change in pressure across the pump for all data points. Second Degree polynomial surface fit for trend visualisation with an R^2 value of 0.992.

Overall the pump shows a low isentropic efficiency, ranging from 4.5 % – 19.1 %, and appears to be a monotonically increasing function of the change in pressure at a fixed mass flow rate. The values of pump efficiency are similar to work by (Quoilin, 2007), who used a similar sized pump achieving an efficiency of 15 %. These low efficiency values are acceptable as the purpose of the pump is to provide a variable, accurate flow rate rather than maximise efficiency. In a more developed system where the optimal flow rate range is known, a suitable pump with a high efficiency at those operating conditions can be selected.

5.2.6.2 Flow rate

In previous studies on this ORC system, prior to installation of a refrigerant mass flow meter, the refrigerant flow was indirectly measured using equation (35) (Southon, 2014).

$$\dot{m}_{wf,pump} = \rho V (1 - \sigma) \frac{1425}{3000} f_{pump,wf} \tag{35}$$

Where ρ is the fluid density at the pump inlet, V is the volume displaced by a single revolution of the pump, $f_{pump,wf}$ is the frequency of the pump motor (set by the user), $\frac{1425}{3000}$ is the expected pump shaft/electric frequency ratio from the name plate of the motor, and σ is the motor slip factor. This method introduced a large uncertainty, due to the unknown size and behaviour of the motor slip factor. In keeping with study by Southon, a value of 0.05 was assumed.

The measured mass flow rate for all experimental data is shown in Figure 5.16 as a function of the pump input controller speed and pressure difference between the pump inlet and outlet.

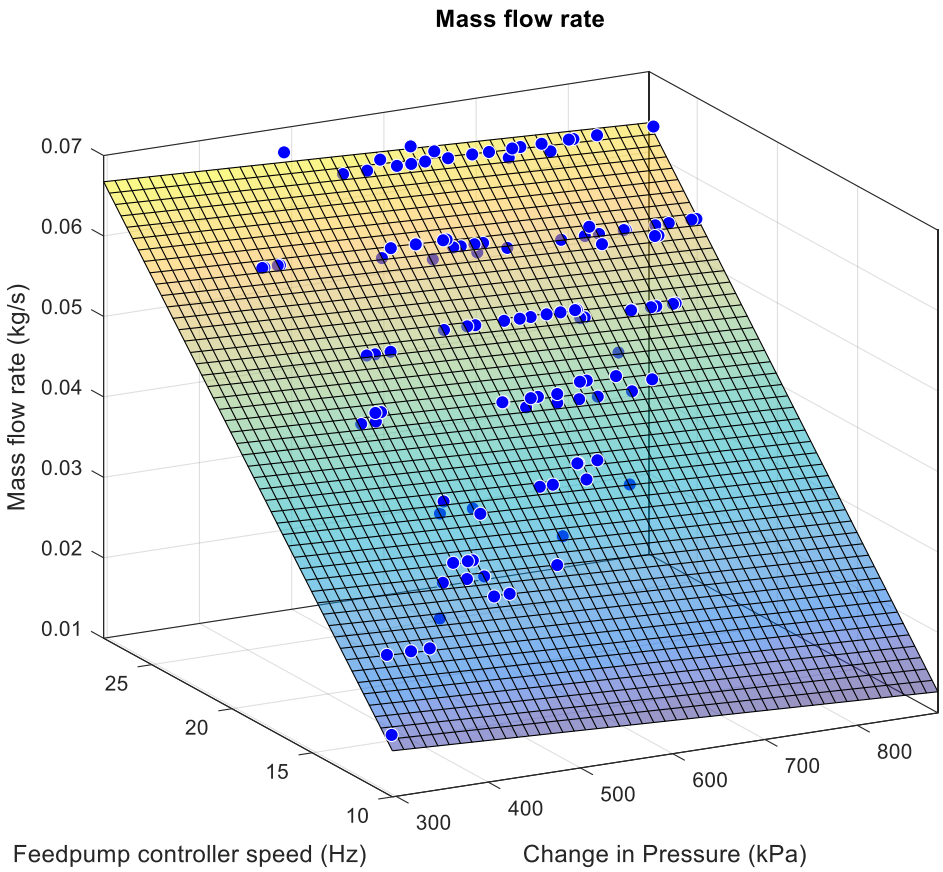

Figure 5.16 – Working fluid pump measured mass flow rate as a function of set controller speed and change in pressure across the pump. Linear surface fit with an R^2 value of 0.984.

The results indicate the refrigerant mass flow rate is primarily dependent on the input controller speed, which is to be expected. The mass flow rate shows a slight decrease with increasing pressure differential at a constant controller speed, with approximately 5 % difference across the observed pressure range. This change may be due to increased motor slip at higher pressure differentials.

The theoretical mass flow rate as calculated in equation (35) is compared to the measured mass flow rate for all experimental data in Figure 5.17.

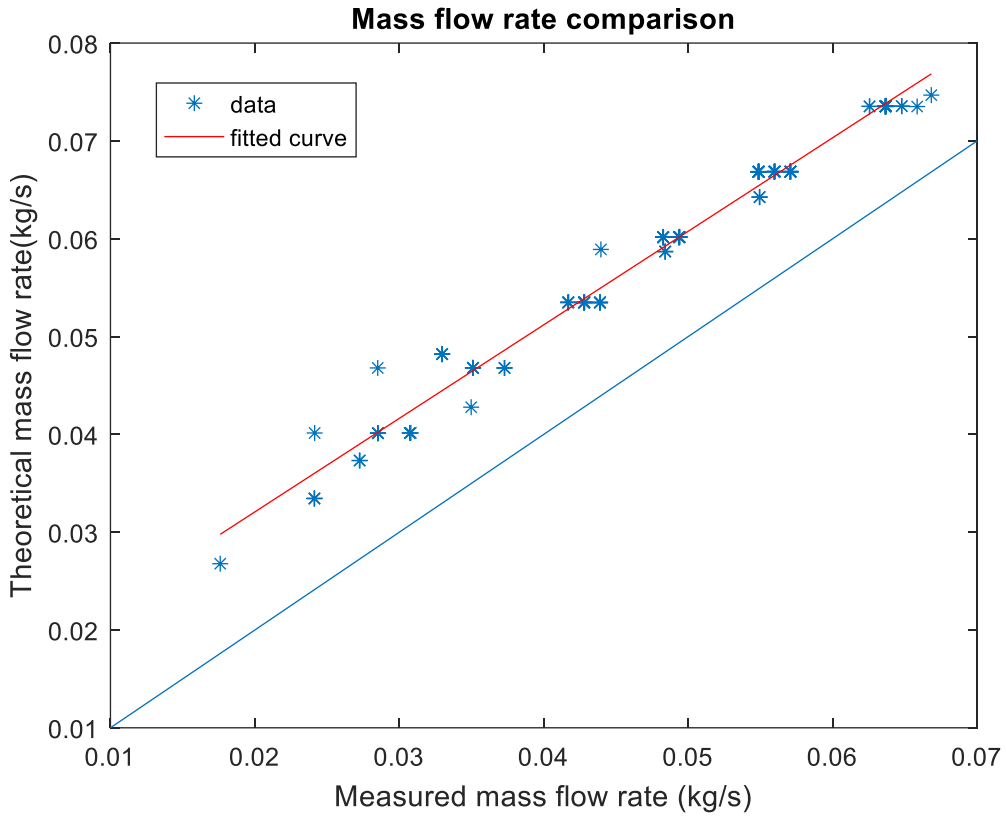

Figure 5.17 – Measured refrigerant mass flow rate compared with theoretical mass flow rate calculated using pump displacement method for all experimental data. Linear line of best fit, with an R^2 value of 0.982.

Figure 5.17 shows the measured mass flow rate was, on average, systematically lower than the value calculated directly by pump displacement, with a slope of 0.956. The average linear offset of 0.0130 kg/s translates to the measured mass flow rate being considerably lower than the theoretical value, which overestimates flow from 66 % - 11.6 % over the experimental data. Horizontal data spread at a constant theoretical flow rate values is likely caused by the effect of increasing pressure differential on motor slip shown in Figure 5.16.

Together, Figure 5.16 and Figure 5.17 demonstrate the need to measure fluid flow directly as opposed to a theoretical function of controller speed and displacement. These observations agree with work by (Bamorovat Abadi et al., 2015), who reach a similar conclusion.

5.2.7 Summary

Analysis of the results from the tests in section 4.4.3 showed the system performed poorly compared design estimates and similar studies by other authors. The expander had a maximum isentropic efficiency of 42.9 %, and consistently high filling factors with a minimum filling factor of 1.61. The maximum power output was 597.8 W, which limited cycle net efficiency to a maximum of 3.56 %, approximately half of that achieved by comparable studies. Similarly, second law efficiency was the lowest among the compared published work with a maximum of 11.8%.

Heat balances on the evaporator and condenser showed the calculated heat transfer rates did not have the expected agreement, pointing to underlying uncertainty in the measurements and possibly REFPROP handling of the M1 refrigerant mixture. The working fluid pump had a maximum isentropic

efficiency of 19.11 %, and a flow rate analysis showed the necessity for a direct fluid flow measurement as opposed to relying on one calculated from a theoretical displacement.

For better system analysis, future work would need to repeat tests with a pure working fluid to eliminate uncertainty around M1 refrigerant behaviour, in a system that retains a constant working fluid level throughout testing, further discussed in Chapter 6.

5.3 Analysis of DVR tests

This section presents the results and analysis of the limited DVR tests in section 4.4.4, to investigate the effect of varying the working fluid charge on the range of possible operation of the system.

5.3.1 Results

In the DVR tests, three heat source temperatures were tested by selecting 5, 10 and 15 kW power settings on the Capstone turbine, with transfer oil pump speed held constant. At each DVR, the pressure ratio was maximised across a needle valve. At each pressure ratio, the refrigerant mass flow rate was maximised while maintaining a steady fluid level in the buffer tank. The achieved pressure ratios and corresponding mass flow rates of the experiments are shown in Figure 5.18 and Figure 5.19.

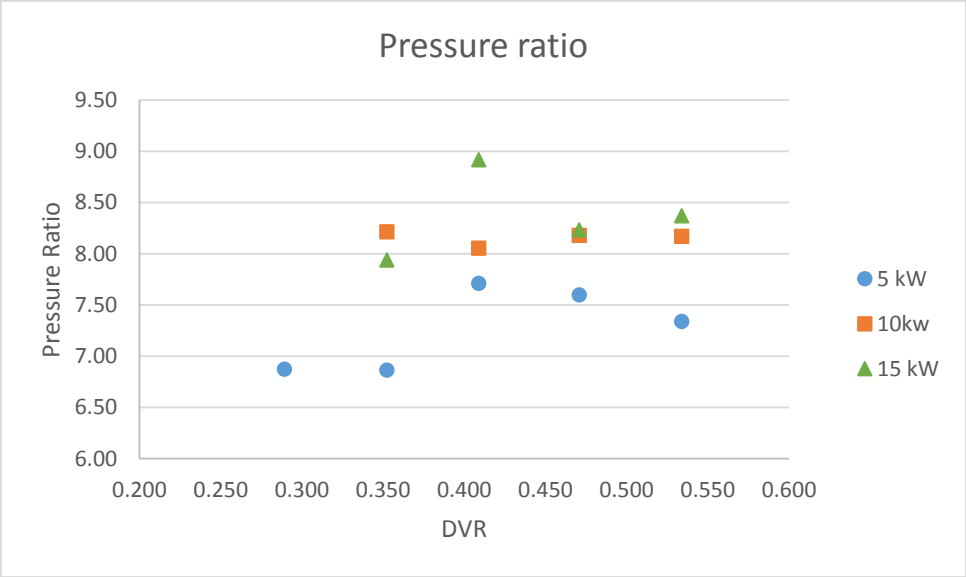

Figure 5.18 – Maximum achieved pressure ratio at each DVR for each heat source setting.

Figure 5.18 shows higher pressure ratios were achieved at greater heat source settings for each DVR. The results weakly suggest the DVR influenced on the maximum achievable pressure ratio for the system for 5 and 15 kW settings, but are inconclusive.

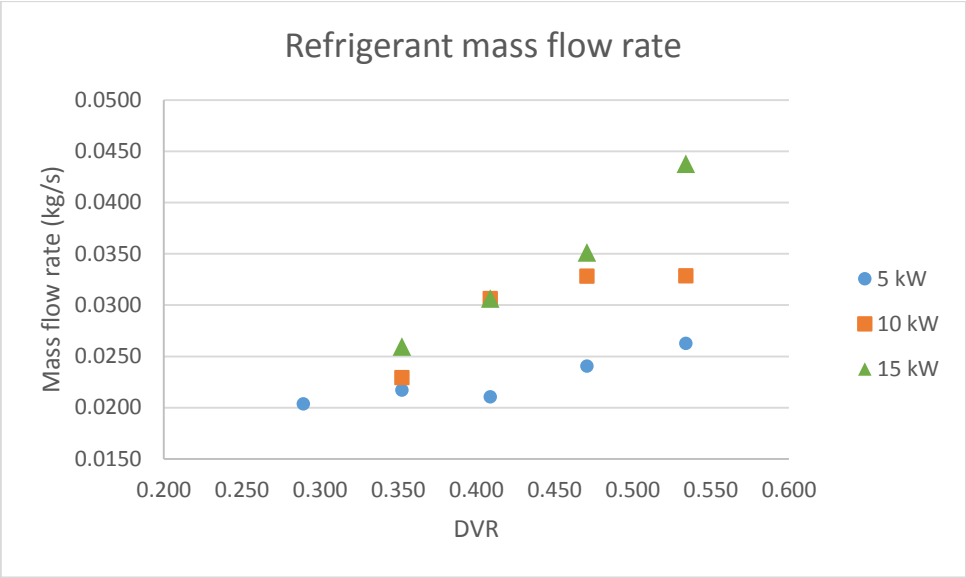

Figure 5.19 – Maximum mass flow rate at each DVR for each heat source setting.

Figure 5.19 suggests that the DVR had an influence on the maximum achievable mass flow rate, which increased with increasing DVR. This agrees with the observation made during the experiments that as the DVR was decreased, the system was starved of working fluid. The limiting factor was often the exiting temperature of the oil from the evaporator (limit 100 °C), or the working fluid maximum temperature (140 °C). At the lowest DVR, operation was limited to the lowest heat input setting creating a single data point.

5.3.2 Heat absorption efficiency

The influence of the DVR on the heat absorption efficiency (η_{abs}), as calculated in equation (21), page 69, is investigated. Figure 5.20 presents the heat absorption efficiency at each DVR for the three input Capstone turbine heat settings. Figure 5.20 shows that the heat absorption efficiency of the system decreased with increasing heat source setting from 5 – 15 kW, indicating decreasing proportional heat extraction. Additionally, at each heat setting, heat absorption efficiency increases with increasing DVR. This effect is more pronounced at higher heat settings. This suggests DVR does influence the ability of system to utilize the heat source.

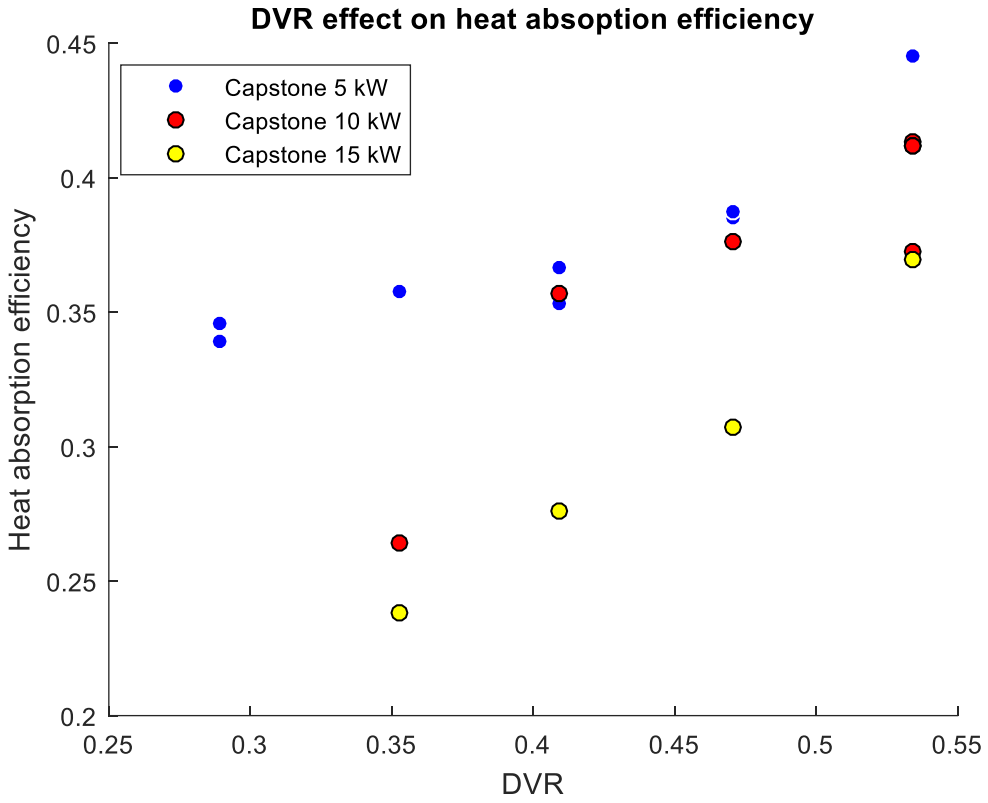

Figure 5.20 – Heat absorption efficiency for all steady state points achieved at each DVR for the three input heat source settings.

5.3.3 Subcooling

The degree of subcooling is the difference between the saturation temperature of the refrigerant in the condenser and the temperature of the exiting working fluid (equation (36)).

$$\Delta T_{cond,out} = T_{sat,cond,out} - T_{wf,cond,out} \tag{36}$$

In this study, the degree of subcooling is calculated with the saturation temperature specified at the exhaust pressure of the condenser.

The degree of subcooling at a certain operating working fluid mass flow rate is believed to be influenced by the working fluid charge in the system (Quoilin, 2007) (Li et al., 2015), due to its impact on the liquid surface area for heat exchange. In order to examine this effect, the degree of subcooling for all steady state operating points at each DVR is shown in Figure 5.21. The degree of subcooling increases with increasing DVR, a similar trend to Figure 38 in (Quoilin, 2007). This would support the hypothesis that the increasing surface area in the heat exchanger with increasing DVR leads to a greater degree of subcooling.

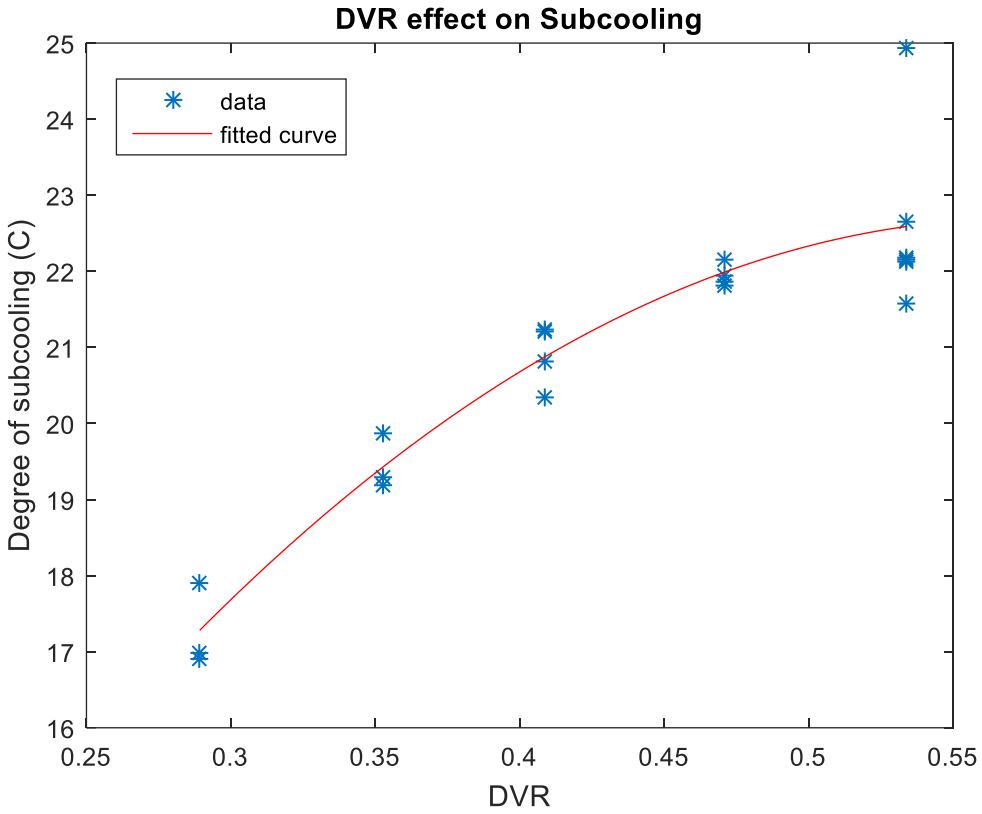

Figure 5.21 – Degree of subcooling for all steady state operating points at each tested DVR achieved in experiments. 2nd degree polynomial fit for trend for trend visualization with an R^2 value of 0.888.

5.3.4 Summary

Analysis of the results from the tests in section 4.4.4 suggest the working fluid charge in the system influences operation, as suggested by the authors in (Li et al., 2015). Although the influence of DVR on maximum achievable pressure ratio was inconclusive, decreasing the DVR reduced the maximum achievable mass flow rate at each of the input heat source settings.

Decreasing the DVR reduced the ability of the system to utilize the available heat stream for all heat settings, shown by decreasing the heat absorption efficiency. Decreasing the DVR also reduced the degree of subcooling in the condenser.

These results support the need for further testing the impact of the working fluid charge in a fully functioning system.

5.4 Operational failures/System Forensics

This section provides a synopsis of the experimental issues encountered during testing and their possible causes and effects. For a full timeline of these events refer to the experimental observations in Appendix D, and further disassembly photos in Appendix E.

During the first set of experiments, it was noted that the expander began making sounds indicating bearing failure. Eventually the expander became inoperable, and upon disassembly it was found all five bearings were without lubricant. Two had resistance to rotation and the rear main shaft bearing was completely seized, with the shaft rotating on the inner race. Ferrous metal flakes were found in

the housing, and found in the refrigerant upon draining, suggesting transport downstream in the system. The bearings were dissected and determined to be a potential source of these flakes as the scroll faces (another source of steel in the system) showed no such wear, shown in Figure 5.22. This figure shows:

- (a) Left: Example of metal flakes found in bearing housing and recovered working fluid. Right: A section of the outer race of the seized bearing.
- (b) Expander bearing cap showing chemical attack of the nitrile butyl rubber (NBR) seal.

(a) (b)

Figure 5.22 – Examples of bearing failure.

The cause of the bearing failure is postulated to be various material incompatibilities with the M1 working fluid leading to a build-up of debris in the races. Both nitrile rubber and PTFE seals were affected by the fluid. PTFE thread tape (applied in the initial build of the system) was found to be blackened, and all nitrile rubber seals had swollen and showed signs of chemical attack.

An unidentified oily residue was also found to be coating the inside of the buffer tank, which obscured the optical level sensors, and in the refrigerant drained from the evaporator, shown in Figure 5.23. This figure shows:

- (a) optical working fluid level sensor obscured by grime debris which coated the inside of the buffer tank.
- (b) cleaned level sensor to highlight degree of fouling.
- (c) & (d) drained refrigerant from the evaporator showing fouled working fluid and floating debris. The fluid was clear and transparent when charged into the system.

This oily residue was possibly the bearing lubricant, as other sources of oil infiltration into the system (though compromised braising in the evaporator, or from the pump crank case) were ruled unlikely upon inspection. The nature of the black particulate matter was unconfirmed, a hypothesis is that it may be fine NBR circulated through the system.

This oil in the evaporator would likely be detrimental to system performance, leading to decreased heat transfer rates (Lemort et al., 2012), compounding the already roughly 50% decreased heat transfer rate of zeotropic working fluid compared to its pure fluid constituents (Weith et al., 2014).

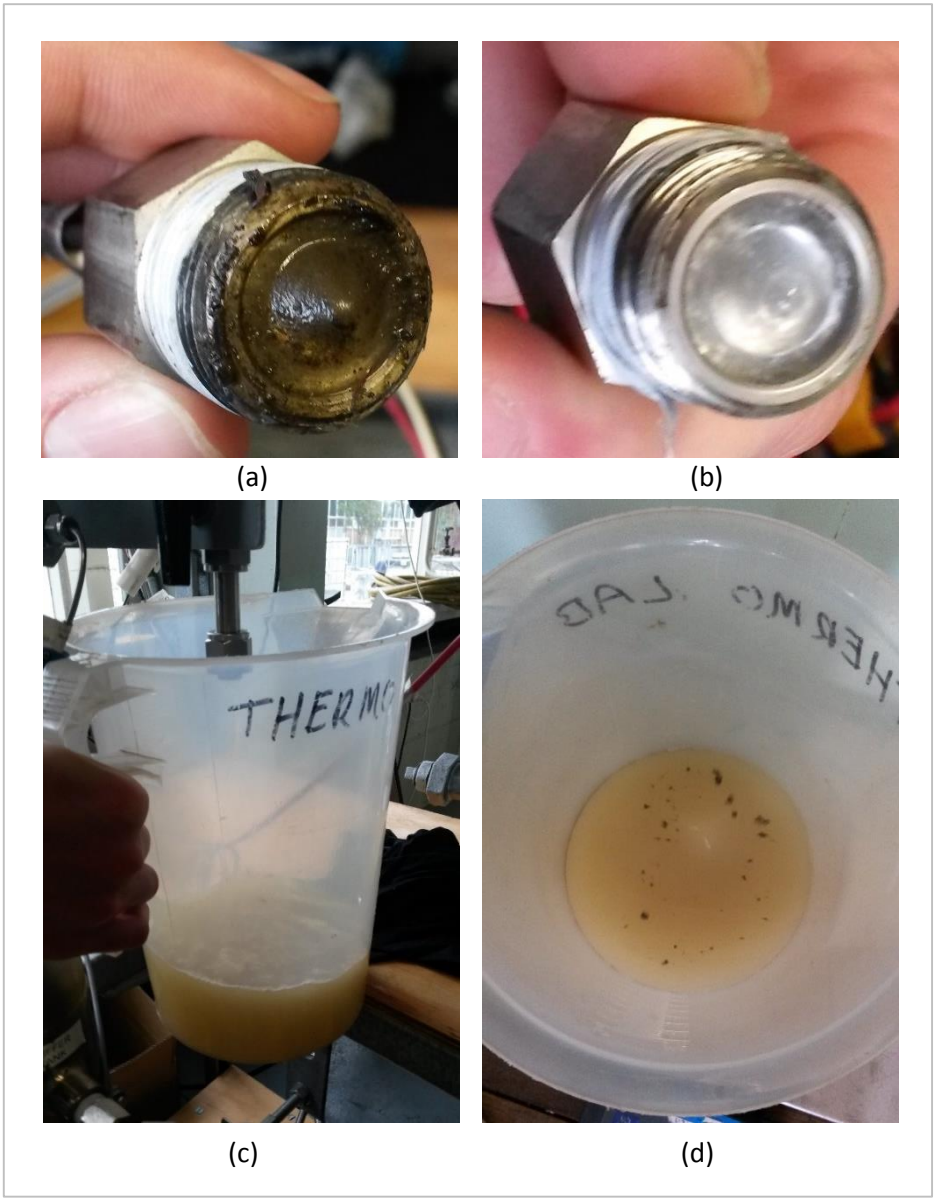

Figure 5.23 – Examples of fouling in ORC loop.

Debris was discovered in the piston assembly of the working fluid pump during the system teardown, shown in Figure 5.24. This appears to be nitrile rubber, however, this is unconfirmed. This may be due to the nitrile rubber seals expanding in the working fluid and their dynamic interaction causing wear.

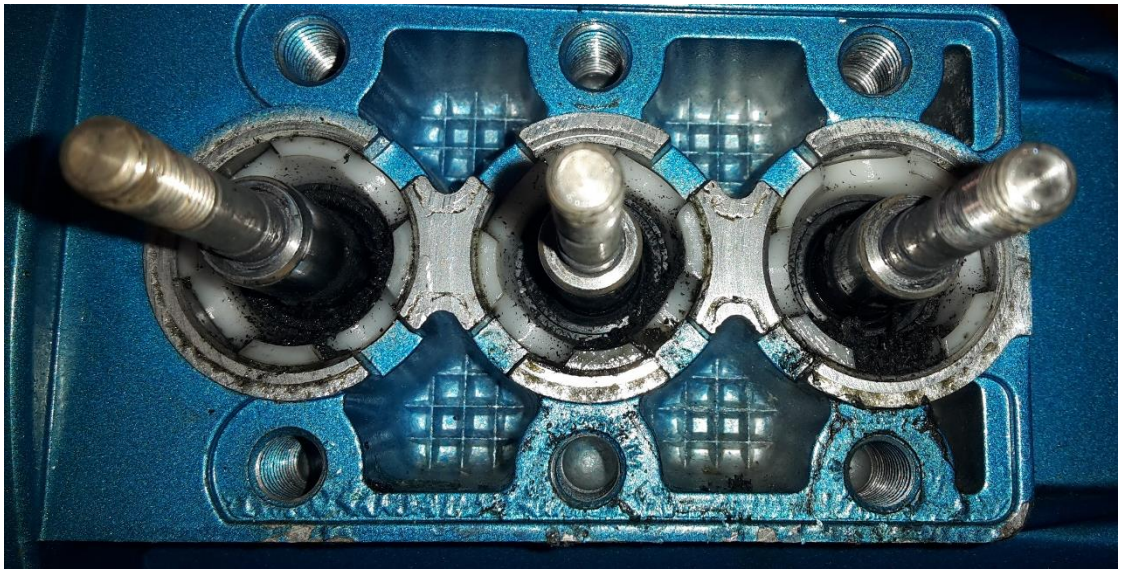

Figure 5.24 – Debris in the working fluid pump piston assembly.

A pinhole leak in the evaporator exit flange weld was identified during operation mid-way through the first set of tests. The system was initially charged with 9.26 ± 0.02 kg, with only 7.9 ± 0.05 kg recovered at the end of trials, meaning a substantial loss of 1.36 ± 0.07 kg (approximately 15% of initial charge). At the time, to continue testing, this was addressed using a wicking grade Loctite product with thermal stability up to 149 ^{o}C (Henkel Corporation, 2010). Initially this was successful, however, by the conclusion of the DVR tests it had reopened, with a loss of 1.05± 0.05 kg (approximately 25 % of the final calculated remaining mass in the system).

All these issues will have had an effect on system performance, and their time dependent nature introduces a large amount of uncertainty into any results obtained in the trials. The performance results can still be viewed to present trends of relationships between variables, but caution should be taken using values to infer future design decisions.

Chapter 6 Future development considerations

The following chapter details recommendations for any study utilizing the experimental system used in the current study for further testing. Recommendations are informed by critiques of components and the working fluid derived from experiences in operating the system, and examples of superior systems in the reviewed literature.

The future work covers the working fluid, heat transfer loop, ORC circuit componentry, sensory equipment, generator and electrical load, expander, working fluid flow meter, and working fluid pump.

6.1.1 Working fluid

The experiments in the current study were persistently undermined by the uncertainty associated with the selection of a mixture working fluid. It is therefore highly recommended that any future work uses a pure working fluid, preferably R245fa.

The unknown zeotropic fluid mixture behaviour in the system, both chemically and thermo-physically, is likely the cause of premature expander failure. The uncertainty greatly increases the difficulty of confidently identifying causes of issues encountered during testing, and confidence in the performance metrics which use REFPROP to calculate state properties. Operating the system with a pure working fluid would remove this uncertainty and provide a benchmark of system performance, after which the behaviour of zeotropic mixtures may be investigated.

The Australian branch of the refrigerant company A-Gas was initially contacted at the outset of the current study, and could theoretically supply R245fa. However, import restrictions and license issues meant this was not possible in the timeframe required to complete experiments before lab closure due to renovations. Future work may take this timeframe into account and procure the working fluid.

The current hypothesis for the oil residue in the working fluid loop is that it is bearing lubricant from the expander, as outlined in section 5.4. This should be confirmed before further testing is undertaken, by contacting the expander manufacturer to confirm the lubricant the bearings initially shipped with. If this is not the case, further test the evaporator and working fluid pump crank case for seal integrity, as these are the only other two sources of oil in the system.

The contaminated working fluid was recovered and stored for any future studies what wish to have a chemical analysis performed to aid residue identification. Similarly, the seized expander bearings have been recovered allowing further inspection.

6.1.1.1 Future testing of DVR

It is possible the current study began testing the effect of DVR on system performance at too low a ratio.

The maximum DVR tested in the system was 0.54, informed by a similar starting point by the authors in (Li et al., 2015) who tested the range of 0.51 – 0.32. In this range, the authors saw a clear effect of changing the DVR.

The size of components and physical layout dictate that the DVR is only a relative measure, specific to each system. Therefore, the starting DVR of the current study was also checked by an estimate of

66% full heat exchangers and 100% in fluid lines where liquid phase was expected. However, the current study neglected to take into account the volume of liquid holdup in the buffer tank. As a result, this starting value may have been insufficient to observe the effects of DVR. For this reason it is recommended future tests begin trials at a higher DVR. For example, a DVR of 0.61 would account for a 50% full buffer tank.

6.1.2 Heat transfer loop

6.1.2.1 Heat exchanger

The finned-tube heat exchanger design may require modification. The heat exchanger features distribution header tanks that cannot be fully purged of air when charging with thermal transfer fluid. This causes the thermal oil loop to experience higher pressures than a design that would allow for all air to be displaced.

Furthermore, the presence of oxygen in the loop may have contributed to the rust build up in the fluid which was discovered when the safety valve vented oil in initial testing.

In order to decrease heat loss, it may be beneficial to insulate the finned tube heat exchanger and Capstone exhaust pipe, for example with high temperature mineral wool.

6.1.2.2 Capstone mass flow rate

A method to approximate the Capstone exhaust mass flow rate may aid in assessing the efficacy of the finned-tube heat exchanger.

The current study uses manufacturer data to assume an exhaust mass flow rate at a given electrical power setting. This introduces an unknown degree of uncertainty, which would be removed by measurement of the exhaust mass flow rate. In the study detailing the design of the heat transfer loop (Engel, 2013), the author concluded that direct measurement of the exhaust mass flow rate was unfeasible due to the undeveloped flow conditions and lack of a reference mass flow rate for calibration. However, the authors in (Yang et al., 2013) demonstrate an effective and low-cost method of approximating the exhaust mass flow rate of their diesel engine, which may be adopted by future work as follows to remove this uncertainty:

- Measure the engine intake air flow rate, temperature, and pressure. The flow rate could be measured with simple vane anemometer (cup or windmill).
- Measure the flow rate and temperature of the diesel, again potentially with some form of rotary vane sensor in the piping.
- Assume conservation of mass to determine the exhaust mass flow rate.

6.1.2.3 Alternative heat source

Future tests may consider using an electrical heater to heat the oil instead of the Capstone turbine exhaust. The results of the current study provide enough data to suitably specify such a system. While this would present another capital cost, it would increase control over the heat source and eliminate the variables introduced by an exhaust heat extraction system. As a further benefit would be eliminating the need to consume diesel purely for the exhaust heat. The electric oil heater method is often used to great effect in the reviewed literature concerning performance testing of small ORC systems (Yang et al., 2017).

6.1.3 ORC circuit recommended modifications

The following issues identified during experimental testing should be address before any further testing is undertaken.

- Evaporator: The evaporator should be disconnected from the system and chemically cleaned to remove the oil residue discovered upon draining of the system. The top flange requires welding to fix the pinhole leak, and pressure testing to confirm integrity.
- Circuit componentry: Using the buffer tank as a test, isolate a method of chemically flushing the ORC loop and its componentry to remove the oily debris discovered on disassembly.
- Expansion tank modification: If future testing involves further inspection of the effects of DVR, consider installing a method to vary the working fluid charge in the system. This could be achieved through the method used by (Quoilin, 2007), who installed an expansion tank after the working fluid pump. The tank was suspended by a piezoelectric force transducer to deduce the mass of the working fluid, and the working fluid level controlled by a pressurized nitrogen source. A secondary advantage of this system is the reduction of variations of the refrigerant flow rate caused by the positive displacement action of the working fluid pump. This leads to more accurate measurement.

6.1.4 Sensory equipment

The experimental system was hampered by inadequate sensory equipment in some areas. These are identified in this section along with recommendations for improvement.

6.1.4.1 Torque measurement

For the reasons outlined in section 5.1.7, using the measured electrical power produced by the generator to deduce the expander power introduces too much uncertainty. Torque should be directly measured, and used in conjunction with shaft speed measurement to determine power, which is common practise in the reviewed literature. This can be achieved by a rotating torque sensor, either directly in-line between the expander and generator, or belt-driven which allows a smaller system footprint. The former method has the advantage of avoiding belt friction losses. It may also be worth considering measuring torque and shaft speed of the working fluid pump as done in (Woodland et al., 2012). This would allow future work to better inspect the efficiency of the pump, which should give insight into system optimisation possibilities.

6.1.4.2 Power measurement

To avoid the necessity for the empirical power relationships detailed in sections 5.1.1 and 5.1.2, and the unknown uncertainties they introduce, it would be advisable to install dedicated power sensors to measure the generator electrical output, working fluid pump, and thermal oil pump. Examples include the Watt transducers used by (Muhammad et al., 2015). These should be directly integrated into the LabVIEW data acquisition program. Additionally, this will cut down on time spent manually transferring power data from the proprietary clamp meter program into the LabVIEW data, and thereby reducing the risk of introducing time-matching errors, which is inherent in this process.

6.1.4.3 Working fluid flow rate

Manual reading and entry of the working fluid flow rate was the largest source of equipment uncertainty in the current study. A digitally integrated solution should be implemented, either by purchasing the relevant kit for the current meter or a Coriolis meter, detailed in section 6.1.7.

6.1.4.4 Load integration

Manual entry of the electric load into the LabVIEW program resulted in several data entry mistakes which led to confusion and loss of useful data. The load should be controlled through LabVIEW, either by binary switching of the light bulbs or selecting resistances as detailed in section 6.1.5.

6.1.4.5 Condenser fluid flow rate

The rotary vane flow meter used for measuring the flow rate of water in the condenser had a faulty connection and the data had to be discarded. This requires rewiring of the connection, and the output checked in LabVIEW by comparing the result to an experimental flow measurement.

6.1.5 Generator and electrical load

The generator used by the current study is unfit for purpose for the reasons outlined in section 5.1.7. With electrical generated power being a crucial metric of the system, an alternative should be sourced. A permanent magnet generator would be preferable such as a three phase permanent magnet generator as used by the authors in (Yang et al., 2017). Another possibility is to use a servo motor with digital control, as used by (Bamorovat Abadi et al., 2015).

Light bulbs are likely not an appropriate method of imposing an electrical load on the system. Their resistance is dependent on their temperature, and there is not enough selection to accurately impose a load to control the expander rotational speed. A preferable alternative would be a cooled resistor bank such as that used by the authors in (Bamorovat Abadi et al., 2015). In conjunction with integrated LabVIEW control, this would allow control over the rotational speed of the expander to evaluate its performance at different speeds.

6.1.6 Expander

With the expander inoperable, a new expander would have to be procured for further testing. The current unit may be able to be refurbished by Air Squared. If this is not feasible, a new expander of the same model could be purchased. If this is the case, it is strongly recommended to only use pure R245fa as a working fluid or consult Air Squared for alternatives. Alternatively, a scroll compressor could be modified to run in reverse, which has shown to be an effective method in literature (Lemort et al., 2012). However, it should be noted this increases system complexity with the need for lubrication.

During experiments, all hot components were insulated to prevent heat loss, except for the expander. The expander design features what appears to be heat dissipating fins (Figure 6.1). This may have been an oversight, with the two factors contributing to heat loss in the system. Future testing could experiment with insulating the expander, though it would be advisable to contact the manufacturer for an opinion on whether any resulting heat expansion of the materials might compromise the unit.

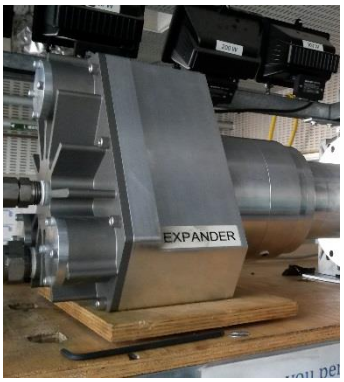

Figure 6.1 – Air Squared 1 kW expander used in experiments.

6.1.7 Working fluid volume flow meter

Working fluid flow rate is a critical measurement for investigating system performance. In the current study, manual reading and entry of the working fluid flow rate was the largest source of measurement uncertainty, and considerably higher than that reported in similar published studies.

As a result of an incorrect specification by a previous team, the variable area flow meter had a poorly suited resolution for its analogue reading, shown in Figure 6.2. The scale starts at 0.95 L/min, with only half a division between that and the next increment at 2.00, then normal divisions up to 9.50. With the maximum flow rate achieved by the fluid pump being 2.5 L/min, this made reading the flow meter difficult. Furthermore, at lower frequencies the pressure pulses inherent in a positive displacement pump became more prevalent, causing further difficulty in reading. This led to a large uncertainty in addition to the measurement accuracy uncertainty.

The poorly suited resolution inherently limited the measurement accuracy. The operating principle results in a constant relative error above 50% of the measurement scale, while below this limit the relative error increases in an inversely proportional relationship (KROHNE), shown in Figure 6.3. As the maximum flow rate was approximately 30% of the measurement scale, measurement error was always greater than 2.6%.

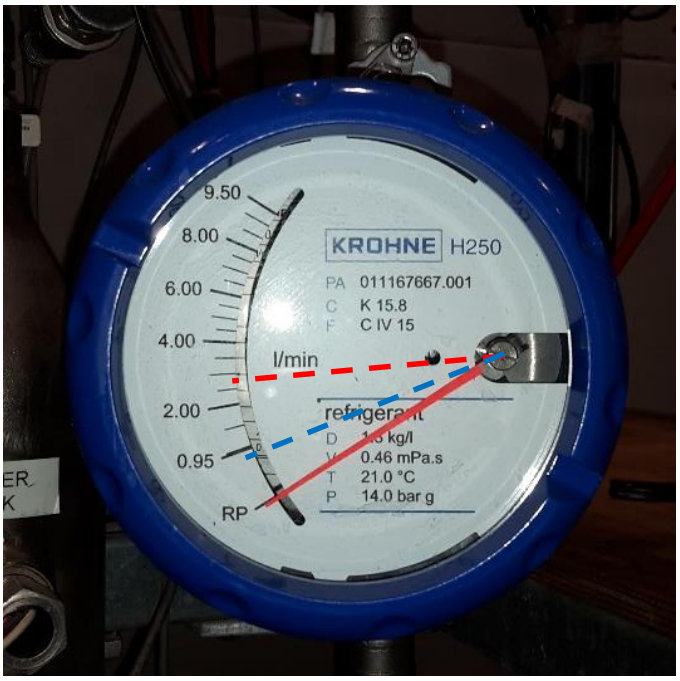

Figure 6.2 – Demonstration of the range of recorded working fluid flow rates during experimental trials with minimum in blue and maximum in red.

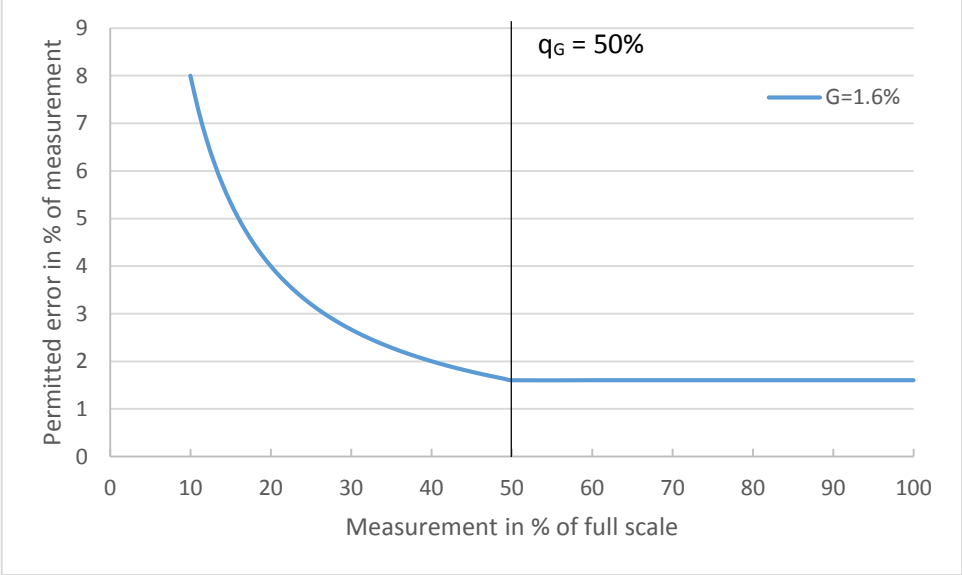

Figure 6.3 – Permissible error as a function of the measurement in % of the full scale. Data from manufacturer (KROHNE).

For these reasons it is recommended the working fluid flow meter be reviewed before further testing is conducted. Possible solutions include:

- Request a quote from KROHNE for cost of re-calibrating the meter to a more appropriate scale.
- Purchase the electronic integration package available from KROHNE, which would allow digital measurement in the LabVIEW software. Coupling this with a high sample rate and some form of averaging would minimise the impact of the pulsation at lower frequencies for more accurate measurement.

- Purchase an appropriately sized Coriolis flow meter. This would produce the most accurate measurement, and is commonly used in experimental small-scale ORC systems (Declaye et al., 2013) (Muhammad et al., 2015).

6.1.8 Working fluid pump

- The seals in the working fluid pump require addressing. They may require replacement, either with another nitrile rubber set or possibly a PTFE set. The latter theoretically should be more chemically stable. These were previously implemented in an earlier iteration of the experimental system and reportedly disintegrated, attributed to chemical attack (Southon, 2014). However, this may have been due to operator error by running the pump dry without working fluid, as opposed to chemical incompatibility. This reportedly happened on several occasions in the previous study. Depending on cost and availability, it may be advisable to purchase both types of seals simultaneously and experimentally confirm the previous study's findings.
- If future work includes a complete redesign of the ORC loop, consider the applicability of a gear pump as the working fluid pump. This would still satisfy the high-pressure, low flow-rate requirement, while producing less of a pressure spike than a plunger pump, making flow rate measurement easier. (Muhammad et al., 2015) successfully operated such a pump in a very similar experimental setup to the current study, however, no comment was made on its efficiency.

Chapter 7 Conclusion

In the present study, an experimental 1 kW ORC was thoroughly investigated. The system was intended as a demonstration unit to understand the impacts of different inputs on system behaviour. These lessons could then be applied to scale-up systems in future work.

The study set out with the aim of investigating the performance of the ORC. Of particular interest was the efficacy of a zeotropic refrigerant mixture as a working fluid, and the impact on performance of the working fluid liquid level in the heat exchangers. In order to assess the latter, the study utilizes the concept of Dimensionless Volume Ratio (DVR), as proposed by Li et al. (Li et al., 2015).

Prior to experimentation, the study addressed the measurement equipment on the system. Existing pressure sensors were recalibrated, as these were found to be incorrectly calibrated by previous system fabricators. A digital pressure sensor was added to the heat transfer oil loop to allow quick monitoring and improve safety.

The cycle was thermodynamically simulated with a MATLAB 2016b, using NIST REFPROP 9.0 as a fluid property reference library. A theoretical performance point based on informed input parameters provided a benchmark to compare with experimental results. The theoretical net electrical work and cycle efficiency were 1.34 kW and 8.01% respectively.

Due to expander failure during experimental trials, the test methodology was revised, resulting in two sets of results. In the first set of experiments, the system inputs are independently varied to inspect system performance over its entire operating range. In the second set of experiments, in order to simulate the expander in its absence, a needle valve in the bypass line was used to produce a pressure drop to investigate maximum performance at each DVR.
Analysis of the results from the first tests showed the system performed poorly compared to design estimates and similar published studies by other authors. The expander had a maximum isentropic efficiency of 42.9%, while consistently high filling factors with a minimum filling factor of 1.61 suggested possible internal leakage. Published studies using the same expander unit reported isentropic efficiencies from 70 to 77%.

The maximum electrical power output was 598 W, which limited cycle net efficiency to a maximum of 3.56%. This is approximately half of that achieved by comparable studies and of a reasonable theoretical estimate at the operating conditions. Similarly, second law efficiency was the lowest among the compared published work with a maximum of 11.8%. The working fluid pump had a maximum isentropic efficiency of 19.11%. A working fluid flow rate analysis showed the theoretical volumetric displacement method, used by a previous study on this system, consistently overestimated flow rate by upwards of 30%. This highlighted the necessity for direct fluid flow measurement as implemented in the present study.

Analysis of the results from the second tests suggest the working fluid charge in the system influences operation, as shown by the authors in (Li et al., 2015). Although the influence of the DVR on maximum achievable pressure ratio was inconclusive, decreasing the DVR reduced the maximum achievable mass flow rate at each of the input heat source settings. Decreasing the DVR resulted in a monotonically decreasing heat absorption efficiency, demonstrating the reduced ability of the

system to utilize the available heat stream. Decreasing the DVR also reduced the degree of subcooling in the condenser. These initial results support the need for further testing the effect of the DVR in a fully functioning system.

The heat transfer loop performed adequately, extracting 10 - 25 kW from the exhaust stream. Decreasing heat absorption efficiency at higher Capstone power settings suggested the heat exchanger may benefit from redesign to better capture heat at higher exhaust flow rates.

The experiments were hampered by a host of problems. Heat balances on the evaporator and condenser showed a significant disparity between calculated and experimental heat transfer rates. This cast uncertainty on the measurements, and raised questions surrounding the behaviour of the zeotropic refrigerant mixture and its handling by REFPROP. This behaviour in REFPROP may also explain the persistently high expander filling factors, with REFPROP underestimating the fluid density at the expander inlet.

Additionally, the system experienced loss of refrigerant in both sets of experiments, through a pinhole leak in the evaporator flange weld. Attempts to fix this during tests were unsuccessful, losing approximately 15% of the charged refrigerant in both tests. The working fluid flow meter, installed in a previous iteration of the project, was ill suited for the application due to its dynamic scale range, resulting in large experimental uncertainties.

Following the conclusion of experiments, the system was disassembled. It was found that the expander bearings had seized, and its internals coated with an unknown residue which also was present downstream in the system. The current hypothesis is this was bearing lubricant, as other oil sources appeared isolated. This is possibly caused by a chemical incompatibility with the selected zeotropic working fluid, as the expander is designed to operate with pure R245fa.

Informed by the various shortcomings of the system experienced during testing, the current study presents suggestions for future operation. It is most strongly recommended to use a pure working fluid such as R245fa, and improve the sensory equipment of the experimental rig. In particular, replacement of the working fluid flow rate sensor and installation of torque measurement to measure expander power, as well as replacing the generator and banks of lights as resistive load with a more suitable solution.

It would be beneficial to further test the influence of the DVR on system performance, with a revised experimental setup. With this knowledge, the foundations to scale-up to larger under 50 kW ORC units and their effective testing methodology can be investigated. Critiques of components and working fluid, derived from experiences in operating the system, coupled with general trends produced by the results, provide useful consideration for the design of future small-scale ORC systems.

Bibliography

AIR SQUARED MANUFACTURING INC. 2015. E15H22N4.25 1 kW Scroll Expander. R4 ed.

ASIMPTOTE. 2016. *Cycle-Tempo* [Online]. Available: http://www.asimptote.nl/software/cycle-tempo/ [Accessed 15/07/2016.

BAMOROVAT ABADI, G., YUN, E. & KIM, K. C. 2015. Experimental study of a 1 kw organic Rankine cycle with a zeotropic mixture of R245fa/R134a. *Energy,* 93, Part 2**,** 2363-2373.

BAO, J. & ZHAO, L. 2013. A review of working fluid and expander selections for organic Rankine cycle. *Renewable and Sustainable Energy Reviews,* 24**,** 325-342.

BARAL, S., KIM, D., YUN, E. & KIM, K. 2015. Energy, Exergy and Performance Analysis of Small-Scale Organic Rankine Cycle Systems for Electrical Power Generation Applicable in Rural Areas of Developing Countries. *Energies,* 8**,** 684.

BRACCO, R., CLEMENTE, S., MICHELI, D. & REINI, M. 2013. Experimental tests and modelization of a domestic-scale ORC (Organic Rankine Cycle). *Energy,* 58**,** 107-116.

BUDISULISTYO, D., SOUTHON, M. & KRUMDIECK, S. The Effect of Heat Exchanger Design on the Return on Investment of a Geothermal Power Plant. Proceedings 36th New Zealand Geothermal Workshop, 2014. 26.

CAPSTONE, T. C. 2006. Technical Reference Capstone Model C30.

CHYS, M., VAN DEN BROEK, M., VANSLAMBROUCK, B. & DE PAEPE, M. 2012. Potential of zeotropic mixtures as working fluids in organic Rankine cycles. *Energy,* 44**,** 623-632.

DECLAYE, S., QUOILIN, S., GUILLAUME, L. & LEMORT, V. 2013. Experimental study on an open-drive scroll expander integrated into an ORC (Organic Rankine Cycle) system with R245fa as working fluid. *Energy,* 55**,** 173-183.

DESIDERI, A., HERNANDEZ, A., GUSEV, S., VAN DEN BROEK, M., LEMORT, V. & QUOILIN, S. 2016. Steady-state and dynamic validation of a small-scale waste heat recovery system using the ThermoCycle Modelica library. *Energy,* 115, Part 1**,** 684-696.

DONALD L. SIMON, J. S. L. 2010. A Data Filter for Identifying Steady-State Operating Points in Engine Flight Data for Condition Monitoring Applications. NASA/TM: Glenn Research Center, Cleveland, Ohio.

DONG, B., XU, G., LUO, X., ZHUANG, L. & QUAN, Y. 2017. Potential of Low Temperature Organic Rankine Cycle with Zeotropic Mixtures as Working Fluid. *Energy Procedia,* 105**,** 1489-1494.

EICKE, A. & SMOLEN, S. 2015. ORC-DEMONSTRATION-PLANT WITH 1 KW SCROLL EXPANDER– CONCEPT, DESIGN AND OPERATIONAL EXPERIENCES.

ENGEL, F. 2013. *Experimental Investigation and Derived Considerations for the Scale-Up of a Finned-Tube Heat Exchanger for Exhaust Gas Heat Recovery.* MSc Master's Thesis, Hamburg University of Technology.

EYERER, S., WIELAND, C., VANDERSICKEL, A. & SPLIETHOFF, H. 2016. Experimental study of an ORC (Organic Rankine Cycle) and analysis of R1233zd-E as a drop-in replacement for R245fa for low temperature heat utilization. *Energy,* 103**,** 660-671.

FELDHUSEN, K.-H. G. J. 2007. Dubbel: Taschenbuch für den Maschinenbau. Springer.

GALINDO, J., RUIZ, S., DOLZ, V., ROYO-PASCUAL, L., HALLER, R., NICOLAS, B. & GLAVATSKAYA, Y. 2015. Experimental and thermodynamic analysis of a bottoming Organic Rankine Cycle (ORC) of gasoline engine using swash-plate expander. *Energy Conversion and Management,* 103**,** 519-532.

GALLONI, E., FONTANA, G. & STACCONE, S. 2015. Design and experimental analysis of a mini ORC (organic Rankine cycle) power plant based on R245fa working fluid. *Energy,* 90**,** 768-775.

GUANGBIN, L., YUANYANG, Z., LIANSHENG, L. & PENGCHENG, S. 2010. Simulation and experiment research on wide ranging working process of scroll expander driven by compressed air. *Applied Thermal Engineering,* 30**,** 2073-2079.

HENKEL CORPORATION 2010. Loctite Threadlocker Green 290 Technical Data Sheet.

HONEYWELL, I. I. 2012. Enovate® 245fa Technical Brochure.

HUNG, T. C., WANG, S. K., KUO, C. H., PEI, B. S. & TSAI, K. F. 2010. A study of organic working fluids on system efficiency of an ORC using low-grade energy sources. *Energy,* 35**,** 1403-1411.

JUNG, H.-C., TAYLOR, L. & KRUMDIECK, S. 2015. An experimental and modelling study of a 1 kW organic Rankine cycle unit with mixture working fluid. *Energy,* 81**,** 601-614.

KROHNE. *Accuracy of variable area flowmeters* [Online]. Available: https://krohne.com/en/products/flow-measurement/variable-area-flowmeters/measuring-principle/ [Accessed 06 July 2017].

LAKEW, A. A. & BOLLAND, O. 2010. Working fluids for low-temperature heat source. *Applied Thermal Engineering,* 30**,** 1262-1268.

LEMMENS, J. J. M., OVERDIEP, J. J., BOS, K. H. & BARTHOLOMEUS, P. M. G. 2006. DEMONSTRATION OF CAPSTONE MICROTURBINES INCLUDING HIGH EFFICIENCY HEAT EXCHANGER, GAS SAFEGUARD MODULE AND NATURAL GAS COMPRESSOR, DEVELOPED BY GASUNIE ENGINEERING & TECHNOLOGY. *23rd World Gas Conference.* Amsterdam.

LEMMON, E. W., MCLINDEN, M.O., HUBER, M.L. 2013. REFPROP-Reference Fluid Thermodynamic and Transport Properties. 9.0 ed.: NIST NSRDS.

LEMMON, E. W. & SPAN, R. 2006. Short Fundamental Equations of State for 20 Industrial Fluids. *Journal of Chemical & Engineering Data,* 51**,** 785-850.

LEMORT, V., DECLAYE, S. & QUOILIN, S. 2012. Experimental characterization of a hermetic scroll expander for use in a micro-scale Rankine cycle. *Proceedings of the Institution of Mechanical Engineers, Part A: Journal of Power and Energy,* 226**,** 126-136.

LEMORT, V., QUOILIN, S., CUEVAS, C. & LEBRUN, J. 2009. Testing and modeling a scroll expander integrated into an Organic Rankine Cycle. *Applied Thermal Engineering,* 29**,** 3094-3102.

LI, T., ZHU, J., FU, W. & HU, K. 2015. Experimental comparison of R245fa and R245fa/R601a for organic Rankine cycle using scroll expander. *International Journal of Energy Research,* 39**,** 202-214.

LIU, Q., DUAN, Y. & YANG, Z. 2014. Effect of condensation temperature glide on the performance of organic Rankine cycles with zeotropic mixture working fluids. *Applied Energy,* 115**,** 394-404.

MA, Z., BAO, H. & ROSKILLY, T. 2016. *Dynamic modelling and experimental validation of scroll expander for small-scale power generation system*.

MAGO, P. J., CHAMRA, L. M. & SOMAYAJI, C. 2007. Performance analysis of different working fluids for use in organic Rankine cycles. *Proceedings of the Institution of Mechanical Engineers, Part A: Journal of Power and Energy,* 221**,** 255-263.

MEYER, D., CHOON WONG, FRITHJOF ENGEL & KRUMDIECK, S. 2013. Design and build of a 1 kW organic rankine cycle power generator *35th New Zealand Geothermal Workshop.* Rotorua, New Zealand.

MOHANRAJ, M., MURALEEDHARAN, C. & JAYARAJ, S. 2011. A review on recent developments in new refrigerant mixtures for vapour compression-based refrigeration, air-conditioning and heat pump units. *International Journal of Energy Research,* 35**,** 647-669.

MUHAMMAD, U., IMRAN, M., LEE, D. H. & PARK, B. S. 2015. Design and experimental investigation of a 1 kW organic Rankine cycle system using R245fa as working fluid for low-grade waste heat recovery from steam. *Energy Conversion and Management,* 103**,** 1089-1100.

PADLECKAS, H. 2009. *Temperature-Composition diagram of a zeotropic mixture* [Online]. Available: https://en.wikipedia.org/wiki/Zeotropic_mixture#/media/File:Binary_Boiling_Point_Diagram_new.svg [Accessed 11 October 2017].

PERIS, B., NAVARRO-ESBRÍ, J., MOLÉS, F., COLLADO, R. & MOTA-BABILONI, A. 2015a. Performance evaluation of an Organic Rankine Cycle (ORC) for power applications from low grade heat sources. *Applied Thermal Engineering,* 75**,** 763-769.

PERIS, B., NAVARRO-ESBRÍ, J., MOLÉS, F., GONZÁLEZ, M. & MOTA-BABILONI, A. 2015b. Experimental characterization of an ORC (organic Rankine cycle) for power and CHP (combined heat and power) applications from low grade heat sources. *Energy,* 82**,** 269-276.

PERIS, B., NAVARRO-ESBRÍ, J., MOLÉS, F. & MOTA-BABILONI, A. 2015c. Experimental study of an ORC (organic Rankine cycle) for low grade waste heat recovery in a ceramic industry. *Energy,* 85**,** 534-542.

QIU, G., LIU, H. & RIFFAT, S. 2011. Expanders for micro-CHP systems with organic Rankine cycle. *Applied Thermal Engineering,* 31**,** 3301-3307.

QUOILIN, S. 2007. *Experimental Study and Modeling of a Low Temperature Rankine Cycle for Small Scale Cogeneration.* Electro-Mechanical Engineeer, University of Liege.

QUOILIN, S., AUMANN, R., GRILL, A., SCHUSTER, A., LEMORT, V. & SPLIETHOFF, H. 2011. Dynamic modeling and optimal control strategy of waste heat recovery Organic Rankine Cycles. *Applied Energy,* 88**,** 2183-2190.

QUOILIN, S., DECLAYE, S., LEGROS, A., GUILLAUME, L. & LEMORT, V. Working fluid selection and operating maps for Organic Rankine Cycle expansion machines. Proceedings of the 21st international compressor conference at Purdue, 2012. 10.

SHU, G., ZHAO, M., TIAN, H., WEI, H., LIANG, X., HUO, Y. & ZHU, W. 2016. Experimental investigation on thermal OS/ORC (Oil Storage/Organic Rankine Cycle) system for waste heat recovery from diesel engine. *Energy,* 107**,** 693-706.

SOLVAY 2010. Solkane® 365mfc Technical Information.

SOUTHON, M., KRUMDIECK, SUSAN. Commissioning, Initial Testing and Results From an Experimental One Kilowatt Organic Rankine Cycle. Proceedings 36th New Zealand Geothermal Workshop, 2014. 26.

U.S. DEPARTMENT OF ENERGY 2008. Improving motor and drive system performance: A sourcebook for industry. .

WANCO 2011. Owner's Manual - Voltmaster Two-Bearing Belt-Drive Generators.

WANG, J. L., ZHAO, L. & WANG, X. D. 2010. A comparative study of pure and zeotropic mixtures in low-temperature solar Rankine cycle. *Applied Energy,* 87**,** 3366-3373.

WANG, X. D. & ZHAO, L. 2009. Analysis of zeotropic mixtures used in low-temperature solar Rankine cycles for power generation. *Solar Energy,* 83**,** 605-613.

WEITH, T., HEBERLE, F., PREIßINGER, M. & BRÜGGEMANN, D. 2014. Performance of siloxane mixtures in a high-temperature Organic Rankine Cycle considering the heat transfer characteristics during evaporation. *Energies,* 7**,** 5548-5565.

WINANDY, E., O, C. S. & LEBRUN, J. 2002. Experimental analysis and simplified modelling of a hermetic scroll refrigeration compressor. *Applied Thermal Engineering,* 22**,** 107-120.

WOODLAND, B. J., BRAUN, J. E., GROLL, E. A. & HORTON, W. T. 2012. Experimental testing of an organic Rankine cycle with scroll-type expander.

YANG, K., ZHANG, H., WANG, Z., ZHANG, J., YANG, F., WANG, E. & YAO, B. 2013. Study of zeotropic mixtures of ORC (organic Rankine cycle) under engine various operating conditions. *Energy,* 58**,** 494-510.

YANG, S.-C., HUNG, T.-C., FENG, Y.-Q., WU, C.-J., WONG, K.-W. & HUANG, K.-C. 2017. Experimental investigation on a 3 kW organic Rankine cycle for low-grade waste heat under different operation parameters. *Applied Thermal Engineering,* 113**,** 756-764.

YU, G., SHU, G., TIAN, H., WEI, H. & LIU, L. 2013. Simulation and thermodynamic analysis of a bottoming Organic Rankine Cycle (ORC) of diesel engine (DE). *Energy,* 51**,** 281-290.

ZHAI, H., AN, Q., SHI, L., LEMORT, V. & QUOILIN, S. 2016. Categorization and analysis of heat sources for organic Rankine cycle systems. *Renewable and Sustainable Energy Reviews,* 64**,** 790-805.

Appendices

Appendix A Glossary

Abbreviation / term	**Description**
Capstone	Company manufacturing micro-turbine generators powered by either gas or diesel.
CSP	Concentrating Solar Power
DVR	Dimensionless Volume Ratio - ratio of the volume of the liquid working fluid charged into the system V_{wf} to the total internal volume of the working fluid circuit V_{sys}
Expander	Machine used to extract work from the pressurised fluid in a Rankine cycle
NBR	Nitrile-butyl rubber
ORC	Organic Rankine Cycle
PTFE	Polytetrafluoroethylene, commonly referred to as Teflon
Zeotropic	A mixture of two or more component fluids with different boiling points

Appendix B Heat transfer fluid manufacturer data

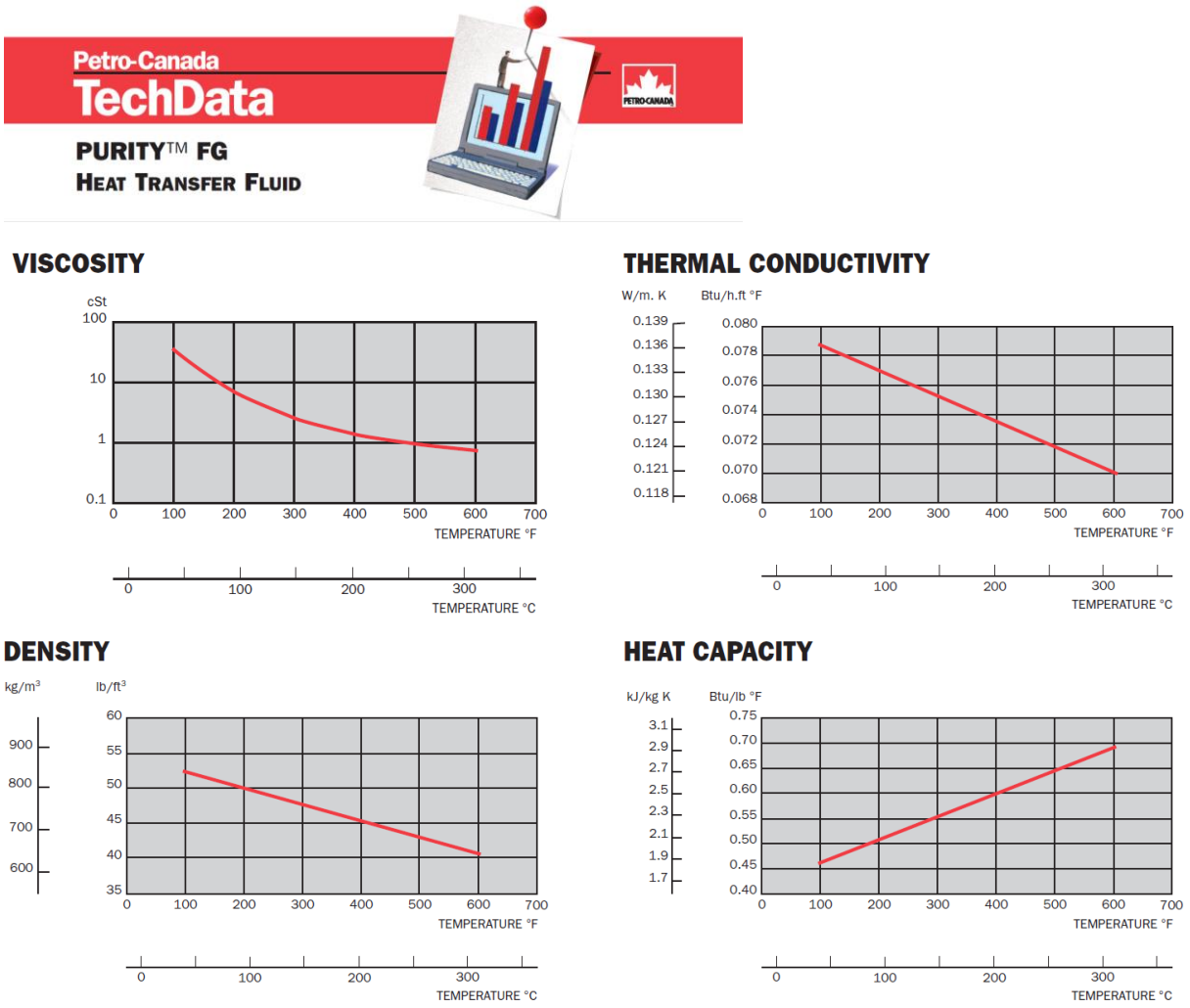

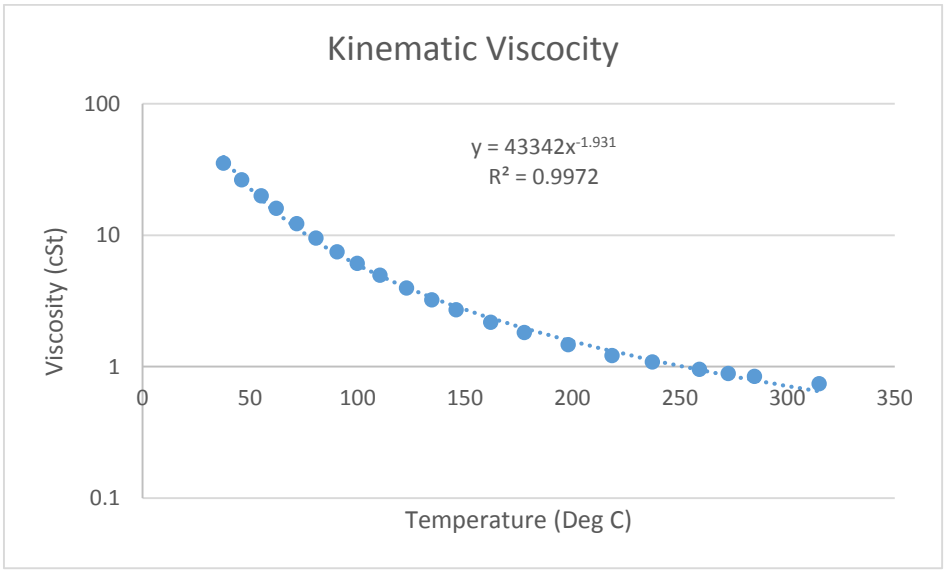

Figure 7.1 – Resulting equation for kinematic viscosity using Engauge Digitizer software on manufacturer data

Appendix C M1 working fluid certificate of analysis

A-GAS™

A-Gas (Australia) Pty Limited
9-11 Oxford Road
Laverton North, VIC, 3026
Australia

Tel [+61] (0) 3 9368 9222
Fax [+61] (0) 3 9368 9233

email info.au@agas.com
www.agas.com

GAS

Speciality Chemicals and Gases

Certificate Of Analysis

Product	Foaming Agent M1	Batch No.	FAM1241011	Report No.	CA000436

Test	Limits (Wt %)	Result (Wt %)
245fa (Enovate 3000)	45 - 55	50.3
365mfc	45 - 55	49.7

Tests Conducted By: _____ *Date: _26_ / _10_ / _11_*

Authorising signature: _____ *Date: _26_ / _10_ / _11_*

Appendix D Experiment details

The following presents the observations and chronology of the experiments carried out in this study.

D.1 May 2015 tests

Test dates: 25, 26

Details:

- Charged with 9.26 ± 0.02 kg of M1.
- First run of system to confirm working order, attempting low energy points over two days.
- Testing ended by refrigerant leak identification at the exhaust of the evaporator Swagelok fitting. Identified the presence of oil in the refrigerant loop.

D.2 June 2015 tests

Test dates: 29, 30

Details:

- Aim of tests was to find highest operating point of the system, observing which of the system limits was reached first. Oil pressure in the transfer loop was not actively monitored, as previous group documentation had calculated that other system limits would be reached well before the oil pressure limit. Furthermore, the pressure required a manual reading on the other side of the equipment making it hard to monitor while observing the main system sensors.
- On 30 June, the oil safety valve was triggered and vented oil into lab.
- Documentation stated the oil safety valve was set for 5 bar, subsequent dead load testing showed failure pressure of 4.2 bar. This could possibly be due to vibrations shaking the seat of the valve loose, or simply previous fabricator error. The safety valve was reset to 5 bar and reinstalled.
- There was fine rust fouling in the vented thermal oil, which may have been detrimental to heat transfer, and possibly impair the oil pump through abrasion. Previous work (Meyer et al., 2013) warned this may happen as there was no way to galvanically isolate the ORC from the steel thermal oil loop.
- New oil was sourced, and a digital pressure transducer installed in the oil loop allowing monitoring from main console.
- The tests indicated the ORC system itself could handle up to 25 kW setting on Capstone, with system parameters all below their limits.

D.3 August 2015 tests

Test dates: 11, 13, 17, 18, 19, 20, 21, 24, 25, 26, 27, 28, 31

Details:

- System performance mapping tests as described in section 4.4.3.
- Tests ended due to expander bearing failure on the 1st September.

- Decommissioning system drained 7.90 ± 0.02 kg of fluid, meaning a fluid loss of 1.37 ± 0.04 kg over the course of the experiments from May (14.8% of the initial charge).
- The drained fluid had significant fouling and transported metal flakes, as detailed in section 5.4.

D.4 Sept-Oct 2015 tests

Dates: 17, 23, 29, 30 September; 1, 4 October

Details:

- DVR tests as described in section 4.4.4.
- While decommissioned, optical sensors in buffer tank were found to be coated in a residue which was impairing their function. Sensors were cleaned and reinstalled.
- During fluid charging procedure, a pinhole leak was discovered in the flange weld on the evaporator outlet.
- Attempted in situ fix of the weld by applying wicking grade 290 Loctite, as there was no time in the test schedule for disassembly and re-doing the weld, due to scheduled lab closure.
- Used vacuum pump to create slight vacuum in system to draw in Loctite. The seal was pressure tested to 13 bar successfully.
- The Loctite compound has a maximum service temperature of 149 °C (Henkel Corporation, 2010).Staying below this temperature from this point was necessary for best chance of maintaining system integrity over DVR tests.
- System was charged with 7.94 ± 0.02 kg of fluid.
- Fluid was drained from exit of pump in 4 steps, with 4.30 kg± 0.02 kg of fluid calculated to be remaining before final decommission.
- The final fluid drain recovered 3.25 ± 0.02 kg, a loss of 1.05 ± 0.04 kg, with the evaporator flange pinhole leak having reopened during testing.

D.5 May 2016 Teardown

Dates: 20, 23

Details:

- Series of investigative tests to inspect leakage of the system and cause of scroll failure.
- Dismantling and documenting scroll expander, pump assembly, and ball valves.
- While pump seals showed signs of chemical attack, pressure testing showed there was no leakage from the pump assembly.

Appendix E Experimental equipment disassembly photos

This appendix presents the remainder of photos and explanations from the system disassembly, in an extension to section 5.4.

Figure 7.2 – Thermal oil spill.

Figure 7.2 shows the thermal transfer oil venting from the safety valve, which occurred when the pressure threshold was exceeded in preliminary trials. The oil was originally a transparent yellow, the brown discolouration was rust, indicating there is rust in the heat transfer loop. This may change the thermal oil properties, and possibly the plate heat exchanger efficacy.

Figure 7.3 – Scroll expander bearing cap.

Figure 7.3 shows the brown oily residue which built up in the expander bearing caps, and was distributed throughout the internals of the expander. The black flakes are the NBR O-ring seals which are being chemically degraded by the working fluid.

(a)

(b)

Figure 7.4 – Expander scrolls.

Figure 7.4 (a) shows a chip in the scroll face seal. This may have been caused by disassembly, however, as great care was taken this is unlikely. This may have interfered with the scroll face seal integrity and contributed to internal leakage. Figure 7.4 (b) shows evidence of the residue having hardened and possibly adding resistance to the scrolls orbital motion.

Figure 7.5 – Residue build-up.

Figure 7.5 shows the debris collected in the rear shroud of the scroll expander that covers the permanent magnet used for the magnetic coupling. The pattern suggests the debris was spun at some velocity.

Figure 7.6 – Seized rear shaft bearing.

Figure 7.6 shows the debris build-up in the rear shaft bearing, which caused it to seize. Figure 7.7, over page, demonstrates how the shaft was rotating on the inner race of the bearing. This caused the excessive noise experienced during testing which indicated the expander failure. The shaft showed signs of wear in this area shown in Figure 7.8, over page.

Figure 7.7 – Demonstration of shaft rotating on the inner race of the bearing.

Figure 7.8 – Shaft of the scroll expander.

Figure 7.9 – Rear bearing and its subsequent dissection.

Figure 7.9 shows, from left to right, the limited degree of movement left in the bearing, the debris build-up on the balls of the bearing, and on the outer race.

Figure 7.10 – Working fluid pump piston assembly.

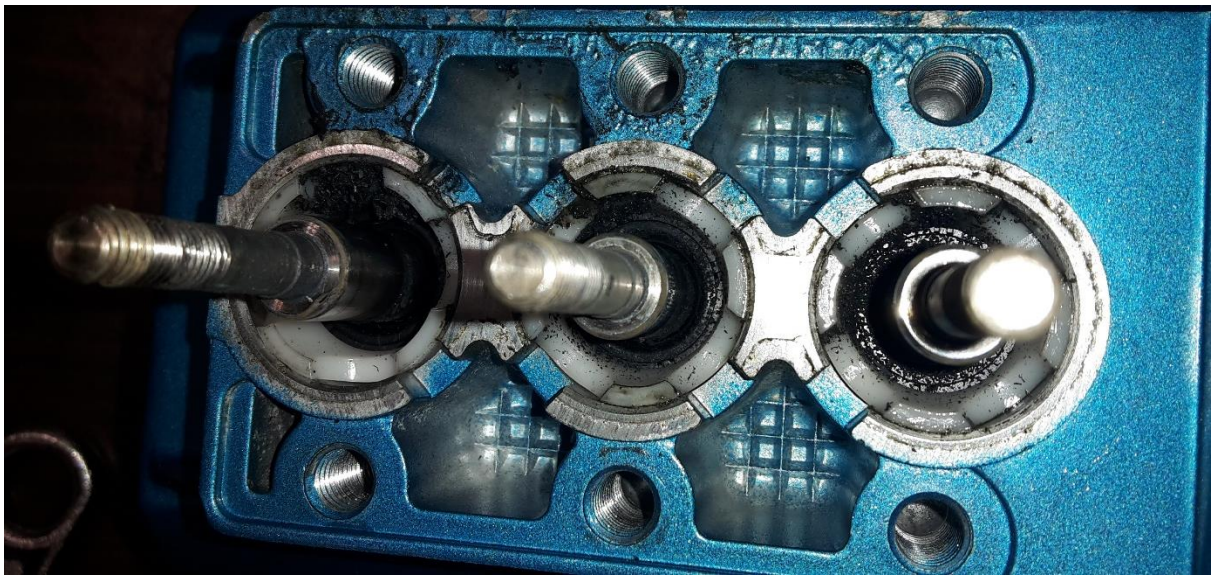

Figure 7.11 – Working fluid pump piston debris

Figure 7.10 shows the working fluid pump piston disassembly. The dynamic NBR o-ring seals on the pistons seem relatively intact. Figure 7.11 shows that at the bottom of the assembly a large amount of debris has collected, which is postulated to be disentegrated NBR seals.

Appendix F MATLAB 2016b Thermodynamic simulation

The following MATLAB code was developed to provide a theoretical thermodynamic simulation of the system. The processes were adapted in another script to accept experimental measurements as inputs to compare experimental performance with a theoretical case.

```
1
2   % ================================================
3   % Simple ORC analysis, R. Wijninckx, Apr 15, 2015
4   % ================================================
5
6   clear all
7   clc
8
9   %%%%%%%%%%%%%%%%%%%%%%%%%%%%%%%%%%%%%%%%%%%%%%%%%%%%%%%%%%%%%%%%%%%%%%%%%%%%%%%
10  % refpropm  Thermophysical properties of pure substances and mixtures.
11  %   Calling sequence for pure substances:
12  %      result=refpropm(prop_req, spec1, value1, spec2, value2, substance1)
13  %
14  %   Calling predefined mixtures:
15  %      result=refpropm(prop_req, spec1, value1, spec2, value2, mixture1)
16  %
17  %   Calling user defined mixtures:
18  %      result=refpropm(prop_req, spec1, value1, spec2, value2,
19  %                                          substance1, substance2, ..., x)
20  %
21  %   where
22  %       prop_req    character string showing the requested properties
23  %                   Each property is represented by one character:
24  %                           0   Refprop DLL version number
25  %                           A   Speed of sound [m/s]
26  %                           B   Volumetric expansivity (beta) [1/K]
27  %                           C   Cp [J/(kg K)]
28  %                           D   Density [kg/m^3]
29  %                           F   Fugacity [kPa] (returned as an array)
30  %                           G   Gross heating value [J/kg]
31  %                           H   Enthalpy [J/kg]
32  %                           I   Surface tension [N/m]
33  %                           J   Isenthalpic Joule-Thompson coeff [K/kPa]
34  %                           K   Ratio of specific heats (Cp/Cv) [-]
35  %                           L   Thermal conductivity [W/(m K)]
36  %                           M   Molar mass [g/mol]
37  %                           N   Net heating value [J/kg]
38  %                           O   Cv [J/(kg K)]
39  %                           P   Pressure [kPa]
40  %                           Q   Quality (vapor fraction) (kg/kg)
41  %                           S   Entropy [J/(kg K)]
42  %                           T   Temperature [K]
43  %                           U   Internal energy [J/kg]
44  %                           V   Dynamic viscosity [Pa*s]
45  %                           X   Liquid phase & gas phase comp.(mass frac.)
46  %                           Y   Heat of Vaporization [J/kg]
47  %                           Z   Compressibility factor
48  %                           $   Kinematic viscosity [cm^2/s]
49  %                           %   Thermal diffusivity [cm^2/s]
50  %                           ^   Prandtl number [-]
51  %                           )   Adiabatic bulk modulus [kPa]
52  %                           |   Isothermal bulk modulus [kPa]
53  %                           =   Isothermal compressibility [1/kPa]
```

```
%                           ~   Cstar [-]
%                           `   Throat mass flux [kg/(m^2 s)]
%                           +   Liquid density of equilibrium phase
%                           -   Vapor density of equilibrium phase
%
%                           E   dP/dT (along the saturation line) [kPa/K]
%                           #   dP/dT     (constant rho) [kPa/K]
%                           R   d(rho)/dP (constant T)   [kg/m^3/kPa]
%                           W   d(rho)/dT (constant p)   [kg/(m^3 K)]
%                           !   dH/d(rho) (constant T)   [(J/kg)/(kg/m^3)]
%                           &   dH/d(rho) (constant P)   [(J/kg)/(kg/m^3)]
%                           (   dH/dT     (constant P)   [J/(kg K)]
%                           @   dH/dT     (constant rho) [J/(kg K)]
%                           *   dH/dP     (constant T)   [J/(kg kPa)]
%
%       spec1           first input character:  T, P, H, D, C, R, or M
%                         T, P, H, D:  see above
%                         C:  properties at the critical point
%                         R:  properties at the triple point
%                         M:  properties at Tmax and Pmax
%                            (Note: if a fluid's lower limit is higher
%                             than the triple point, the lower limit will
%                             be returned)
%
%       value1          first input value
%
%       spec2           second input character:  P, D, H, S, U or Q
%
%       value2          second input value
%
%       substance1      file name of the pure fluid (or the first
%                       component of the mixture)
%
%       mixture1        file name of the predefined fluid mixture
%                       with the extension ".mix" included
%
%       substance2,substance3,...substanceN
%                       name of the other substances in the
%                       mixture. Up to 20 substances can be handled.
%                       Valid substance names are equal to the file names
%                       in the C:\Program Files\REFPROP\fluids\' directory.
%
%       x               vector with mass fractions of the substances
%                       in the mixture.
%
%   Examples:
%   1) P = refpropm('P','T',373.15,'Q',0,'water') gives
%      Vapor pressure of water at 373.15 K in [kPa]
%
%   2) [S Cp] = refpropm('SC','T',373.15,'Q',1,'water') gives
%      Entropy and Cp of saturated steam at 373.15 K
%
%   3) D = refpropm('D','T',323.15,'P',1e2,'water','ammonia',[0.9 0.1])
%      Density of a 10% ammonia/water solution at 100 kPa and 323.15 K.
%
%   4) [x y] = refpropm('X','P',5e2,'Q',0.4,'R134a','R32',[0.8, 0.2])
%      Temperature as well as gas and liquid compositions for a mixture
%      of two refrigerants at a certain pressure and quality.
%      Note that, when 'X' is requested, two variables must be sent, the
%      first contains the liquid phase composition and the second
%      the vapor phase composition.
%
```

```
%   5) T=refpropm('T','C',0,' ',0,'water')
%      Critical temperature
%
%   6) T=refpropm('T','M',0,' ',0,'r410a.mix')
%      Maximum temperature that can be used to call properties.
%      Shows how to call a predefined mixture.
%
%%%%%%%%%%%%%%%%%%%%%%%%%%%%%%%%%%%%%%%%%%%%%%%%%%%%%%%%%%%%%%%%%%%%%%%%%%%%%%%

% Activate REFPROP 9.0
addpath('C:\_Data\ORC\ORC\REFPROP') %activate_refprop

%--------- Initialize fluid ---------%
workingfluid = {'R245fa','R365MFC','WATER','M1.mix'};
% ======== List of Working Fluid (ref REFPROP)======= %
% 1 : R245fa                                          %
% 2 : R365mfc
% 3 : WATER
% 4 : M1
% ================================================== %
%format shortG

FLUID = workingfluid{4};

%--------- System parameters ---------%

mdotr = 0.06; %mass flow rate in the system, kg/s

Eta_t = 0.60;   %isentropic efficiency of expander
Eta_p = 0.60;   %isentropic efficiency of pump
Eta_g = 0.85;   %electrical efficiency of generator
Eta_mot = 0.82; %electrical efficiency of pump motor

T_sat_vapor = 125; % Celsius, saturation temperature inside evaporator -
INPUT
T_sat_liquid = 30; % Celsius, saturation temperature inside condenser -
INPUT
P_high = 1250;     % kPa


DELTAT_superheat = 5; % superheat by 5 K inside evaporator
DELTAT_subcool = 5;   % subcool by 5 K inside condenser

T_sat_vapor_K = TempConvert2(T_sat_vapor,1); %Convert temperatures to K
T_sat_liquid_K = TempConvert2(T_sat_liquid,1);

x = zeros(1,9); % Phase array
T = zeros(1,9); % Temp array
P = zeros(1,9); % Pressure array
h = zeros(1,9); % Enthalpy array
h_isen = zeros(1,9); %Isentropic Enthalpy array
d = zeros(1,9); % Density array
v = zeros(1,9); % Specific Volume array
s = zeros(1,9); % Entropy array
DATARRAY = zeros(9,8);

%--------- Boiling Process (State 7->8->1) ---------%
x(7) = 0; % Saturated Liquid (quality of 0%)
P(7) = P_high;
T(7) = refpropm('T','P',P(7),'Q',x(7),FLUID);
```

```
176  s(7) = refpropm('S','T',T(7),'Q',x(7), FLUID); % Compute Entropy [J/(kg K)]
177  %P(7) = refpropm('P','T',T(7),'Q',x(7), FLUID); % Compute Pressure [kPa]
178  h(7) = refpropm('H','T',T(7),'Q',x(7), FLUID); % Compute Enthalpy [J/kg]
179  d(7) = refpropm('D','T',T(7),'Q',x(7), FLUID); % Compute Density [kg/m^3]
180  v(7) = 1/d(7); % Compute Volume [m^3/kg]
181
182  x(8) = 1; % Saturated Vapor (quality of 100%)
183  P(8) = P(7);
184  T(8) = refpropm('T','P',P(8),'Q',x(8),FLUID);
185  s(8) = refpropm('S','T',T(8),'Q',x(8), FLUID); % Compute Entropy
186  %P(8) = refpropm('P','T',T(8),'Q',x(8), FLUID); % Compute Pressure
187  h(8) = refpropm('H','T',T(8),'Q',x(8), FLUID); % Compute Enthalpy
188  d(8) = refpropm('D','T',T(8),'Q',x(8), FLUID); % Compute Density
189  v(8) = 1/d(8); % Compute Volume
190
191  P(1) = P(8);
192  T(1) = T(8) + DELTAT_superheat;
193  h(1) = refpropm('H','T',T(1),'P',P(1), FLUID);
194  s(1) = refpropm('S','T',T(1),'P',P(1), FLUID);
195  d(1) = refpropm('D','T',T(1),'P',P(1), FLUID);
196  v(1) = 1/d(1);
197
198  %--------- Expander Process (State 1->2) ---------%
199  T(3) = T_sat_liquid_K;
200  x(3) = 1;
201  s(3) = refpropm('S','T',T(3),'Q',x(3), FLUID); % Compute Entropy
202  P(3) = refpropm('P','T',T(3),'Q',x(3), FLUID); % Compute Pressure
203  h(3) = refpropm('H','T',T(3),'Q',x(3), FLUID); % Compute Enthalpy
204  d(3) = refpropm('D','T',T(3),'Q',x(3), FLUID); % Compute Density
205  v(3) = 1/d(3); % Compute Volume
206
207
208  P(2) = P(3);
209  h_isen(2) = refpropm('H','P',P(2),'S',s(1), FLUID);
210  h(2) = h(1) - Eta_t*(h(1)-h_isen(2));            % Enthalpy at Expander
211  outlet
212  T(2) = refpropm('T','P',P(2),'H',h(2), FLUID);   % Temperatrue at Expander
213  Outlet
214  s(2) = refpropm('S','P',P(2),'H',h(2), FLUID);   % Specific Entropy at
215  Expander Outlet
216  d(2) = refpropm('D','P',P(2),'H',h(2), FLUID);   % Density at Expander
217  Outlet
218  v(2) = 1/d(2);                                   % Volume at Expander
219  Outlet
220
221  DELTAh_Exp = h(1) - h(2);    % Specific work of Expander [J/kg]
222  Exp_r = v(2)/v(1);            % Expansion Ratio
223
224  %--------- Air-cooled Condenser Analysis (State 2->3, 3->4, 4->5) ---------
225  %
226
227  x(4) = 0;                   % saturated liquid
228  P(4) = P(3);
229  h(4) = refpropm('H','P',P(4),'Q',x(4), FLUID);
230  T(4) = refpropm('T','P',P(4),'Q',x(4), FLUID);
231  s(4) = refpropm('S','P',P(4),'Q',x(4), FLUID);
232  d(4) = refpropm('D','P',P(4),'Q',x(4), FLUID);
233  v(4) = 1/d(4);
234
235  P(5) = P(4);                % subcooled liquid
```

```
T(5) = T(4) - DELTAT_subcool;
h(5) = refpropm('H','T',T(5),'P',P(5), FLUID);
s(5) = refpropm('S','T',T(5),'P',P(5), FLUID);
d(5) = refpropm('D','T',T(5),'P',P(5), FLUID);
v(5) = 1/d(5);

DELTAh_Con = h(2) - h(5);    % heat rejected to cold sink

%--------- Condensate Pump Analysis (State 5->6) ---------%

P(6) = P(1);        % Pump Outlet Pressure
h_isen(6) = refpropm('H','P',P(6),'S',s(5), FLUID); % isentropic pump
outlet state
h(6) = h(5) + (h_isen(6)-h(5))/Eta_p;               % enthalpy at pump
outlet
T(6) = refpropm('T','P',P(6),'H',h(6), FLUID);
s(6) = refpropm('S','P',P(6),'H',h(6), FLUID);
d(6) = refpropm('D','P',P(6),'H',h(6), FLUID);
v(6) = 1/d(6);

DELTAh_pump = h(6)-h(5);     % Specific Work of Pump

%--------- Finned Tube Type Evaporator Analysis (State 6->7, 7->8, 8->1) --
-------%

DELTAh_Eva = h(1)-h(6);      % heat transferred to evaporator

T(9) = T(1);
s(9) = s(1);
P(9) = P(1);
h(9) = h(1);

%--------- Cycle Thermal Efficiency ---------%

eta_thermal = ((DELTAh_Exp - DELTAh_pump)/DELTAh_Eva)*100;

%--------- Cycle Performance Analysis ---------%

W_in = DELTAh_pump*mdotr;
W_out = DELTAh_Exp*mdotr;
W_net = W_out-W_in;

W_out_e = W_out*Eta_g;      %electrical expander work
W_in_e = W_in/Eta_mot;      %electrical pump work
W_net_e = W_out_e - W_in_e; %electrical net work

Q_in = DELTAh_Eva*mdotr;    %Q_evap
Q_out = DELTAh_Con*mdotr;   %Q_cond

eta_carnot = 1 - T(5)/T(1); %Carnot efficiency
eta_2ndlaw = eta_thermal/eta_carnot; %second law efficiency
eta_cycle_elec = (W_net_e/Q_in)*100; %electrical cycle efficiency
eta_2ndlaw_elec = eta_cycle_elec/eta_carnot; %electrical second law
efficiency

P_r = P(1)/P(2); %Pressure ratio

% Unit convert SI
% REFPROP uses units as follows
```

```
% Temperature [K], Entropy [J/(kg K)], Pressure [kPa], Enthalpy [J/kg]
% Density [kg/m^3], Volume [m^3/kg]

for i=1:9
    T(i) = TempConvert2(T(i),2);
    s(i) = s(i)/1000; % [J/(kg K)] -> [kJ/(kg K)]
    P(i) = P(i)*1000; % [kPa] -> [Pa]
    h(i) = h(i)/1000; % [J/kg] -> [kJ/kg]
    h_isen(i) = h_isen(i)/1000;
end
    DELTAh_Exp = DELTAh_Exp/1000;   % [J/(kg K)] -> [kJ/(kg K)]
    DELTAh_Con = DELTAh_Con/1000;   % [J/(kg K)] -> [kJ/(kg K)]
    DELTAh_pump = DELTAh_pump/1000; % [J/(kg K)] -> [kJ/(kg K)]
    DELTAh_Eva = DELTAh_Eva/1000;   % [J/(kg K)] -> [kJ/(kg K)]

% Arrange
DATARRAY(:,1) = s; %[kJ/(kg K)]
DATARRAY(:,2) = T; %[C]
DATARRAY(:,3) = x;
DATARRAY(:,4) = P; %[Pa]
DATARRAY(:,5) = h; %[kJ/kg]
DATARRAY(:,6) = h_isen; %[kJ/kg]
DATARRAY(:,7) = v; %[m^3/kg]
DATARRAY(:,8) = d; %[kg/m^3]




% Show Result

disp('======= Simple ORC analysis ======= ')
disp('Unit Setting  : SI C Pa kJ mass deg C')
disp(sprintf('Working Fluid : %s', FLUID))
disp(sprintf('Expander Isentropic Efficiency: %f', Eta_t))
disp(sprintf('Pump Isentropic Efficiency: %f', Eta_p))

disp('------Performance-------')
disp(sprintf('Specific Work of Expander:      %f', DELTAh_Exp))
disp(sprintf('Expansion Ratio:                %f', Exp_r))
disp(sprintf('Heat rejected to ACC:           %f', DELTAh_Con))
disp(sprintf('Specific Work of Pump:          %f', DELTAh_pump))
disp(sprintf('Heat tranferred to evaporator:  %f', DELTAh_Eva))
disp(sprintf('Cycle efficiency:               %f', eta_thermal))
disp(sprintf('Cycle electrical efficiency:    %f', eta_cycle_elec))
disp(sprintf('Pump Work:                      %f', W_in))
disp(sprintf('Pump Electrical Work:           %f', W_in_e))
disp(sprintf('Expander Work:                  %f', W_out))
disp(sprintf('Expander Electrical Work:       %f', W_out_e))
disp(sprintf('Net Work:                       %f', W_net))
disp(sprintf('Net Electrical Work:            %f', W_net_e))
disp(sprintf('Heat in:                        %f', Q_in))
disp(sprintf('Heat out:                       %f', Q_out))
disp(sprintf('Pressure ratio:                 %f', P_r))
disp(sprintf('Second Law Efficiency:          %f', eta_2ndlaw))
disp(sprintf('Second Law Electrical Efficien: %f', eta_2ndlaw_elec))
DATARRAY

%% Plot state points on T-s diagram
y = DATARRAY(:,2); % T, Temperature
x = DATARRAY(:,1); % s, entropy
```

```
355
356   figure(1)
357   hold on
358   plot(x,y,'-*')
359   xlabel('Entropy (kJ/kg.K)')
360   ylabel('Temperature (C)')
361
362   %% Generate Model on T-S for M1
363   i=1;
364   high = 34.7;
365   step = .1;
366
367   for p=1:step:high;
368           t1(i)=refpropm('T','P',p*100,'Q',0,FLUID)-273.15;
369           s1(i)=refpropm('S','P',p*100,'Q',0,FLUID)/1000;
370           i=i+1;
371   end
372
373   for j=1:step:high;
374           p=high-j+1;
375           t1(i)=refpropm('T','P',p*100,'Q',1,FLUID)-273.15;
376           s1(i)=refpropm('S','P',p*100,'Q',1,FLUID)/1000;
377           i=i+1;
378   end
379
380   plot(s1,t1)
381
382   hold off
383
```

Appendix G Experimental steady state data points

Row	Date	P1	P2	P2_Exp_In	P2_Exp_Out	P3	P4	T1_Evap_In	T2_Evap_Out	T2_Exp_In	T2_Exp_Out	T3_Cond_In	T4_Cond_Out	T5_HE_Surface	T6_Exhaust_Gas_In	T7_Exhaust_Gas_Out	T8_Ambient	T9_Hot_Oil	T10_Cooled_Oil	T11_Water_Inlet	T12_Water_Outlet	Superheat	Subcool	P___Oil	Electrical_load
1	25-05-15	628.2	641.1	611.4	153.9	150.8	151.4	14.3	128.6	127.4	88.6	86.6	13.0	108.4	230.1	167.6	18.1	134.1	71.0	12.7	14.2	41.0	21.2	0.0	200.0
2	25-05-15	627.0	633.7	615.0	138.3	136.0	133.3	14.5	123.9	123.1	88.0	86.6	13.0	109.4	230.1	166.8	18.6	131.5	67.6	12.5	14.0	36.4	18.2	0.0	500.0
3	25-05-15	598.8	596.6	587.9	121.1	111.4	111.9	14.3	87.3	86.3	36.3	34.9	12.7	107.1	230.8	162.6	19.6	123.4	51.1	12.4	14.2	1.4	14.8	0.0	500.0
4	25-05-15	601.5	594.1	585.8	123.1	108.8	108.9	14.4	86.7	85.7	36.2	33.6	12.7	107.6	231.0	162.6	20.2	123.1	47.4	12.4	14.4	0.9	15.2	0.0	500.0
5	26-05-15	613.1	607.4	595.3	117.9	108.4	109.3	14.0	87.9	87.3	35.9	34.2	12.6	107.6	229.7	161.6	18.1	123.0	51.4	12.5	14.3	1.9	14.2	0.0	156.0
6	26-05-15	587.8	582.1	570.3	119.8	109.5	109.9	14.1	86.7	85.8	36.2	34.7	12.6	107.7	229.6	162.1	18.7	121.8	51.3	12.5	14.2	2.1	14.6	0.0	500.0
7	29-06-15	657.3	655.2	645.7	140.5	136.8	134.0	12.2	91.2	90.6	41.4	40.9	10.4	103.5	230.2	158.7	17.4	103.4	83.7	10.2	11.9	2.0	21.2	0.0	500.0
8	29-06-15	823.6	826.3	821.5	134.3	128.0	129.8	12.6	114.0	112.6	69.4	67.2	10.6	138.3	262.1	199.5	17.6	151.9	65.6	10.2	12.3	14.2	19.8	0.0	1000.0
9	29-06-15	852.9	854.0	850.4	162.1	159.1	159.4	12.7	124.7	124.0	86.2	82.8	10.6	136.4	263.8	196.9	18.0	132.9	90.0	10.2	12.6	24.1	25.1	0.0	1000.0
10	29-06-15	897.1	895.2	878.3	152.5	148.1	146.2	12.5	122.6	122.3	90.8	86.5	10.6	136.7	263.6	197.3	17.9	132.9	88.4	10.2	12.8	21.1	23.4	0.0	1000.0
11	29-06-15	908.7	909.6	897.8	148.3	143.8	141.0	12.6	115.0	114.1	84.2	82.7	10.6	136.8	263.5	196.9	17.5	131.9	86.0	10.2	13.1	11.9	22.6	0.0	1000.0
12	30-06-15	604.7	630.3	583.2	124.9	121.9	117.0	12.1	89.3	88.6	40.3	40.3	10.4	105.2	229.0	161.7	18.6	120.3	57.3	10.1	11.8	4.0	18.0	0.0	500.0
13	30-06-15	969.3	971.7	956.6	149.7	141.5	140.3	12.6	111.9	111.5	71.2	70.1	10.7	136.1	265.0	193.8	18.5	128.2	96.6	10.3	13.1	6.6	22.7	0.0	1000.0
14	30-06-15	967.7	966.1	948.2	151.1	143.8	142.6	12.6	113.4	113.0	77.0	76.0	10.6	135.4	264.7	193.7	18.7	128.3	96.5	10.2	13.2	8.5	23.0	0.0	1300.0
15	11-08-15	574.3	579.7	569.3	274.5	274.9	278.2	11.6	124.4	123.3	94.5	91.5	10.7	106.2	227.6	165.1	13.2	128.2	73.0	10.5	11.8	39.6	41.2	334.8	500.0
16	11-08-15	613.7	610.9	599.5	166.4	163.7	163.9	11.7	91.4	90.8	58.8	58.3	10.7	105.4	228.3	162.7	13.7	122.9	61.2	10.6	12.2	5.2	25.7	316.0	500.0
17	13-08-15	677.6	674.0	663.5	206.1	205.4	206.4	13.1	110.8	110.2	80.9	79.6	11.1	110.4	229.6	165.5	18.0	113.3	82.8	10.8	12.4	20.5	31.8	294.9	500.0
18	13-08-15	615.1	610.3	603.0	168.8	162.9	162.1	12.6	88.4	87.6	45.8	45.3	10.8	109.5	229.7	162.4	18.6	105.5	71.8	10.6	12.4	1.8	26.0	278.2	500.0
19	13-08-15	571.2	563.8	553.2	160.0	150.9	152.0	12.8	84.4	83.6	43.3	42.3	11.1	107.4	230.7	160.4	18.5	100.8	65.3	10.8	12.7	1.1	24.2	272.6	500.0
20	13-08-15	584.3	576.1	565.4	157.7	150.9	150.7	12.8	85.2	84.4	43.0	42.0	11.1	107.5	229.6	160.0	17.9	100.8	65.8	10.9	12.7	1.0	23.8	276.8	1000.0
21	13-08-15	611.9	601.8	594.7	163.5	159.1	159.4	12.8	88.2	87.4	45.2	44.7	11.0	109.3	229.7	162.0	19.4	104.9	71.7	10.9	12.6	2.1	25.0	281.5	1000.0
22	13-08-15	647.5	642.5	635.1	186.4	183.4	181.8	13.1	92.5	91.9	63.9	63.2	10.9	111.9	229.9	164.8	19.3	110.2	78.5	10.6	12.3	4.0	28.9	281.0	1000.0
23	13-08-15	607.4	602.6	597.3	269.4	267.5	272.9	13.3	111.3	110.5	85.7	84.0	10.9	113.2	230.1	166.8	19.6	113.8	84.2	10.6	12.1	25.0	40.5	293.2	1000.0
24	13-08-15	655.6	650.0	643.1	217.4	215.9	220.2	13.1	111.4	110.8	86.4	85.5	11.0	112.3	230.1	166.3	18.5	113.4	82.9	10.8	12.5	22.3	33.5	287.0	0.0
25	13-08-15	678.3	677.7	676.7	293.4	292.9	297.3	13.5	114.0	113.4	89.4	87.6	11.1	111.7	230.2	167.7	18.0	116.2	88.0	10.9	12.4	23.0	43.1	289.5	500.0
26	17-08-15	675.3	676.9	672.6	193.4	192.3	191.8	13.4	98.7	98.2	71.3	70.6	11.4	108.9	229.9	163.0	18.1	106.8	85.3	11.0	12.6	8.0	29.5	301.2	500.0
27	17-08-15	614.9	609.2	597.5	184.1	178.0	177.8	12.9	87.7	87.0	48.0	47.6	11.3	109.1	229.5	160.2	19.2	101.1	78.1	11.1	12.9	1.4	28.1	293.4	500.0
28	17-08-15	574.3	568.3	558.6	164.6	156.7	157.4	12.8	84.9	83.9	44.3	43.4	11.3	108.5	229.9	159.0	19.5	97.1	73.0	11.1	12.9	0.9	24.8	287.3	500.0
29	17-08-15	593.2	585.3	577.6	164.3	155.7	157.2	12.8	86.0	85.1	44.2	43.3	11.3	109.4	229.9	159.2	20.1	97.7	73.9	11.1	12.9	0.9	24.8	289.6	1000.0
30	17-08-15	633.1	627.1	623.6	179.0	175.2	174.5	13.0	89.1	88.4	47.5	47.1	11.3	109.9	229.3	160.6	18.5	101.7	79.1	11.1	12.9	1.2	27.4	295.4	1000.0
31	17-08-15	637.0	636.1	626.2	199.9	196.7	198.4	13.4	98.5	97.7	70.7	69.8	11.4	110.5	230.3	162.5	19.1	105.4	83.6	11.2	12.8	10.4	30.5	300.3	1000.0
32	17-08-15	642.7	643.1	638.9	278.2	276.9	282.0	13.7	107.0	106.0	81.7	80.0	11.5	112.8	230.2	164.2	19.2	109.6	89.1	11.1	12.6	17.9	40.9	314.3	1000.0
33	18-08-15	748.6	752.5	737.3	187.1	184.1	185.9	13.2	137.1	136.2	100.9	99.2	11.0	131.7	251.1	190.5	19.6	146.9	70.1	10.6	12.5	42.2	29.0	412.4	500.0
34	18-08-15	798.9	805.3	789.1	165.6	159.7	161.0	13.4	112.7	110.8	78.3	77.5	11.2	131.3	251.3	189.4	20.0	143.2	65.6	10.8	13.1	14.1	25.2	364.0	500.0
35	18-08-15	770.9	772.1	757.3	159.1	153.8	155.0	13.0	102.5	101.1	61.2	58.7	11.1	129.8	251.1	187.6	19.7	140.0	59.5	10.9	13.1	6.0	24.0	343.2	500.0
36	18-08-15	730.6	724.1	713.7	155.2	145.1	146.5	12.9	97.0	95.8	45.1	43.9	11.2	128.1	251.1	185.1	19.5	133.4	49.8	11.0	13.3	3.2	23.2	324.3	500.0
37	18-08-15	763.4	758.6	749.1	156.3	147.0	146.7	13.0	98.7	97.7	46.7	43.9	11.3	129.2	251.1	185.3	19.9	133.6	50.7	11.1	13.5	3.1	23.4	316.5	1000.0
38	18-08-15	783.0	776.2	767.6	159.8	153.3	154.3	13.2	102.6	101.4	56.0	55.4	11.3	128.8	251.1	187.6	19.7	138.0	60.0	11.1	13.1	5.9	24.0	321.7	1000.0
39	18-08-15	808.6	809.3	794.7	163.9	159.0	158.8	13.6	110.1	109.3	75.5	74.6	11.4	133.5	251.3	189.8	20.3	141.7	66.5	11.1	13.1	12.3	24.6	331.6	1000.0
40	19-08-15	804.5	806.6	795.4	338.1	336.1	339.7	13.4	126.5	125.8	100.7	98.9	11.2	128.1	249.6	187.4	19.0	129.1	92.4	11.0	12.8	28.7	47.7	347.4	500.0

Row	Date	P1	P2	P2_Exp_In	P2_Exp_Out	P3	P4	T1_Evap_In	T2_Evap_Out	T2_Exp_In	T2_Exp_Out	T3_Cond_In	T4_Cond_Out	T5_HE_Surface	T6_Exhaust_Gas_In	T7_Exhaust_Gas_Out	T8_Ambient	T9_Hot_Oil	T10_Cooled_Oil	T11_Water_Inlet	T12_Water_Outlet	Superheat	Subcool	P___Oil	Electrical_load
41	19-08-15	765.5	763.9	753.9	178.4	173.8	174.4	13.1	99.1	98.5	56.9	56.1	11.3	124.4	249.4	183.5	17.7	119.7	79.1	11.1	13.2	3.7	27.3	310.0	500.0
42	19-08-15	712.6	706.9	694.8	164.7	156.6	156.4	12.9	94.8	94.0	46.0	44.8	11.3	121.7	249.0	180.8	16.8	115.0	72.4	11.2	13.4	2.5	24.9	293.8	500.0
43	19-08-15	739.3	733.3	722.2	165.9	156.1	156.0	13.0	96.2	95.5	45.8	44.7	11.4	123.5	249.1	181.5	17.3	115.6	73.4	11.2	13.4	2.4	25.0	295.9	1000.0
44	19-08-15	761.8	757.1	747.7	177.5	172.8	171.7	13.0	98.8	98.3	54.4	53.9	11.4	122.8	248.2	182.5	17.2	119.4	79.3	11.3	13.4	3.8	27.0	301.1	1000.0
45	19-08-15	784.9	782.0	772.5	187.9	182.7	183.4	13.5	106.7	106.1	75.3	74.4	11.5	126.4	249.0	184.5	18.4	122.2	82.7	11.3	13.3	10.2	28.6	300.1	1000.0
46	20-08-15	705.0	697.2	686.8	166.0	159.7	158.5	12.5	94.1	93.1	45.7	44.8	11.0	125.9	250.6	182.1	19.1	115.3	71.4	10.7	12.9	2.1	25.4	290.3	500.0
47	20-08-15	779.4	774.4	761.9	173.4	166.5	166.5	13.2	98.5	97.7	47.7	46.8	11.5	128.2	251.3	183.0	20.0	113.0	83.7	11.0	13.4	2.4	26.2	324.2	1000.0
48	20-08-15	836.6	836.2	826.1	191.7	187.0	187.0	13.4	106.6	106.2	75.6	74.9	11.4	127.1	251.4	181.8	19.6	119.1	90.1	11.0	13.4	7.6	29.3	362.9	1000.0
49	20-08-15	857.6	857.8	848.6	243.4	242.0	245.5	13.8	122.9	122.2	91.3	89.9	11.5	129.5	251.8	184.5	20.2	125.0	97.7	11.1	13.3	22.5	36.6	389.3	1000.0
50	20-08-15	769.8	769.6	755.4	174.5	168.1	168.1	13.0	98.5	97.9	49.0	48.0	11.4	123.4	250.3	178.5	19.0	114.0	83.7	11.2	13.8	3.0	26.5	345.2	500.0
51	20-08-15	809.8	810.6	797.3	193.2	189.6	188.8	13.6	103.9	103.1	72.6	71.8	11.5	122.3	250.2	179.9	18.1	117.7	88.8	11.2	13.6	5.9	29.4	357.3	500.0
52	20-08-15	852.9	853.7	839.4	222.4	222.2	224.9	13.7	120.8	120.3	88.5	87.2	11.5	126.2	250.4	182.7	19.3	123.7	96.5	11.2	13.4	21.0	33.7	387.7	500.0
53	20-08-15	842.5	846.3	825.8	254.2	251.2	255.3	13.7	122.6	122.0	92.9	91.6	11.6	124.5	249.9	182.9	17.9	124.5	97.6	11.3	13.4	23.4	37.9	393.1	500.0
54	20-08-15	738.6	733.4	720.4	172.8	164.1	164.6	13.0	95.8	95.1	47.3	45.9	11.5	115.8	249.0	175.6	17.0	110.7	80.2	11.3	13.8	2.2	26.1	335.4	500.0
55	20-08-15	781.1	778.9	765.2	180.6	176.8	176.8	13.0	99.2	98.7	52.7	52.1	11.5	121.2	249.7	178.1	17.1	114.8	85.5	11.3	13.7	3.3	27.4	351.9	500.0
56	20-08-15	783.9	777.4	765.6	172.9	164.7	162.7	13.1	98.3	97.6	47.2	45.8	11.5	124.6	250.1	178.7	18.9	113.0	82.4	11.3	13.8	2.2	26.1	345.4	1000.0
57	20-08-15	810.5	808.1	797.2	180.9	174.3	174.9	13.1	101.2	100.6	53.5	53.2	11.5	124.9	250.0	180.1	18.6	116.7	87.4	11.3	13.7	3.4	27.4	354.3	1000.0
58	21-08-15	699.4	691.9	681.9	161.1	153.3	151.5	12.6	93.5	92.6	44.7	43.3	11.0	126.5	249.3	180.9	18.4	114.2	70.1	10.8	13.2	1.9	24.5	327.8	500.0
59	21-08-15	739.9	729.7	718.9	161.8	153.6	151.8	12.8	95.7	95.0	45.0	43.6	11.1	128.2	249.4	181.7	18.9	115.7	71.6	10.9	13.4	2.1	24.6	334.0	1000.0
60	21-08-15	732.2	729.7	718.3	167.7	163.7	161.9	12.9	97.5	96.7	49.7	49.2	11.2	128.9	250.1	183.8	19.3	119.4	76.7	11.0	13.3	3.9	25.5	342.3	500.0
61	21-08-15	756.9	751.8	740.8	167.2	163.2	161.3	12.9	98.5	97.9	49.6	49.1	11.1	130.4	250.1	184.4	19.5	120.0	77.5	11.0	13.2	3.8	25.5	343.0	1000.0
62	21-08-15	815.0	815.5	804.1	186.9	184.2	185.9	13.6	115.3	114.8	83.6	82.6	11.4	131.2	250.2	187.3	19.5	125.4	85.6	11.2	13.2	17.3	28.5	361.7	500.0
63	21-08-15	778.7	778.7	765.9	279.5	276.6	282.0	13.7	126.6	126.0	100.7	99.3	11.6	132.7	250.4	189.4	19.6	129.0	90.8	11.4	13.3	30.5	41.0	365.0	500.0
64	24-08-15	793.5	788.9	772.4	159.6	146.8	146.7	12.9	101.3	99.8	47.4	46.1	11.2	143.2	266.8	201.6	18.2	147.5	46.6	11.0	13.8	4.0	24.0	357.3	500.0
65	24-08-15	834.5	832.0	816.0	158.7	146.7	146.6	13.0	103.7	102.2	48.0	46.9	11.3	146.3	267.4	202.7	19.2	148.6	47.7	11.0	13.8	4.1	23.8	359.7	1000.0
66	24-08-15	799.9	801.8	783.0	159.4	149.7	149.9	12.9	104.3	102.1	57.4	56.7	11.3	145.1	267.7	203.4	18.8	149.4	52.3	11.0	13.7	5.7	24.0	359.1	500.0
67	24-08-15	832.5	834.1	811.3	160.3	150.6	150.0	13.1	105.2	103.8	58.4	57.8	11.3	147.1	267.6	204.0	19.0	150.1	53.0	11.1	13.9	5.9	24.1	360.6	1000.0
68	24-08-15	834.6	833.4	823.3	161.6	152.8	152.9	13.2	110.1	107.0	69.8	69.1	11.3	146.8	268.1	205.2	19.1	152.4	57.8	11.1	13.7	8.5	24.3	353.4	500.0
69	24-08-15	867.8	872.2	852.3	161.6	155.1	153.4	13.2	110.6	108.6	70.5	69.9	11.4	147.9	267.7	205.4	18.9	152.8	58.5	11.2	13.8	8.6	24.2	357.1	1000.0
70	24-08-15	871.3	881.1	859.5	164.1	157.0	157.9	13.4	124.1	120.1	85.7	84.8	11.5	148.8	268.0	206.6	19.7	155.0	63.7	11.2	13.7	19.8	24.6	356.2	500.0
71	24-08-15	911.4	917.6	900.2	165.1	160.3	158.8	13.4	122.3	120.3	85.7	84.9	11.6	149.2	268.0	207.2	19.0	155.9	65.0	11.3	13.7	18.0	24.7	353.9	1000.0
72	25-08-15	827.4	831.5	815.3	160.7	155.8	154.0	13.1	115.4	112.7	77.0	76.2	11.1	143.1	264.0	202.1	18.9	152.9	61.0	10.7	13.0	14.6	24.3	353.9	500.0
73	25-08-15	888.3	892.8	876.6	162.8	158.5	157.7	13.5	119.0	117.3	82.8	82.0	11.3	146.0	265.6	204.4	19.3	153.9	64.1	10.8	13.5	16.1	24.5	344.1	1000.0
74	25-08-15	819.9	817.7	800.4	168.7	159.0	158.1	13.1	101.9	101.0	49.2	48.1	11.3	141.6	265.3	199.4	19.8	126.3	75.1	11.0	13.8	3.7	25.6	312.1	1000.0
75	25-08-15	781.0	778.9	761.6	169.7	159.2	159.2	13.1	100.1	99.0	49.3	48.1	11.4	140.7	265.5	198.8	19.0	124.9	73.7	11.1	13.8	3.8	25.7	309.2	500.0
76	25-08-15	794.9	794.6	778.3	171.8	162.7	162.9	13.1	102.4	101.3	58.9	58.2	11.4	141.9	265.9	200.4	19.1	127.8	77.2	11.1	13.7	5.2	26.0	306.7	497.0
77	25-08-15	819.4	819.3	801.6	171.8	164.3	163.2	13.2	103.3	102.5	59.8	59.2	11.5	142.8	265.6	200.5	19.0	128.4	78.2	11.2	13.8	5.1	26.0	310.0	1000.0
78	25-08-15	831.5	841.2	814.5	173.4	167.5	167.2	13.6	107.2	106.1	71.8	71.1	11.5	142.9	265.9	201.5	19.7	130.5	81.4	11.1	13.7	8.1	26.2	315.2	500.0
79	25-08-15	863.0	874.3	846.9	174.0	166.9	166.3	13.5	108.8	107.7	73.4	72.8	11.5	144.3	266.0	202.3	19.8	131.6	82.6	11.2	13.8	8.0	26.3	316.6	1000.0
80	25-08-15	859.1	865.1	847.9	189.2	184.3	184.9	13.5	123.8	123.9	91.5	90.6	11.5	144.8	266.0	203.1	19.2	133.7	85.9	11.1	13.7	24.2	28.8	322.8	500.0

Row	Date	P1	P2	P2_Exp_In	P2_Exp_Out	P3	P4	T1_Evap_In	T2_Evap_Out	T2_Exp_In	T2_Exp_Out	T3_Cond_In	T4_Cond_Out	T5_HE_Surface	T6_Exhaust_Gas_In	T7_Exhaust_Gas_Out	T8_Ambient	T9_Hot_Oil	T10_Cooled_Oil	T11_Water_Inlet	T12_Water_Outlet	Superheat	Subcool	P___Oil	Electrical_load
81	25-08-15	868.7	870.1	854.5	191.0	185.7	187.0	13.4	125.4	124.9	93.6	92.7	11.6	145.5	265.1	203.2	19.9	133.9	86.3	11.2	13.7	24.8	29.0	322.4	1000.0
82	25-08-15	924.9	926.4	914.9	442.1	438.6	441.9	13.5	140.2	139.6	118.6	117.1	11.6	148.8	264.9	206.6	19.7	141.9	98.4	11.2	13.8	36.6	56.9	365.4	500.0
83	26-08-15	771.0	768.5	746.6	173.9	165.1	164.7	12.8	99.1	98.0	49.8	48.7	11.0	135.3	263.9	196.1	18.4	117.5	82.4	10.6	13.5	3.6	26.8	321.1	500.0
84	26-08-15	801.6	799.2	786.0	173.6	164.7	164.7	12.8	100.5	99.7	49.9	48.7	11.0	134.9	263.7	196.1	18.5	118.6	83.8	10.7	13.6	3.1	26.7	327.7	1000.0
85	26-08-15	795.1	796.0	774.4	177.8	171.5	171.1	13.1	101.9	100.9	61.8	61.1	11.1	137.0	264.6	196.9	18.9	120.4	86.0	10.7	13.6	5.0	27.3	342.6	500.0
86	26-08-15	819.8	824.1	806.0	178.9	173.3	172.9	13.2	103.4	102.6	65.1	64.4	11.2	139.1	264.8	197.3	19.3	121.6	87.0	10.8	13.6	5.0	27.4	362.9	1000.0
87	26-08-15	839.5	837.0	830.7	191.7	188.3	187.0	13.6	113.0	112.6	82.0	81.3	11.3	140.1	265.3	198.0	19.7	124.3	90.2	10.8	13.5	13.8	29.4	391.9	500.0
88	26-08-15	897.5	892.2	882.1	188.7	184.4	185.0	13.5	113.4	113.1	81.9	81.2	11.3	140.1	264.8	197.9	19.7	126.0	92.4	10.9	13.7	11.7	28.9	399.8	1000.0
89	26-08-15	922.2	924.0	904.7	270.5	269.6	272.5	13.6	131.1	130.4	102.9	101.7	11.4	140.9	264.4	200.3	18.9	132.6	101.0	11.0	13.5	27.9	40.1	457.3	500.0
90	27-08-15	854.1	856.0	835.7	158.2	149.1	148.0	13.2	107.7	105.5	60.8	60.1	11.3	155.6	278.5	215.8	19.5	159.0	49.1	10.9	13.9	6.4	23.7	376.1	500.0
91	27-08-15	889.4	890.0	873.6	158.8	150.9	149.2	13.1	109.0	107.2	62.1	61.4	11.2	156.8	278.1	215.8	19.6	158.9	50.5	10.9	13.9	6.2	23.9	368.5	1000.0
92	27-08-15	892.0	894.5	878.6	159.6	153.0	151.2	13.4	114.3	111.2	73.7	73.1	11.3	156.7	279.1	217.4	20.2	161.4	55.4	11.0	13.9	10.0	24.0	368.9	500.0
93	27-08-15	933.5	944.7	921.0	159.6	151.4	151.5	13.4	115.4	113.0	74.5	73.8	11.4	156.8	278.5	217.5	19.5	161.8	56.4	11.0	13.9	9.8	23.9	359.7	1000.0
94	27-08-15	929.7	940.5	918.5	161.3	156.7	156.5	13.6	126.9	123.3	88.4	87.5	11.5	157.0	279.0	218.6	19.5	163.9	61.5	11.1	13.8	20.1	24.1	359.1	500.0
95	27-08-15	974.8	990.8	958.2	160.8	156.3	156.2	13.6	126.4	124.3	89.2	88.4	11.5	158.7	279.3	219.4	19.3	164.9	62.6	11.0	13.7	19.3	24.0	356.9	1000.0
96	27-08-15	934.5	935.7	915.4	171.3	163.1	161.7	13.3	110.3	109.4	67.6	66.8	11.4	154.9	278.8	214.7	19.4	137.3	80.8	11.1	14.2	6.4	25.9	351.2	1000.0
97	27-08-15	890.0	892.8	874.7	171.3	163.2	162.5	13.2	108.8	107.3	65.2	64.6	11.4	153.4	277.9	213.5	19.2	135.7	78.8	11.0	14.4	6.2	25.9	340.9	500.0
98	27-08-15	938.3	946.7	922.1	173.8	167.3	167.0	13.6	114.7	113.6	78.4	77.7	11.4	154.4	279.2	215.6	19.5	139.2	83.4	11.0	13.9	10.3	26.3	334.1	500.0
99	27-08-15	977.5	980.5	966.7	173.6	167.0	166.7	13.6	116.1	114.9	79.2	78.5	11.5	155.4	278.7	216.1	19.2	140.1	84.7	11.0	14.0	9.6	26.3	327.2	1000.0
100	27-08-15	961.0	972.9	948.1	190.5	186.0	187.1	13.6	134.2	132.0	100.0	99.0	11.4	155.8	278.6	216.7	19.3	142.3	88.2	11.0	13.9	27.5	29.0	329.3	500.0
101	27-08-15	979.2	989.1	969.6	187.6	183.9	184.4	13.6	132.0	130.7	98.6	97.6	11.5	156.0	278.6	216.6	19.1	142.4	88.4	11.1	14.0	25.2	28.5	331.5	1000.0
102	27-08-15	938.3	943.8	921.3	242.6	240.6	244.7	13.7	143.1	142.8	112.0	110.4	11.5	156.2	279.2	218.4	18.9	145.9	94.0	11.1	13.8	39.5	36.5	342.7	500.0
103	28-08-15	936.1	947.5	920.1	182.2	175.0	173.0	13.2	112.3	111.4	76.5	75.8	11.2	150.6	277.8	208.8	19.6	131.4	91.0	10.7	14.2	8.1	28.0	392.2	500.0
104	28-08-15	965.9	975.6	951.3	182.4	175.5	173.2	13.2	113.3	112.6	77.5	76.8	11.2	151.0	277.4	208.8	19.2	132.3	92.1	10.8	14.1	7.9	28.0	398.4	1000.0
105	28-08-15	959.7	964.9	947.0	199.1	192.6	193.2	13.3	123.8	125.0	93.0	92.1	11.3	150.4	277.1	209.4	18.5	134.3	95.2	10.9	14.1	20.6	30.6	422.8	500.0
106	28-08-15	1003.1	1015.5	988.5	198.7	193.6	194.3	13.4	126.5	126.1	94.7	93.8	11.3	150.9	277.0	209.5	19.5	135.5	96.7	10.9	14.2	19.8	30.5	423.7	1000.0
107	28-08-15	973.8	989.7	959.6	160.8	150.5	150.5	13.2	117.0	114.5	75.8	75.0	11.4	166.0	289.0	228.4	18.8	169.4	52.6	11.0	14.3	9.5	24.1	414.9	1000.0
108	28-08-15	948.2	951.9	934.1	161.2	151.8	150.6	13.3	116.9	114.1	76.4	75.5	11.4	167.1	290.4	229.3	19.4	170.0	52.2	11.0	14.2	10.2	24.1	399.6	500.0
109	28-08-15	997.3	1014.5	981.3	163.2	155.2	154.3	13.5	129.9	125.9	90.9	90.0	11.5	168.8	290.6	230.7	19.4	173.5	58.4	11.0	14.1	19.9	24.4	430.4	500.0
110	28-08-15	1037.4	1054.5	1030.1	162.6	155.3	155.2	13.5	128.8	126.6	90.8	89.8	11.5	169.5	290.4	231.0	19.5	173.5	59.3	11.0	14.1	18.5	24.3	420.6	1000.0
111	28-08-15	967.0	986.8	953.3	172.1	167.4	166.4	13.5	153.9	147.5	114.4	112.9	11.5	169.9	290.3	231.8	19.2	175.2	63.7	11.1	14.1	42.8	25.9	452.3	500.0
112	28-08-15	986.0	1009.8	972.5	170.8	165.8	164.4	13.4	151.3	146.4	114.6	113.3	11.5	169.8	289.2	231.2	18.9	174.5	63.6	11.1	14.1	40.8	25.8	441.0	1000.0
113	31-08-15	902.5	919.3	886.6	181.3	173.1	171.2	13.3	122.6	121.5	94.1	93.3	11.3	165.5	290.2	226.3	19.7	144.5	80.0	10.9	14.4	19.9	27.7	361.9	500.0
114	31-08-15	1049.2	1056.8	1032.8	174.9	164.8	164.7	13.3	122.4	121.1	85.6	84.9	11.4	167.1	289.9	227.8	18.8	146.8	84.4	11.1	14.6	12.8	26.5	323.1	1000.0
115	31-08-15	1040.1	1065.1	1021.8	190.4	182.7	182.6	13.3	139.1	137.3	106.1	105.0	11.4	168.1	290.7	229.3	20.4	149.3	88.5	11.1	14.5	29.5	29.1	315.2	500.0
116	31-08-15	1070.0	1094.1	1055.1	189.3	181.6	182.5	13.5	140.1	138.0	106.8	105.8	11.6	169.7	291.1	230.1	20.3	150.1	89.5	11.1	14.5	28.7	28.8	311.5	1000.0
117	31-08-15	992.5	1007.7	972.7	270.4	266.8	269.6	13.6	153.6	153.2	124.8	123.5	11.7	171.0	291.6	232.1	20.8	155.2	97.3	11.2	14.3	47.5	39.8	333.9	500.0
118	31-08-15	993.8	1006.6	975.0	276.9	272.7	275.7	13.6	153.8	153.4	125.5	124.1	11.6	171.1	291.4	232.1	20.6	155.4	97.5	11.2	14.4	47.7	40.6	331.8	1000.0

Row	Speed_Oil_Pump	oil_massflow	Speed_Feed_Pump	Capstone_Power_setting	wf_Vdot	wf_mdotr	scroll_RPM	W_gross	W_net	W_gross_theory	W_gross_diff	eta_scroll_isen	Scroll_filling_factor	eta_feedpump_isen	eta_cycle_gross (%)	eta_cycle_net	PR	Q_exhaust_ideal	Q_exhaust	Q_oil	Q_evap	Q_water
1	6.0	0.1	14.0	5.0	0.0	0.0	2627.1	132.2	13.9	562.5	-0.8	0.2	1.8	0.2	1.6	0.2	4.0	18689.2	9828.2	11888.0	8287.6	5944.5
2	6.0	0.1	14.0	5.0	0.0	0.0	2318.7	236.3	118.1	554.9	-0.6	0.3	2.0	0.2	2.9	1.4	4.4	18698.0	9955.7	11984.7	8151.2	5839.2
3	6.0	0.1	22.0	5.0	0.0	0.0	2253.7	228.3	52.4	895.7	-0.7	0.2	3.3	0.2	1.8	0.4	4.9	18819.9	10732.9	13382.3	12395.9	7098.0
4	6.0	0.1	28.0	5.0	0.0	0.1	2360.3	210.7	-8.8	1252.9	-0.8	0.1	4.4	0.2	1.2	-0.1	4.8	18857.8	10769.9	13985.9	17059.7	8243.9
5	6.0	0.1	22.0	15.0	0.0	0.0	1855.2	254.9	78.7	822.6	-0.7	0.2	4.0	0.2	2.0	0.6	5.0	27001.7	15525.8	13261.7	12466.4	6873.5
6	6.0	0.1	22.0	15.0	0.0	0.0	2317.4	215.8	40.1	901.1	-0.8	0.2	3.3	0.2	1.7	0.3	4.8	26971.4	15394.6	13029.5	12405.2	6966.1
7	20.0	0.2	18.0	5.0	1.5	0.0	1987.9	266.7	118.9	551.3	-0.5	0.3	2.3	0.2	3.1	1.4	4.6	18709.2	11237.4	11631.6	8656.9	6735.3
8	6.0	0.1	18.0	15.0	1.5	0.0	2286.9	431.3	280.7	754.4	-0.4	0.4	1.7	0.2	4.6	3.0	6.1	35314.5	14380.0	16514.9	9396.7	8307.1
9	13.0	0.1	18.0	15.0	1.5	0.0	2283.0	500.8	349.8	717.7	-0.3	0.4	1.7	0.2	5.1	3.6	5.2	35752.2	15371.9	17098.5	9830.9	9314.7
10	13.0	0.1	22.0	15.0	2.0	0.0	2483.6	529.7	348.9	1054.0	-0.5	0.3	2.0	0.2	4.1	2.7	5.8	35698.1	15223.3	17720.3	13014.4	10323.8
11	13.0	0.1	24.0	15.0	2.5	0.1	2499.3	536.1	340.6	1313.2	-0.6	0.3	2.3	0.2	3.4	2.2	6.1	35666.9	15291.4	18247.2	15677.2	11266.0
12	6.0	0.1	18.0	5.0	1.5	0.0	2323.5	227.4	80.4	612.9	-0.6	0.2	2.2	0.1	2.6	0.9	4.7	18507.9	10592.0	11650.8	8633.0	6728.9
13	20.0	0.2	24.0	15.0	2.5	0.1	2666.1	569.3	372.8	1380.9	-0.6	0.3	2.0	0.2	3.7	2.4	6.4	36063.5	16367.8	19157.6	15420.9	11214.4
14	20.0	0.2	24.0	15.0	2.5	0.1	2464.8	590.9	394.5	1311.6	-0.5	0.3	2.2	0.2	3.8	2.5	6.3	35984.7	16325.8	19267.7	15539.2	11911.2
15	6.0	0.1	10.0	5.0	0.8	0.0	1746.9	31.9	-56.4	150.8	-0.8	0.1	1.9	0.2	0.6	-1.1	2.1	18248.4	9815.3	10354.3	5345.0	4992.7
16	6.0	0.1	15.0	5.0	1.4	0.0	2247.5	199.7	74.4	470.2	-0.6	0.3	2.1	0.2	2.4	0.9	3.6	18373.5	10303.3	11450.4	8153.4	6152.4
17	12.0	0.1	15.0	5.0	1.4	0.0	2205.7	208.5	82.1	452.0	-0.5	0.3	2.1	0.1	2.4	0.9	3.2	18610.1	10074.4	11009.9	8741.3	6616.1
18	12.0	0.1	20.0	5.0	1.9	0.0	2175.9	203.0	41.4	628.0	-0.7	0.2	3.0	0.1	1.8	0.4	3.6	18626.5	10579.2	12017.0	11119.9	7359.8
19	12.0	0.1	25.0	5.0	2.6	0.1	2078.1	195.3	-1.9	788.7	-0.8	0.2	4.5	0.1	1.3	0.0	3.5	18794.4	11048.9	12581.0	14604.5	7387.2
20	12.0	0.1	25.0	5.0	2.6	0.1	1766.2	197.2	-0.2	741.5	-0.7	0.1	5.2	0.1	1.3	0.0	3.6	18607.5	10943.6	12423.3	14641.7	7232.0
21	12.0	0.1	20.0	5.0	2.0	0.0	1799.6	215.0	53.5	586.4	-0.6	0.2	3.7	0.1	1.9	0.5	3.6	18616.7	10634.6	11823.4	11381.8	7085.6
22	12.0	0.1	15.0	5.0	1.4	0.0	1887.0	195.1	69.3	404.4	-0.5	0.3	2.3	0.1	2.4	0.9	3.4	18657.7	10227.9	11362.4	8085.8	6653.7
23	12.0	0.1	12.5	5.0	1.1	0.0	1675.6	0.1	-106.9	209.9	-1.0	0.0	2.4	0.1	0.0	-1.5	2.2	18698.3	9952.3	10660.3	6897.3	5961.5
24	12.0	0.1	15.0	5.0	1.1	0.0	2691.3	164.3	38.3	374.7	-0.6	0.3	1.4	0.1	2.4	0.6	3.0	18688.6	10024.8	11023.5	6893.3	6566.7
25	12.0	0.1	12.5	5.0	1.1	0.0	1827.0	113.2	5.0	230.2	-0.5	0.3	1.9	0.1	1.6	0.1	2.3	18718.0	9827.9	10202.9	6937.8	5893.9
26	18.0	0.2	15.0	5.0	1.3	0.0	2218.8	212.5	86.3	427.0	-0.5	0.3	1.8	0.1	2.8	1.1	3.5	18657.2	10521.5	11425.6	7685.2	6409.7
27	18.0	0.2	20.0	5.0	1.9	0.0	2113.4	187.2	25.6	569.5	-0.7	0.2	3.1	0.1	1.7	0.2	3.2	18582.4	10882.2	12162.5	11061.5	7039.5
28	18.0	0.2	25.0	5.0	2.6	0.1	2056.2	172.3	-25.0	771.6	-0.8	0.1	4.5	0.1	1.2	-0.2	3.4	18667.3	11159.7	12702.4	14607.8	7375.5
29	18.0	0.2	25.0	5.0	2.6	0.1	1751.4	186.9	-10.7	727.0	-0.7	0.1	5.1	0.1	1.3	-0.1	3.5	18658.7	11110.0	12524.8	14662.7	7329.1
30	18.0	0.2	20.0	5.0	2.0	0.0	1788.2	205.7	43.7	563.8	-0.6	0.2	3.6	0.1	1.8	0.4	3.5	18560.8	10804.3	11923.3	11392.3	7084.0
31	18.0	0.2	15.0	5.0	1.3	0.0	1862.4	244.5	118.8	356.4	-0.3	0.4	2.3	0.1	3.2	1.5	3.1	18725.6	10658.8	11596.3	7702.7	6398.2
32	18.0	0.2	12.5	5.0	1.1	0.0	1645.3	115.7	8.1	211.7	-0.5	0.3	2.2	0.1	1.7	0.1	2.3	18710.1	10383.8	10944.9	6735.6	5872.0
33	6.0	0.1	15.0	10.0	1.3	0.0	2430.8	266.8	139.3	565.8	-0.5	0.3	1.7	0.1	3.0	1.6	3.9	27424.2	11714.8	14651.5	8964.7	7613.8
34	6.0	0.1	17.5	10.0	1.6	0.0	2578.8	307.8	161.3	745.1	-0.6	0.3	1.7	0.2	3.1	1.6	4.8	27474.6	11978.4	14724.2	9913.7	8992.8
35	6.0	0.1	20.0	10.0	1.9	0.0	2581.2	309.9	145.8	854.6	-0.6	0.3	2.0	0.2	2.7	1.3	4.8	27430.1	12293.6	15197.3	11332.3	8492.3
36	6.0	0.1	25.0	10.0	2.6	0.1	2506.6	294.3	94.5	1106.6	-0.7	0.2	2.9	0.2	1.9	0.6	4.6	27435.9	12773.4	15631.8	15196.9	9228.9
37	6.0	0.1	25.0	10.0	2.6	0.1	2109.5	358.5	158.1	1025.1	-0.7	0.2	3.3	0.2	2.3	1.0	4.8	27434.5	12727.9	15509.1	15273.6	9498.6
38	6.0	0.1	20.0	10.0	1.9	0.0	2143.4	375.1	210.7	787.2	-0.5	0.3	2.4	0.2	3.2	1.8	4.8	27423.3	12286.1	14715.4	11625.4	8054.7
39	6.0	0.1	17.5	10.0	1.7	0.0	2203.4	403.0	256.4	721.5	-0.4	0.4	2.0	0.2	3.9	2.5	4.8	27474.2	11899.4	14252.2	10444.7	7663.9
40	12.0	0.1	15.0	10.0	1.3	0.0	1931.8	136.7	8.3	295.3	-0.5	0.3	1.9	0.1	1.6	0.1	2.4	27113.0	12036.9	13486.1	8570.5	7526.5

Row	Speed_Oil_Pump	oil_massflow	Speed_Feed_Pump	Capstone_Power_setting	wf_Vdot	wf_mdotr	scroll_RPM	W_gross	W_net	W_gross_theory	W_gross_diff	eta_scroll_isen	Scroll_filling_factor	eta_feedpump_isen	eta_cycle_gross (%)	eta_cycle_net	PR	Q_exhaust_ideal	Q_exhaust	Q_oil	Q_evap	Q_water
41	12.0	0.1	20.0	10.0	1.9	0.0	2508.6	289.9	125.8	787.3	-0.6	0.3	2.1	0.2	2.5	1.1	4.2	27065.5	12750.3	14702.8	11486.7	8511.8
42	12.0	0.1	25.0	10.0	2.6	0.1	2433.9	269.7	70.1	1021.0	-0.7	0.2	3.1	0.2	1.8	0.5	4.2	26976.3	13190.0	15348.9	15100.6	8879.9
43	12.0	0.1	25.0	10.0	2.6	0.1	2028.6	324.3	124.3	936.7	-0.7	0.2	3.5	0.2	2.1	0.8	4.4	27002.6	13084.2	15195.8	15156.5	8918.6
44	12.0	0.1	20.0	10.0	1.9	0.0	2068.4	343.7	179.6	699.7	-0.5	0.3	2.5	0.2	3.0	1.6	4.2	26810.1	12702.9	14517.4	11486.2	8357.8
45	12.0	0.1	17.5	10.0	1.6	0.0	2109.9	362.6	216.4	587.3	-0.4	0.4	2.0	0.2	3.7	2.2	4.1	26973.5	12468.5	14347.5	9717.5	7915.6
46	12.0	0.1	25.0	10.0	2.6	0.1	2433.9	266.6	67.2	986.0	-0.7	0.2	3.0	0.2	1.8	0.5	4.1	27330.3	13253.0	15811.2	14797.2	9030.6
47	18.0	0.2	25.0	10.0	2.6	0.1	2093.3	354.7	154.1	961.3	-0.6	0.2	3.2	0.2	2.3	1.0	4.4	27473.4	13223.4	15738.2	15240.0	9399.0
48	18.0	0.2	20.0	10.0	1.9	0.0	2235.4	422.4	257.2	758.6	-0.4	0.4	2.2	0.2	3.6	2.2	4.3	27503.9	13468.8	15717.7	11803.2	9554.4
49	18.0	0.2	17.5	10.0	1.3	0.0	2085.8	355.6	208.1	441.1	-0.2	0.5	1.6	0.1	4.2	2.5	3.5	27573.2	13014.6	14910.5	8404.0	9079.3
50	18.0	0.2	25.0	10.0	2.5	0.1	2558.7	303.7	103.2	1036.6	-0.7	0.2	2.6	0.2	2.1	0.7	4.3	27265.3	13893.4	16243.2	14699.1	10386.5
51	18.0	0.2	20.0	10.0	1.9	0.0	2615.1	319.9	155.1	803.8	-0.6	0.3	1.9	0.2	2.7	1.3	4.1	27234.7	13590.2	15599.3	11652.1	9461.2
52	18.0	0.2	17.5	10.0	1.7	0.0	2472.6	281.3	134.0	675.6	-0.6	0.3	1.8	0.2	2.6	1.2	3.8	27281.2	13096.1	14761.3	10911.0	8700.8
53	18.0	0.2	17.5	10.0	1.6	0.0	2389.3	260.0	112.8	557.0	-0.5	0.3	1.8	0.1	2.5	1.1	3.2	27167.1	12965.4	14612.4	10354.0	8609.9
54	18.0	0.2	27.5	10.0	2.9	0.1	2467.5	280.5	62.4	1138.6	-0.8	0.2	3.2	0.2	1.7	0.4	4.2	26964.9	14194.2	16258.1	16883.6	10021.7
55	18.0	0.2	22.5	10.0	2.3	0.0	2540.5	308.7	126.2	916.3	-0.7	0.2	2.3	0.2	2.3	1.0	4.2	27126.9	13855.6	15786.4	13261.7	9399.5
56	18.0	0.2	27.5	10.0	3.0	0.1	2089.3	356.0	137.1	1113.0	-0.7	0.2	3.7	0.2	2.0	0.8	4.4	27203.8	13802.9	16373.5	17582.5	9971.8
57	18.0	0.2	22.5	10.0	2.3	0.0	2143.4	376.3	193.3	850.5	-0.6	0.3	2.6	0.2	2.8	1.5	4.4	27183.5	13510.7	15789.5	13330.3	9634.0
58	12.0	0.1	27.5	10.0	2.9	0.1	2431.1	268.6	51.1	1137.2	-0.8	0.2	3.5	0.2	1.6	0.3	4.2	27031.5	13230.8	15848.5	16792.7	9600.5
59	12.0	0.1	27.5	10.0	2.9	0.1	2040.0	331.6	113.5	1079.6	-0.7	0.2	4.0	0.2	1.9	0.7	4.4	27055.7	13089.9	15893.4	17189.3	9656.2
60	12.0	0.1	22.5	10.0	2.3	0.0	2524.1	294.7	112.9	920.0	-0.7	0.2	2.5	0.2	2.2	0.9	4.3	27224.5	12837.4	15442.2	13205.0	9267.4
61	12.0	0.1	22.5	10.0	2.3	0.0	2095.2	357.6	175.5	841.9	-0.6	0.3	2.9	0.2	2.7	1.3	4.4	27224.2	12712.2	15392.9	13255.9	8883.3
62	12.0	0.1	17.5	10.0	1.7	0.0	2470.0	280.0	133.2	729.9	-0.6	0.3	1.8	0.2	2.6	1.2	4.3	27245.8	12186.0	14531.1	10692.6	8083.2
63	12.0	0.1	16.0	10.0	1.6	0.0	2114.1	186.1	50.9	451.7	-0.6	0.3	2.2	0.1	1.8	0.5	2.7	27275.3	11806.1	14017.0	10522.2	7563.8
64	6.0	0.1	27.5	15.0	2.9	0.1	2651.8	331.0	111.9	1353.7	-0.8	0.2	2.9	0.2	1.9	0.6	4.8	36527.5	14984.3	19128.1	17486.4	11096.9
65	6.0	0.1	27.5	15.0	2.9	0.1	2231.1	422.1	202.4	1244.1	-0.7	0.2	3.2	0.2	2.4	1.2	5.1	36688.4	14888.9	19149.2	17290.9	11130.4
66	6.0	0.1	25.0	15.0	2.5	0.1	2687.4	341.1	140.1	1176.7	-0.7	0.2	2.4	0.2	2.3	0.9	4.9	36762.9	14797.7	18470.2	14950.2	10646.4
67	6.0	0.1	25.0	15.0	2.5	0.1	2252.0	432.7	231.2	1076.4	-0.6	0.3	2.8	0.2	2.9	1.5	5.1	36740.0	14631.8	18483.6	15020.0	10900.5
68	6.0	0.1	22.5	15.0	2.3	0.0	2766.3	364.6	181.2	1119.2	-0.7	0.2	2.0	0.2	2.7	1.3	5.1	36868.7	14479.5	18065.6	13693.4	10497.9
69	6.0	0.1	22.5	15.0	2.3	0.0	2328.2	466.4	282.4	1027.2	-0.5	0.3	2.3	0.2	3.4	2.1	5.3	36762.2	14335.9	18023.9	13758.3	10257.5
70	6.0	0.1	20.0	15.0	2.0	0.0	2789.2	371.6	205.7	1065.5	-0.7	0.3	1.8	0.2	2.9	1.6	5.2	36834.9	14109.9	17520.3	12832.5	9781.0
71	6.0	0.1	20.0	15.0	1.9	0.0	2387.0	0.0	-166.5	959.6	-1.0	0.0	1.9	0.2	0.0	-1.3	5.5	36823.4	13959.4	17461.3	12491.2	9680.0
72	6.0	0.1	20.0	15.0	1.9	0.0	2713.4	348.5	183.4	954.3	-0.6	0.3	1.8	0.2	2.9	1.5	5.1	35787.4	14217.4	17583.2	11871.0	9125.3
73	6.0	0.1	20.0	15.0	1.9	0.0	2356.2	481.3	315.1	913.1	-0.5	0.3	2.0	0.2	4.0	2.6	5.4	36210.4	14059.4	17220.2	12031.6	10449.6
74	12.0	0.1	27.5	15.0	2.9	0.1	2172.6	396.7	177.2	1161.6	-0.7	0.2	3.3	0.2	2.3	1.0	4.7	36141.7	15148.0	18675.4	17214.1	11018.1
75	12.0	0.1	27.5	15.0	2.9	0.1	2603.3	317.0	98.2	1249.8	-0.7	0.2	2.9	0.2	1.9	0.6	4.5	36192.3	15325.4	18614.2	17117.4	11045.1
76	12.0	0.1	25.0	15.0	2.6	0.1	2622.6	324.1	123.2	1118.9	-0.7	0.2	2.5	0.2	2.1	0.8	4.5	36282.2	15048.5	18469.7	15184.7	10489.7
77	12.0	0.1	25.0	15.0	2.6	0.1	2165.9	392.3	191.0	1015.0	-0.6	0.2	3.0	0.2	2.6	1.3	4.7	36205.5	14944.1	18358.7	15229.0	10642.2
78	12.0	0.1	22.5	15.0	2.3	0.0	2708.3	348.2	164.8	1045.6	-0.7	0.2	2.1	0.2	2.6	1.2	4.7	36275.8	14795.2	17992.2	13611.5	10341.7
79	12.0	0.1	22.5	15.0	2.3	0.0	2273.7	441.5	257.7	960.4	-0.5	0.3	2.4	0.2	3.2	1.9	4.9	36313.7	14647.0	17996.2	13676.7	10452.9
80	12.0	0.1	20.0	15.0	2.0	0.0	2681.1	339.3	173.6	956.6	-0.6	0.3	1.9	0.2	2.6	1.3	4.5	36320.4	14454.5	17602.3	13041.8	10261.3

Row	Speed_Oil_Pump	oil_massflow	Speed_Feed_Pump	Capstone_Power_setting	wf_Vdot	wf_mdotr	scroll_RPM	W_gross	W_net	W_gross_theory	W_gross_diff	eta_scroll_isen	Scroll_filling_factor	eta_feedpump_isen	eta_cycle_gross (%)	eta_cycle_net	PR	Q_exhaust_ideal	Q_exhaust	Q_oil	Q_evap	Q_water
81	12.0	0.1	20.0	15.0	2.0	0.0	2263.8	435.6	269.8	862.7	-0.5	0.3	2.3	0.2	3.3	2.1	4.5	36090.5	14240.5	17562.7	13097.3	9787.4
82	12.0	0.1	17.5	15.0	1.6	0.0	1899.1	126.2	-22.4	316.2	-0.6	0.2	2.1	0.1	1.1	-0.2	2.1	36037.9	13401.9	16204.6	11075.4	10121.5
83	18.0	0.2	27.5	15.0	2.9	0.1	2572.9	282.9	64.2	1202.5	-0.8	0.2	3.0	0.2	1.7	0.4	4.3	35760.5	15566.1	18893.2	17091.3	11752.1
84	18.0	0.2	27.5	15.0	2.9	0.1	2072.0	347.3	128.1	1093.1	-0.7	0.2	3.5	0.2	2.0	0.7	4.5	35711.1	15515.0	18759.6	17161.3	11564.5
85	18.0	0.2	25.0	15.0	2.6	0.1	2594.2	314.0	113.1	1081.1	-0.7	0.2	2.6	0.2	2.1	0.7	4.4	35952.7	15564.9	18621.3	15165.4	11355.1
86	18.0	0.2	25.0	15.0	2.6	0.1	2139.5	380.0	178.7	984.3	-0.6	0.2	3.0	0.2	2.5	1.2	4.5	36014.0	15510.8	18683.4	15230.0	11327.8
87	18.0	0.2	22.5	15.0	2.3	0.0	2728.0	353.2	169.8	1020.8	-0.7	0.2	2.1	0.2	2.5	1.2	4.3	36125.5	15449.1	18495.2	13997.7	10776.9
88	18.0	0.2	22.5	15.0	2.3	0.0	2350.3	478.8	294.4	971.7	-0.5	0.3	2.3	0.2	3.4	2.1	4.7	36001.6	15367.0	18319.5	13981.2	11231.4
89	18.0	0.2	20.0	15.0	1.9	0.0	2392.1	260.4	93.7	692.5	-0.6	0.2	2.0	0.2	2.1	0.7	3.3	35894.4	14727.3	17323.1	12681.4	10116.7
90	6.0	0.1	27.5	20.0	2.9	0.1	2808.6	376.1	156.0	1476.5	-0.7	0.2	2.5	0.2	2.1	0.9	5.3	45693.4	16681.9	21090.5	17511.8	11743.8
91	6.0	0.1	27.5	20.0	2.9	0.1	2358.6	480.4	259.8	1356.1	-0.6	0.2	2.8	0.2	2.7	1.5	5.5	45569.2	16560.0	20807.9	17607.3	11914.2
92	6.0	0.1	25.0	20.0	2.5	0.1	2910.8	377.0	174.5	1357.8	-0.7	0.2	2.0	0.2	2.4	1.1	5.5	45894.0	16450.0	20412.2	15420.3	11608.6
93	6.0	0.1	25.0	20.0	2.5	0.1	2449.3	524.0	320.8	1250.5	-0.6	0.3	2.3	0.2	3.4	2.1	5.8	45704.8	16242.6	20325.4	15491.0	11291.5
94	6.0	0.1	22.5	20.0	2.2	0.0	2874.9	395.4	210.5	1260.5	-0.7	0.2	1.8	0.2	2.8	1.5	5.7	45845.6	16077.5	19804.0	14236.4	10958.4
95	6.0	0.1	22.5	20.0	2.2	0.0	2488.8	544.2	358.5	1177.6	-0.5	0.3	2.0	0.2	3.8	2.5	6.0	45951.5	15954.4	19808.2	14262.1	10783.6
96	12.0	0.1	27.5	20.0	2.9	0.1	2386.6	494.9	273.5	1322.2	-0.6	0.2	2.6	0.2	2.8	1.6	5.3	45780.3	17060.6	20854.4	17392.4	12395.5
97	12.0	0.1	27.5	20.0	2.9	0.1	2816.1	378.8	158.2	1425.0	-0.7	0.2	2.3	0.2	2.2	0.9	5.1	45527.8	17150.0	20961.3	17286.8	13353.3
98	12.0	0.1	25.0	20.0	2.6	0.1	2911.6	408.7	205.4	1359.0	-0.7	0.2	2.0	0.2	2.6	1.3	5.3	45928.3	16949.9	20627.0	15826.0	11603.3
99	12.0	0.1	25.0	20.0	2.5	0.1	2486.4	543.3	339.4	1237.3	-0.6	0.3	2.1	0.2	3.5	2.2	5.6	45772.5	16679.6	20506.9	15556.7	11847.6
100	12.0	0.1	22.5	20.0	2.2	0.0	2728.0	352.1	166.6	1157.8	-0.7	0.2	1.9	0.2	2.4	1.1	5.0	45739.7	16481.8	20105.9	14740.6	11569.4
101	12.0	0.1	22.5	20.0	2.2	0.0	2357.8	480.5	294.7	1073.3	-0.6	0.3	2.1	0.2	3.3	2.0	5.2	45717.7	16490.7	20061.4	14643.2	11535.1
102	12.0	0.1	20.0	20.0	1.9	0.0	2504.2	290.2	123.2	820.8	-0.6	0.2	1.9	0.2	2.2	0.9	3.8	45923.9	16204.8	19391.5	13291.8	10788.1
103	18.0	0.2	27.5	20.0	2.9	0.1	2931.7	413.7	192.3	1493.7	-0.7	0.2	2.2	0.2	2.3	1.1	5.0	45505.5	18377.7	22106.2	17866.8	13678.0
104	18.0	0.2	27.5	20.0	2.9	0.1	2497.9	548.2	326.3	1374.9	-0.6	0.3	2.5	0.2	3.1	1.8	5.2	45363.0	18243.4	21989.4	17914.2	13319.1
105	18.0	0.2	25.0	20.0	2.5	0.1	2842.9	384.9	181.3	1280.3	-0.7	0.2	2.0	0.2	2.4	1.1	4.8	45289.7	18037.5	21454.1	16309.7	12889.8
106	18.0	0.2	25.0	20.0	2.5	0.1	2413.8	506.5	302.2	1185.2	-0.6	0.3	2.3	0.2	3.1	1.9	5.0	45255.4	17964.6	21311.3	16329.0	12939.7
107	6.0	0.1	27.5	25.0	2.9	0.1	2499.1	551.0	329.0	1497.8	-0.6	0.3	2.5	0.2	3.1	1.8	6.0	55437.9	18354.0	22668.0	18064.3	13170.2
108	6.0	0.1	27.5	25.0	2.9	0.1	2930.5	414.6	193.0	1635.1	-0.7	0.2	2.2	0.2	2.3	1.1	5.8	55922.8	18506.6	22873.8	18044.8	12754.9
109	6.0	0.1	25.0	25.0	2.5	0.1	2950.3	422.6	218.4	1505.8	-0.7	0.2	1.9	0.2	2.6	1.3	6.0	56001.9	18142.3	22437.5	16311.3	12247.4
110	6.0	0.1	25.0	25.0	2.5	0.1	2585.1	596.3	391.4	1417.9	-0.6	0.3	2.0	0.2	3.7	2.4	6.3	55938.4	18009.8	22293.6	16316.0	12141.6
111	6.0	0.1	22.5	25.0	2.2	0.0	2765.5	363.2	177.7	1312.8	-0.7	0.2	2.0	0.2	2.3	1.1	5.5	55875.2	17688.0	21815.1	15669.4	11912.5
112	6.0	0.1	22.5	25.0	2.2	0.0	2327.4	466.0	280.1	1190.7	-0.6	0.3	2.3	0.2	3.0	1.8	5.7	55525.3	17564.5	21690.2	15606.7	11962.5
113	12.0	0.1	27.5	25.0	2.9	0.1	2745.3	358.4	137.5	1469.4	-0.8	0.2	2.6	0.2	1.9	0.7	4.9	55858.0	19361.6	23958.7	18703.6	13688.2
114	12.0	0.1	27.5	25.0	2.9	0.1	2596.7	597.8	374.5	1550.9	-0.6	0.3	2.2	0.2	3.2	2.0	5.9	55751.8	18809.7	23289.7	18493.9	13941.3
115	12.0	0.1	25.0	25.0	2.5	0.1	2755.2	362.0	157.0	1401.5	-0.7	0.2	2.0	0.2	2.1	0.9	5.4	56029.6	18581.9	22756.0	17076.0	13592.0
116	12.0	0.1	25.0	25.0	2.5	0.1	2360.7	482.4	276.9	1297.9	-0.6	0.2	2.3	0.2	2.8	1.6	5.6	56165.0	18462.8	22695.4	17076.9	13523.5
117	12.0	0.1	22.5	25.0	2.2	0.0	2549.8	311.3	125.3	949.6	-0.7	0.2	2.1	0.2	1.9	0.8	3.6	56339.2	18019.1	21824.3	15983.8	12421.1
118	12.0	0.1	22.5	25.0	2.2	0.0	2546.2	301.0	115.0	933.5	-0.7	0.2	2.1	0.2	1.9	0.7	3.5	56285.6	17972.2	21838.0	15996.8	12553.0